

Black Phosphorus, Phosphorene and Phosphorene Nanoribbons

Literature Review

Mitchell Watts



Department of Physics

UCL

August 2016

Black Phosphorus, Phosphorene and Phosphorene Nanoribbons

Literature review

Mitchell Watts

A detailed overview of the literature on Black Phosphorus, Phosphorene and Phosphorene Nanoribbons is presented, along with some relevant theory

Contents

1	Introduction	19
1.1	Layered and 2D materials	19
1.2	Black Phosphorus	20
2	Properties	21
2.1	Introduction	21
2.2	Structure	21
2.2.1	Bulk Black Phosphorus	21
2.2.2	Phosphorene	24
2.3	Physical and air stability	24
2.3.1	Physical	24
2.3.1.1	Black Phosphorus	24
2.3.1.2	Phosphorene	24
2.3.2	Oxidation and stability	24
2.3.2.1	Introduction	24
2.3.2.2	Dominant oxidation reaction	26
2.3.2.3	Secondary oxidation mechanism	31
2.3.2.4	Passivation	32
2.3.3	Thermal	37
2.3.4	Strain and Stress	40
2.4	Electronic and optical	41
2.4.1	Band structure	41
2.4.1.1	Black Phosphorus	41
2.4.2	Transport	44
2.4.2.1	Black Phosphorus	44
2.4.3	Optical	46
2.4.3.1	Black Phosphorus	46
2.4.4	Superconductivity	46
2.5	Phononic	48
2.5.1	Black Phosphorus	48
2.5.2	Phosphorene	56
3	Synthesis	59
3.1	Black Phosphorus	59
3.2	Phosphorene	61
3.2.1	Mechanical	61
3.2.2	Liquid-Phase	61
3.2.3	Growth	65

3.2.4	Etching	65
4	Characterisation	68
4.1	Introduction	68
4.2	Physical	68
4.2.1	Introduction	68
4.2.2	AFM	68
4.2.3	Optical Microscopy	68
4.2.4	Young's Modulus	69
4.2.5	Diffraction	69
4.3	Electronic and Optical	73
4.3.1	PL	73
4.3.1.1	Extinction coefficients	76
4.4	Phononic	76
4.4.1	Black Phosphorus	76
5	Applications	78
6	Phosphorene Nanoribbons	85
6.1	Isolation	85
6.2	Properties	88
6.2.1	Physical and stability	88
6.2.2	Electronic and optical	88
6.2.3	Phononic and thermal	97
6.3	Characterisation and DFT	100

List of Figures

2.1	The structure of black phosphorus - note the ABA stacking order of layers. (a) 3D representation. (b) Lateral view. (c) Top view. These structures have been obtained by relaxing structures using DFT calculations. [5]	22
2.2	Schematics of (a) the structure of phosphorene, (b) the bonding structure and sp ₃ hybridization process, and (c) the mechanism of van der Waals force formation between adjacent layers. The small yellow and green balls represent the lone pairs and bonding electrons, respectively. The separation distance between neighboring layers is approximately 5.0 - 5.5 Å [13]	23
2.3	The layered structure of (a) black and (b) blue phosphorus in top and side views. Atoms at the top and bottom of the nonplanar layers are distinguished by color and shading, and the Wigner-Seitz cells are shown by the shaded region. (c) Schematic of the conversion of black to blue phosphorus by dislocations, highlighted by the shaded regions and arrows. (d) Equilibrium structure of AB stacked blue phosphorus in side view. [112]	23
2.4	Applications of FL-BP. (a,b) Sensing of NH ₃ gas using BP films. (a) Sensor response plot shows percentile resistance change versus time with a bias voltage of 1V at room temperature (b) Plot of signal-to-noise ratio as a function of NH ₃ concentration from 1 to 3 p.p.m. (c–e) Saturable absorption of std-BP and graphene in CHP for femtosecond pulses excited at (c) 1,030nm and (d) 515 nm. Linear transmission T ₀ is given in the legend. (e) Saturation intensity of FL-BP and graphene as a function of T ₀ . (f) Representative stress–strain curves for PVC and PVC: FL-BP (0.3 vol%). Inset: low strain regime. (g–i) Young’s modulus, including the theoretical constant-strain rule-of-mixtures modulus prediction (g), tensile strength (h) and tensile toughness (i) plotted as a function of FL-BP volume fraction. (j) Calculated orientation dependence of the in-plane two-dimensional Young’s modulus (YBP, blue) and Poisson’s ratio (n, red), of black phosphorus, together with the Voigt–Reuss–Hill averaged in-plane modulus (oYBP4, black). [24]	25

- 2.5 (a)-(d) Selected AFM scans of a BP flake in air taken at (a) 3 hours, (b) 46 hours, (c) 69 hours, and (d) 122 hours after exfoliation. Dotted white lines indicate the position of the line profiles shown in (e). (e) Line profiles taken across the BP flake from the scans in (a)-(d) as well as a line profile for the AFM scan taken directly after exfoliation. (f) Total volume of the flake and water over the measurement period. [30] 26
- 2.6 Evolution of the photooxidation reaction in ambient conditions of multilayer 2D-phosphane probed by TEM-EELS analysis. a,b, TEM images at 80kV of a flake recorded right after exfoliation in air (a) and after a further 20s in normal light (b). c,d, Energy-filtered TEM images extracted from the data cube at the oxygen K-edge (534 eV) in the same conditions as in a and b, respectively. Colour scale bars: normalized intensity relative to the maximum. [17] 27
- 2.7 Chemical analysis by hyperspectral TEM-EELS spectroscopy of a multilayer 2D-phosphane exfoliated under ambient light in air. a, High-angle annular dark-field (HAADF) contrast image taken at 80kV. b-d, EELS images extracted from the data cube at the energy of phosphorus L_{2,3}-edge (130.2 and 136 eV) and oxygen K-edge (534 eV), as indicated. e, EELS spectra corresponding to the selected areas in a. Colour scale bars: normalized intensity relative to the maximum. [17] 28
- 2.8 Sketch of the density of states (DOS) of aqueous oxygen acceptor and of n-layer 2D-phosphane, as predicted by Marcus-Gerisher theory. On the left: DOS of mono-, bi- tri-layer 2D-phosphane and bulk P(black). On the right: the energy diagram of the DOS of aqueous oxygen acceptor states with the enlargement of the DOS due to the solvent reorganization. The figure also illustrates by the blue arrows the proposed CT reaction induced by photo-excitation of n-layer 2D phosphane. [18] 29
- 2.9 Morphology change of an exfoliated black phosphorus flake on *SiO*₂/Si after exposure to water and air. a. Optical images of a freshly exfoliated black phosphorus flake. b. Same flake after being submerged in DI water for 1 week. c. Same flake after a total of 2 weeks exposure to water. d. Image after removal of the flake from DI water and exposure to air for 1 week, e. Same sample after annealing at 120 °C for 2 hours in ultrahigh vacuum (10⁻⁹ Torr). f. After additional annealing at 250 °C for 2 hours in ultrahigh vacuum. [28] 30
- 2.10 (a) AFM topography image (500 nm x 500 nm) of oxidized black phosphorus with an RMS roughness of 1.5 nm. (b) Thickness of two exfoliated black phosphorus flakes on *SiO*₂/Si as a function of exposure time, where red circles represent a 406 nm as-cleaved flake and blue squares represent a 95 nm as-cleaved flake. [15] 31

2.11 Stability of exfoliated black phosphorous nanosheets. (a,b) Relative absorbance at 465nm, measured as a function of time, for (a) the standard dispersion exfoliated in solvents labelled. (b) std-BP in CHP compared with size-selected dispersions containing small (S-BP) and large nanosheets (L-BP). The dashed lines represent exponential decays: $A = A_{UnRe} + A_{Re}e^{-\frac{t}{\tau}}$, where A_{Re} represents the component of BP, which reacts with water/O ₂ , A_{UnRe} represents the unreacted component and τ represents the reaction timescale. (c) Reaction timescale, τ , plotted versus the fraction of BP which reacts, $\frac{A_{Re}}{A_{UnRe} + A_{Re}} A_{Re}$, for a number of different systems. (d) Fitted time-dependent absorbance (465nm) data for std-BP in CHP and std-BP dispersions with 3 vol% and 12.5 vol% of water added. (e) Plot of τ versus volume fraction of added water. The inset shows the fraction of unstable BP plotted versus water content. (f) Plot of τ versus $\frac{A_{Re}}{A_{UnRe} + A_{Re}}$ for BP exfoliated in CHP with and without the addition of water. (g) Sequence of AFM images of the same sample region of an as-prepared sample, and after 1, 4 and 11 days of exposure to ambient conditions, respectively (scale bar, 600nm). (h) Map showing both fractional length, L, and width, w, changes as measured by AFM immediately after exfoliation after day 4. Negative values of $\frac{\Delta w}{w_0}$ and $\frac{\Delta L}{L_0}$ indicate that the nanosheets are getting smaller over time. (i) Mean Raman spectra (633nm excitation) summed over the same sample region of an as-prepared sample, after 4 days and 11 days, respectively. Inset: Raman A_g^1 intensity map of the sample region (freshly prepared and after 11 days). (j) TEM images of the same flake deposited from a freshly prepared dispersion and after 16 days. [24]	33
2.12 Reactivity of solvent-stabilized Black Phosphorous with water. (a) Edge selective degradation model for BP exposed to pure neutral water. Top and bottom panel represent reagent (BP edge + three water molecules) and reaction products (BP defective edge+phosphine+phosphorous acid), respectively, with the reaction energy also given. Green, red and white balls represent P, O and H atoms, respectively. (b) Experimental data for amount of reacted phosphorus and water, respectively, as a function of time for std-BP GB in CHP after addition of 3 vol% of water. The data was obtained from tracking both water and BP concentrations by ultraviolet– visible spectroscopy. (c) Molar ratio of water/ BP as a function of time measured for a std-BP GB dispersion in CHP after addition of 3 and 10 vol% of water. The molar ratio is centred at 2–3. [24]	34
2.13 Influence of water amount in the liquid exfoliation process of BP in DMSO at different times (4, 9, 14, 20 h). [79]	35

- 2.14 AFM study of the surface integrity of passivated and exposed BP sheets in ambient conditions. (a-b) Atomic force microscopy (AFM) scans of a 5-nm-thick bP crystal partly covered with graphene. The images are acquired, respectively, 10min and 24h after exposure to ambient conditions. The white dashed lines outline the passivating graphene crystal. (c) AFM scan of a 10-nm-thick bP crystal partly covered with hexagonal BN (hBN) after 5 days in ambient conditions. Scale bar, 4mm (for all images). (d) Average roughness (Ra) versus time in ambient conditions for the passivated (blue triangles) and exposed (red squares) bP surface of the bP/graphene sample from a,b. (e) Height distribution of the exposed (top) and encapsulated bP surface (bottom) at different times after exposure to ambient conditions for the bP/graphene sample from a,b.(f) Average roughness (Ra) versus time for the passivated (blue triangles) and exposed (red squares) bP surface of the bP/hBN sample from c. . [14] 35
- 2.15 Comparison of encapsulated and exposed ultrathin BP FETs. (a) A schematic three- dimensional illustration of the device geometry. (b) Optical image of a typical device with outlines of the ultrathin bP crystal (black dashed-dotted line) and the passivating hexagonal BN crystal (blue dashed line). Scale bar, $3\mu m$. (c) Four-terminal conductance versus backgate voltage (V_g) of the passivated and exposed channels of two bP FETs at source-drain bias $V_{sd} = 50mV$ and temperatrure $T = 300K$. Field-effect mobilities were extracted from the line fit (black dashed line). [14] 36
- 2.16 I-V characteristic of the passivated and exposed channels of a black phosphorus field-effect transistor. (a) Two-terminal sheet conductance versus backgate voltage (V_g) for the passivated (solid blue curve) and exposed (solid red curve) channel at temperature $T = 200K$. (b) I-V characteristic of the device on the hole side for the passivated (solid blue curve) and exposed (solid red curve) channel(c) Source-drain current (I_{sd}) versus source-drain voltage (V_{sd}) for the passivated channel The inset shows the output conductance qI_{sd}/qV_{sd} (d) I_{sd} versus V_{sd} for the exposed region on the electron conduction side [14] 36
- 2.17 Evolution of black phosphorus with thin dielectric capping. (a) Schematics ofBP samples on Al_2O_3/Si substrates without (left) and with (right) a thin Al_2O_3 capping layer. Red arrows indicate the possible pathways of oxygen and moisture to react with the sample. The MIM setup is also sketched on top of the thin-cap sample. (b) Local sheet resistance maps derived from the MIM-Real data of a 24 nm-thick flake capped by 3nm Al_2O_3 layer. (c) AFM topography of the same flake simultaneously acquired during the same time duration. (d) Raman intensity maps integrated over $445-475\text{ }cm^2$ 1 (A_g^2 mode of phosphorene) and $800-900\text{ }cm^2$ 1 (consistent with P-Ostretching modes) measured at Day 9. All scale bars are 5 mm. [34] 38

2.18 Aging of black phosphorus FETs. (a-c) Id-Vg plot of BP devices with various capping schemes. (a) FETs with thin capping (5 nm ALD-deposited Al_2O_3) experienced significant degradation, such as reduced ON/OFF ratio and the increase of gate hysteresis. (b) Thick-cap devices (25 nm ALD Al_2O_3) showed less aging effect. (c) Devices with double-layer capping (25 nm ALD Al_2O_3 followed by DuPont Teflon-AF fluoropolymer) showed the least aging. (d-e) Statistical analysis of BP FET devices with different capping methods. (d) The change of ON current (I_{on}) with respect to the values at Day 1. (e) Hysteresis in Vg between forward and reverse sweeps. The best stability is obtained in devices with double-layer capping. (f) I_{on}/I_{off} ratio of three selected devices. Thin capped device showed sharp degradation. In contrast, I_{on}/I_{off} ratio of thick capped device was preserved to 70% compared to Day 1. Double capped device showed the best preservation of I_{on}/I_{off} ratio, with negligible change after 79 days. [34]	39
2.19 The direction dependence of Young's modulus of a monolayer phosphorene. [93]	40
2.20 (a) Layered structure, (b) two-dimensional Brillouin zone, and (c) the highest valence and lowest conduction bands of monolayer phosphorene. Green and red curves are the projections of global band edges of the monolayer onto the xz and yz planes. The energy level of vacuum is set to zero. [91]	41
2.21 Calculated band structure. Calculated electronic band structure for monolayer, bilayer, trilayer and bulk black phosphorus sheets at all high-symmetry points in the Brillouin zone. The energy is scaled with respect to the Fermi energy E_F . [5]	42
2.22 LCAO band dispersion of (a) monolayer, (b) bilayer, and (c) five-layer phosphorene. Only the nearest-neighbor and next-nearest- neighbor in-plane couplings and the nearest-neighbor interlayer coupling are taken into account. (d) Symmetric points in the 2D Brillouin zone. [20]	42
2.23 Global band structure of (a) monolayer phosphorene, (b) monolayer phosphorene under the vertical electric field, and (c) bilayer phosphorene. Several Dirac points are indicated by dashed circles. [20]	43
2.24 Comparison of the band gap values for different 2D semiconductor materials and some bulk semiconductors. The horizontal bars spanning a range of band gap values indicate that the band gap can be tuned over that range by changing the number of layers, straining, or alloying. In conventional semiconductors, the bar indicates that the band gap can be continuously tuned by alloying the semiconductors (e.g., $Si_{1-x}Ge_x$ or $In_{1-x}Ga_xAs$). [4]	45
2.25 Optical absorption spectra. (a,b) Optical absorption spectra of few-layer BP for light incident in the c (z) direction and polarized along the a (x) and b (y) directions, respectively. (c) Schematic illustration of a proposed experimental geometry to determine the orientation of few-layer BP structures using optical absorption spectroscopy, and thus to utilize the anisotropic electronic properties of BP. [70]	47

2.26	[102]	48
2.27	Top view of a single layer of black phosphorus, with the definition of the unit cell (green rectangle) and of the parameters to locate the basis atoms. Open (closed) circles represent the atoms at the bottom (top) part of the puckered structure. [73]	49
2.28	Normal modes of the Γ -point optical phonons in black phosphorous. [81]	49
2.29	Phonon dispersion for SLBP along Γ M from the fitted SW potential is compared to the data from ab initio calculations. [33]	50
2.30	Calculated full phonon dispersion (a) Phonon dispersion along high symmetry q points. (b) The high symmetry q path in the Brillouin zone. The Γ -A and Γ -X directions are corresponding to the ZZ and AC directions, respectively. [86]	50
2.31	Experimental scheme and birefringence phenomenon in BP crystals. a) Schematic diagram of angle-resolved polarized Raman scattering of the BP sample. b) Schematic illustration of the birefringence effect in the BP crystal. The x and z axes are along the zigzag (ZZ) and armchair (AC) directions, respectively. θ is the angle between the AC direction and the polarization direction of the incident laser. The phase delay between the two components of the incident due to birefringence is represented by δ [56]	51
2.32	Angular dependence of the Raman intensities measured with the (a,d) 633 nm, (e,f) 532 nm, and (g,h) 488nm laser lines. The polarization configurations (parallel or cross) and the different Raman modes are indicated in each panel. Dots are experimental data, and solid curves correspond to the best fits to the data using eqs 10 and 11 for each configuration and Raman mode. [74]	54
2.33	Raman spectra of BP flakes with different thicknesses [8]	56
2.34	Raman spectra of single-layer and bilayer phosphorene and bulk black phosphorus films [60]	57
2.35	Thickness dependence of $I_{A_g^1}/I_{Si}$ [9]	57
2.36	The Raman shift of the A_g^1 , B_{2g} and A_g^2 modes measured for black phosphorus flakes with different thicknesses. [6]	58
3.1	(a) Low-magnification SEM image of an individual B-P ribbon, (b) the high-magnification SEM image of the B-P ribbon, (c) the high-magnification SEM image of a thin ribbon, and (d) EDAX pattern of the grown B-P. [109]	60
3.2	Ex-situ XRD patterns of black phosphorus taken before charging and after charging down to different voltages. a, In wide range. b, Amplification of (002) diffraction peaks. c, Amplification of (004) diffraction peaks. [83]	60
3.3	Three step exfoliation procedure of P(black). Step 1: Exfoliation done on the flat PDMS-1. Step 2: The flakes were reported on semi-spherical PDMS-2 stamp. Step 3: the stamp was rolled on the substrate (SiO ₂ on Si) with an estimated speed of 0.1 cm/s. [18]	62

3.4 Characterization of individual nanosheets. (a-c) Representative atomic force microscopic (AFM) images (scale bars in a, b and c: are 500, 200 and 1000 nm). (d) Height profile of the nanosheet in the inset a (scale bar, 500nm). (e) Heights of 470 steps of deposited FL-BP nanosheets in ascending order. The step height is always found to be a multiple of 2 nm, which is the apparent height of one monolayer. 2.06 ± 0.18 nm. (f) Plot of number of layers per nanosheet as a function of flake area determined from AFM. The dashed line indicates N / pA behaviour. (g) Histogram of number of monolayers per nanosheet (sample size=126). The mean number of layers is determined as 9.4 ± 1.3 nm (h,i) Large area AFM image (h, scale bar, 1mm) and Raman A_g^1 intensity map (i, excitation wavelength 633nm) of the same sample region. (j) Raman spectra (normalized to A_g^2) of the nanosheets indicated in h and i. (k) Histogram of the intensity ratio of the $\frac{A_g^1}{A_g^2}$ modes obtained from the analysis of 120 baseline-corrected spectra acquired over an area of $2525 mm^2$ (sample size=120) The absence of spectra with an intensity ratio 0.6 strongly suggests that no basal plane oxidation has occurred. [24]	63
3.5 Basic characterization of exfoliated black phosphorous. (a) Structure of black phosphorus (BP). (b) SEM image of a layered BP crystal (scale bar, 100 nm). (c) Photograph of a dispersion of exfoliated FL-BP in CHP. (d-f) Representative low-resolution transmission electron microscopy (TEM) images of FL-BP exfoliated in N-cyclohexyl-2-pyrrolidone (CHP) (scale bars in d-f: 500, 100 and 500nm). (g) Bright-field scanning transmission TEM (STEM) image and (h) Butterworth-filtered high-angle annular dark field (HAADF) STEM image of FL-BP (exfoliated in isopropanol) showing the intact lattice (scale bars in g and h, 2 and 1 nm). (i) Nanosheet length histogram of the exfoliated FL-BP obtained from TEM (sample size=239). (j) Extinction, absorbance, scattering coefficient spectra of FL-BP in CHP. (k) Concentration of FL-BP as a function of sonication time. The dashed line shows power law behaviour with exponent 0.4. (l) Raman spectrum (mean of 100 spectra, excitation 633nm) of a filtered dispersion. Inset: scanning electron microscopic image of thin film (scale bar, 2mm). (m) X-ray photoelectron spectroscopy P core-level region. [24])	64
3.6 TEM image of phosphorene nanobelt. [82]	64
3.7 Selective variation of the centrifugationrate allows for control over flake thickness (a) and flake lateral size (b). [95]	65
3.8 (a) Strategy for the synthesis of thin BP films. (b) Schematic apparatus for the deposition of RP film. (c) Photos of thin RP film on PET substrate (left), RP/PET disc for pressurization (middle) and BP/PET disc after pressurization. (d) Schematic of the high pressure anvil cell for conversion. The arrows indicate the directions along which the pressure is applied in conversion process. [41]	66

- 3.9 Schematically showing the fabrication of air-stable mono- and few-layer phosphorene samples. (a) A thick phosphorene flake is firstly exfoliated onto a SiO_2/Si substrate and the sample is then treated with O_2 plasma etching (yellow balls). (b) During the O_2 plasma pre-treatment process, the top layers of the phosphorene flake are oxidized to become P_xO_y , which then serves as a protective layer for the remaining phosphorene sample underneath. With further O_2 plasma etching, oxygen plasma can penetrate the P_xO_y layer by diffusion and oxidize the underlying phosphorene, and this thins down the phosphorene layer and also increases the thickness of the P_xO_y . Meanwhile, the O_2 plasma physically sputters away the P_xO_y layer from the top because of the collisions by oxygen plasma. After the plasma pre-treatment, a dynamic equilibrium is reached between oxidation of the phosphorene and physical removal of the P_xO_y layer, such that the P_xO_y layer approaches a constant thickness and the etching rate also becomes constant. (c) Because of the constant etching rate, any designated number of layers of phosphorene down to a monolayer can then be precisely fabricated and the degradation of the remaining layers is inhibited because of the protective nature of the P_xO_y . (d) To further improve the lifetime of the phosphorene produced, the sample was also coated with an Al_2O_3 protective layer by ALD. In this case the P_xO_y layer prevents the underlying phosphorene from reacting with the precursor gases used in the ALD process, which is especially important for samples less than a few layers thick [66] 67
- 4.1 Isolation of few-layer black phosphorus flakes. (a) Transmission mode optical microscopy image of a few-layer black phosphorus flake exfoliated onto a PDMS substrate. An optical transmittance line profile has been included in the figure to highlight the reduction of about 5.5% in the optical transmittance in the thinner part of the flake. (b) Bright field optical microscopy image of the same flake after transferring it onto a SiO_2/Si substrate. Note that part of the flake was broken during the transfer. (c) Atomic force microscopy topography image of the region highlighted with a dashed square in (b). A topographic line profile, acquired along the horizontal dashed black line, has been included in the image. [5] 69
- 4.2 Aging of black phosphorus flakes. (a) Sequence of optical images acquired at different times after the transfer of the exfoliated black phosphorus flakes. The sequence shows how one hour after the transfer some droplet-like structures become visible on the surface of the flakes and how they keep growing when the samples are kept in air. (b) and (c) shows the comparison of a sample right after the transfer and after two weeks in air, respectively. [5] 70
- 4.3 XRD simulated powder diffraction pattern from cif file via Reitveld refined experimental powder diffraction of BP [10] 71

4.4	Transmission electron microscopy study of few-layer black phosphorus flakes. (a) Optical image of a black phosphorus flake transferred onto a holey silicon nitride membrane. (b) High resolution transmission electron microscopy image of the multilayered region of the flake (13-21 layers). (c) and (d) are electron diffraction patterns acquired with a 400 μm spot on the thick (13-21 layers) and the thin (2 layers) region of the flake. [5]	71
4.5	(a) An AFM image of a few- layer BP sheet with a height of 2.0 nm. (b) Polar plots of the angle-resolved normalized intensities of A_g^2 mode recorded on three typical flakes with different thicknesses. (c) and (d) The SAED and HRTEM images recorded on the tri-layer BP flake [52]	73
4.6	Photoluminescence (PL) spectra of thin-layer phosphorene. (a) PL spectra of 2L, 3L, 4L, and 5L phosphor- ene. (b) Energygap of 2L, 3L, 4L, and 5L phosphorene from experimental PL spectra and theoretical simulation. (c) Layer dependence of PL peak intensity that is normalized by layer number. [108]	74
4.7	Exciton photoluminescence with large in-plane anisotropy. a, Polarization-resolved photoluminescence spectra. The excitation 532 nm laser is linearly polarized along either x (grey curves) or y (blue curves) directions.. b,Photoluminescence peak intensity as a function of polarization detection angle for excitation laser polarized along x (grey), 45° (magenta) and y (blue) directions. Solid lines are fitted curves using a $\cos 2\theta$ function (θ denotes the angle between the x axis and the polarization detection angle). c, Top view of the square of the electron wavefunction of the ground-state exciton in monolayer black phosphorus. Because the carriers are more mobile along the x direction with low effective mass and the Coulomb interaction is isotropic, the exciton is anisotropic, forming striped patterns as shown. The white spot at the centre represents the hole. Scale bar, 1 nm. [92]	75
4.8	Phosphorene crystalline orientation determination by polarization Raman spectra. (a) Raman spectra of a 15L phosphorene under different polarization angles. (b) Polarization dependence of A_g^1 , B_{2g} , and A_g^2 modesin a 15L phosphorene and the Raman peaks in silicon. (c) Schematic plot showing the vibration directions of A_g^1 , B_{2g} , and A_g^2 Raman modes. (d) Crystalline orientation of the 15L phosphorene flake, determined by angle-dependent Raman measurement. [108]	77
4.9	Low-temperature Raman spectra of 5L phosphorene. (a) Raman spectra of a 5L phosphorene at temperatures ranging from 20 to ?160 °C. (b) Temperature dependence of A_g^1 , B_{2g} , and A_g^2 Raman peak positions. [108]	77
5.1	[111]	79
5.2	TEM image of phosphorene nanobelt. [82]	79
5.3	Raman of mono-layer and few-layer phosphorene. a, Raman spectra of phosphorene with different number of layers. b, Atomic displacements of Raman active modes. [82]	80
5.4	[25]	80

5.5 A sodiation mechanism of black phosphorus. Here, the numbers in parentheses indicate calculated formation energies of Na_xP structures. The blue solid lines indicate cell sizes of Na_xP including 64 P atoms used in our DFT calculations, and the black insets in $Na_{0.03}P$ and $Na_{0.06}P$ structures show top views of each structure to clarify positions of Na atoms in the structures. [25]	81
5.6 (a) Valence electron charge density distribution on a (010) plane in the $Na_{0.28}P$. Here green and red atoms are P and Na atoms, respectively. (b) The charge density difference distribution along a P-P bond represented by a black dashed line in (a) and the Na-P bond represented by a red dashed line in (a). [25]	82
5.7 NEB calculations on diffusion barriers of a Na atom in black phosphorus (solid symbols) and on a phosphorene single layer (open symbols). The color codes correspond to the diffusion pathways in the right figure [25]	82
5.8 Temperature dependence of the full-width at half maximum (FWHM) of the Raman phonons corresponding to the (a) out-of-plane (A_g^1) vibrational mode and (b) and (c) in-plane (B_{2g} and A_g^2) vibrational modes. A1g [44]	83
5.9 Temperature dependence of the Raman shifts corresponding to the (a) out-of-plane (A_g^1) and (b) and (c) in-plane (B_{2g} and A_g^2) vibrational modes. (d) The delta Raman shift between the B_{2g} and the A_g^1 optical modes. [44]	84
6.1 Crystal structure of BP and device structure for the thermal transport experiment. (a) Illustration of the crystal structure of BP showing the ZZ and AC axes. ZZ and AC axes correspond to the [100] and [001] direction of the orthorhombic unit cell, respectively. (b) Scanning electron microscopic image of a micro-device consisting of two suspended pads and a bridging BP nanoribbon. Thermal conductivity is measured by transporting heat from the Joule-heated pad to the other pad through the nanoribbon. (c) High-resolution transmission electron microscopy lattice image of a BP flake. (d) Selected area electron diffraction pattern taken from the area shown in c.(e) Micro-Raman spectra of a BP flake with laser polarized in parallel to the ZZ and AC axis, respectively. Scale bars, 50mm(b); 10nm (c); 20nm-1 (d). [39]	86

6.2 STEM nanosculpting of zigzag and armchair few-layer BPNRs. HAADF STEM images of an (a-h) 8.0 nm long zigzag and (i-p) 6.5 nm long armchair nanoribbon. (a,i) wr and wc are the total and crystalline BPNR widths, respectively (see also Figure S6.1). Thinning of the ribbons from (a) to (h) and from (i) to (p) was observed by using the HAADF intensity-thickness correlation for each panel along the red line X (indicated in (a) and (i); see also Figure S11). The fast Fourier transforms in the insets of (b) and (j) indicate lattice spacings of 1.65 and 2.28 Å, consistent with a_1' and a_2' , respectively. For the zigzag case, wr is initially (a) 7.2 nm and subsequently narrowed to (b) 6.0, (c) 5.7, (d) 4.6, (e) 2.8, (f) 2.2, and (g) 1.7 nm. The corresponding wc values are (a) 5.6, (b) 4.6, (c) 4.3, (d) 3.1, (e) 1.9, (f) 1.0, and (g) 0 nm. For the armchair case, the values for wr are (i) 6.3, (j) 5.8, (k) 4.2, (l) 3.1, (m) 2.8, (n) 2.5, and (o) 2.1 nm. The corresponding wc values are (i) 4.9, (j) 4.2, (k) 3.0, (l) 1.4, (m) 0.9, (n) 0.5, and (o) 0 nm. After the BPNRs break, (h) 3.5 and (p) 2.8 nm wide nanogaps remain. All scale bars in (a-p) are 5 nm. [57]	87
6.3 Calculated band structure and conductance of the ZPNRs in the presence of an applied bias voltage Δg at zero temperature. (a)-(b) $\Delta g = 0$, (c)-(d) $\Delta g = 0.1 - t_1$, and (e)-(f) $\Delta g = 0.4 - t_1$. Red curves represent the quasi-flat bands, and green lines are the Fermi energy. The width of the ZPNRs is set to $N = 20$. [55]	89
6.4 Calculated conductance and thermopower of the ZPNRs under bias voltage $\Delta g = 0.6 - t_1$ for three different ribbon widths. The temperature is taken to be $k_B T = 0.03 - t_1$ in the thermopower calculation. [55]	89
6.5 The evolution of the band gaps (PBE, G0W0), optical gap (BSE@G0W0) and first bright excitonic state as a function of the nanoribbon width. The insets show the variations of the exciton binding energy (EBE) with the ribbon width. The power law fitting curves are presented by dashed lines. Experimental data of 2D phosphorene are marked by the cross sign [7, 27]. [62]	89
6.6 Top view of electron charge density of the VBM and CBM states of the 5-aPNR and 4-zPNR. [62]	90
6.7 Electronic band structure of 2D phosphorene, calculated by DFT-PBE along the ac and zz directions. The top of the valence band is set to be zero. [62]	90
6.8 The calculated VBM and CBM states of PNRs and 2D phosphorene as a function of their width. [62]	91
6.9 Exciton exchange splitting versus ribbon width. In the inset, the exchange splitting as a function of the band gap of PNRs. [62]	92
6.10 Impact of edge defects on DOS and transmission in PNRs. The impact of edge defects is reported for (a) DOS and (c) transmission in aPNRs, and (b) DOS and (d) transmission in zPNRs. The results are shown for $W = 2.1$ nm, $L = 10$ nm, and a PED of 10% and 50%. Each panel contains results for all ($N = 50$) simulated PNRs with defects (gray line), average DOS or transmission (dashed red/blue line), and DOS or transmission for an ideal PNR (full red/blue line). [69]	93

6.11 Transport gap modulation by PED and PNR width. (a) Left panel: impact of increasing PED on EG. Right panel: increase of EG as a function of PED. Results are shown for aPNRs and zPNRs about 2-nm wide and 10-nm long. (b) Left panel: width-dependence of EG in aPNRs and zPNRs with 10% and 50% edge defects. Right panel: increase of EG in aPNRs and zPNRs with defects as a function of nanoribbon width. Each data point, except for an ideal device (PED = 0), gives an average parameter value obtained by simulating N = 50 PNRs with random edge defects. Ideal zPNRs are metallic due to the non-zero transmission around E = 0 eV, but EG is nevertheless extracted as the separation between the main valence and conduction bands to allow a comparison with zPNRs with defects that are semiconducting. [69]	94
6.12 Electron and hole transport properties in PNRs with edge defects. (a) Defect-limited mobility as a function of the nanoribbon width in aPNRs and zPNRs with a PED of 10% and 50%. The μ_{ED} is extracted at $n2D = 1013 \text{ cm}^{-2}$, i.e. the typical on state. (b) Total mobility in PNRs compared to experimental mobility in GNRs. The μ_{TOT} for PNRs is obtained by applying Mathiessen's rule to μ_{ED} (reported in this work for PED = 10%), μ_{PH} and μ_{CO} (see the main text for details). (c) Mobility-transport gap plot for electron and hole mobility in aPNRs and zPNRs. The plot also shows the simulation results for GNRs, and experimental data bulk Si, InP, and GaAs, as well as monolayer MoS ₂ , and UTB SOI with a thickness of less than 7 nm. [69]	95
6.13 Influence of edge defects and nanoribbon width downscaling on mean free path. λ as a function of energy for a PED of 10% and 50% is reported for (a) aPNRs and (b) zPNRs around 2-nm wide. Each panel in (a) and (b) contains the λ results for all (N = 50) simulated PNRs with defects (gray line) and average λ (dashed red/blue line). (c) Impact of increasing PED on λ extracted at 2 eV in aPNRs and zPNRs around 2-nm wide. (d) Width-dependence of λ in aPNRs and zPNRs with 10% and 50% edge defects. Each data point in (c) and (d) is an average λ obtained by simulating N = 50 PNRs with random edge defects. [69]	96
6.14 (a) Top view of ball-and-stick model of ZBPNRs. (b) and (c) The band structures of the 4-ZBPNR with antiferromagnetic ordering and ferromagnetic ordering, respectively. (d)–(g) Band structures of the ferromagnetic ZBPNRs with different ribbon widths. [103]	97
6.15 (a) The schematic illustration of the ZBPNR junction, where the source, the drain and the central scattering are adopted by the same ZBPNR with ferromagnetic ordering. (b) The spin-up current I_{up} and the spin-down current I_{dn} versus TL for different values of DT. (c) I_{up} and I_{dn} versus DT for different values of the source temperature TL. To [103]	98
6.16 (a) and (c) The band structures of the left panel and the right panel of the 15-ZBPNR junction; (b) the spin-dependent transmission spectra of the junction. [103]	98

- 6.17 Temperature-dependent thermal conductivity of BP nanoribbons. (a) Thermal conductivity (k) versus temperature (T) plot of BP nanoribbons axially oriented to the ZZ and AC directions, respectively. Thickness (t)/width (W) of the ZZ and AC nanoribbons are 170/540nm and 170/590nm, respectively. Error bars include the errors (B8%) from thermal conductance and sample size measurements. (b) k versus Tplots (on logarithmic scale) of ZZ nanoribbons with different dimensions; 170 (t)/540nm (W) and 310 (t)/540nmnm (W). (c) k versus Tplots (on logarithmic scale) of AC nanoribbons with different dimensions; 170 (t)/590nm (W) and 270 (t)/420nm (W). The solid lines in b and c are fitted lines by taking into account various phonon scattering mechanisms (phonon–phonon, impurity and boundary). Lengths of the nanoribbons all exceed 10mm. [39] 99
- 6.18 Thickness and orientation-dependent thermal conductivity of BP nanoribbons. Thermal conductivity of ZZ and AC nanoribbons, at 300K, as a function of thickness. Error bars include the errors (8%) from thermal conductance and sample size measurements. The lines show linear fitting of the data to guide the eye. [39] 99
- 6.19 (a) The calculated formation energy of APNRs and ZPNRs as a function of the ribbon width, and (b) the ab-initio MD results of the nearest P-P distance at the edges for the 7-APNR and 7-ZPNR at room temperature. [107] 101

List of Tables

2.1	The dependence of the fitted anisotropic factor (a/c) on the laser wavelength, the thickness of the BP sample, and the Raman modes [56].	58
4.1	Thickness dependence of the electron diffraction patterns. We display the thickness dependence of the intensity ratio between the 101 and 200 reflections. The experimental data acquired on two spots of the thin flake and one spot of the thicker area has been included for comparison. [5]	72

Chapter 1

Introduction

Low dimensional materials have become increasingly popular research interests since the isolation of graphene in (2004?) by (Novoslov). Recently, a new layered material has been the subject of research, due to the possibility of exfoliated into its 2D form. This material is black phosphorus (BP), and it will be the subject of this review. Like graphene, the 2D form of black phosphorus - called phosphorene, is mono-elemental, meaning it is composed entirely of one atomic species. This is a rare quality in 2D materials which can be exfoliated.

Phosphorene is also interesting due to its novel properties, such as a bandgap which is highly tuneable by layer number, sheet width, external stresses and electric fields. Additionally, it intermediate values of band gap and mobility compared to graphene or TMDCs, for this reason researchers often refer to BP as "bridging the gap" between graphene and TMDCs.

1.1 Layered and 2D materials

A two-dimensional (2D) material is one which is confined in one dimension, resulting in a 'sheet' of material. This can be one, or multiple atoms thick, and may be flat or puckered. Examples of 2D materials include graphene, MoS_2 and recently, phosphorene. These can be exfoliated from the bulk or grown, depending on the material, for example silicene can only be grown on a substrate (as can blue phosphorene for now). 1D materials have further confinement in another direction, examples include graphene nanoribbons and carbon nanotubes. Further dimensional confinement can result in 0D materials, or quantum dots.

Low-dimensional materials are interesting due to effects of quantum confinement. This occurs when a dimension of the material approaches the exciton Bohr radius of the bulk material. The exciton Bohr radius is the distance between an electron-hole pair. This problem becomes similar to a particle in a box situation, changing the continuous band-like distribution of allowed states into discrete energy levels, reminiscent of those found in atoms (if the dimensions are extended in one or more dimensions then the overall band structure is intact but modified). To model this particle in a box the hole typically has a negative electron mass with positive charge and the system is modelled like the hydrogen atom with the reduced mass of the

system as the mass. The exciton Bohr radius can be defined as:

$$a_b^* = \epsilon_r \left(\frac{m}{\mu} \right) a_b \quad (1.1.1)$$

Where μ is the exciton reduced effective mass, a_b is the Bohr radius=0.053nm (most probably distance between proton and electron in H atom), and ϵ_r is size dependent dielectric constant.

Further quantum confinement in black phosphorus below a 2D material is interesting due to anisotropic masses in the in-plane lattice directions. This means that different confinement effects will be observed for 1D black phosphorus depending on the orientation

The Schrödinger equation for a 2D quantum well is:

$$E_n(k_x k_y) = \frac{\pi^2 \hbar^2 n^2}{2m^* L_z^2} + \frac{\hbar^2}{2m^*} (k_x^2 + k_y^2), \psi = \phi(z) \exp(ik_x x + k_y y) \quad (1.1.2)$$

The solutions of this depend not only on the thickness of the material, but on the potential of the materials around it. If these are infinitely high then the material is isolated and the energy solutions are simple:

$$E_n = \frac{\pi^2 \hbar^2 n^2}{2m^* L_z^2}, n = 1, 2, \dots \quad (1.1.3)$$

and

$$\phi_n = A \sin\left(\frac{n\pi z}{L_z}\right) \quad (1.1.4)$$

If the material at the boundaries is not a vacuum, then there will be some tunnelling of electrons and these solutions will change accordingly.

Add in tight binding model derivations etc and Hamiltonians for black p?
Maybe talk about DFT struggling with vdw forces?

1.2 Black Phosphorus

Black phosphorus was first isolated in 2014. Since then over 150 papers have been published on the material. It has experienced a year on year growth in publications greater than that for graphene following its isolation. This is due to its interesting properties such as a tunable band gap and high hole mobilities.

Due to these exciting novel properties black phosphorene has been investigated for applications in electronics, photonics, thermoelectrics and sensing devices. Its unique anisotropy also offers the potential for conceptually new electronic and photonic devices to be produced [43].

Chapter 2

Properties

2.1 Introduction

Since the isolation of the 2D counterpart, renewed interest has been found in BP, with a range of potential applications. Additionally, researchers have undertaken in-depth characterisation, in order to better understand the 2D form. The bulk of research, however, has focused on the FL form of BP. This is due primarily to interesting quantum confinement effects when reducing dimensionality in the stacking axis. Here we describe the physical, electronic and optical, and phononic properties as well as issues with stability.

2.2 Structure

2.2.1 Bulk Black Phosphorus

Black phosphorus (BP) is a layered material, similar in many ways to graphite in terms of structure, the most noticeable difference being that each layer is puckered. Black phosphorus is strongly bonded in plane, with weak out of plane bonds, which allows the exfoliation of 2D layers, which will be discussed in detail later.

Each phosphorus atom has 5 valence electrons, unlike the four present in graphite. This gives a shell configuration of $3s^23p^3$, and each phosphorus atom bonds to three neighbouring atoms. This produces sp^3 hybridisation, similar to that seen in ammonia, leading to a puckered honeycomb lattice as seen in figures 2.1 and 2.2 [4, 13]. This hybridisation describes the merging of partially filled atomic orbital. The anisotropic structure found in BP leads to unusual mechanical, electronic and optical effects, which will be investigated below.

BP is typically studied in its orthorhombic structure, although at high pressure it can also adopt a hexagonal (rhombohedral) structure, similar to arsenic A7, which has been called 'blue phosphorus'- another allotrope of phosphorus with a direct bandgap of 2eV [4]. It can also adopt a simple cubic structure at very high pressures above 8GPa [31].

The atoms in the unit cell of BP can be described by [73]:

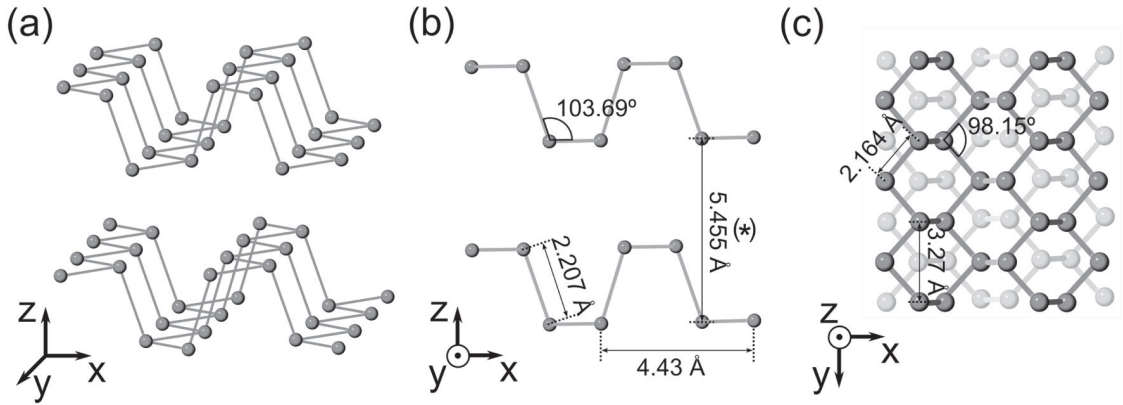


Figure 2.1: The structure of black phosphorus - note the ABA stacking order of layers. (a) 3D representation. (b) Lateral view. (c) Top view. These structures have been obtained by relaxing structures using DFT calculations. [5]

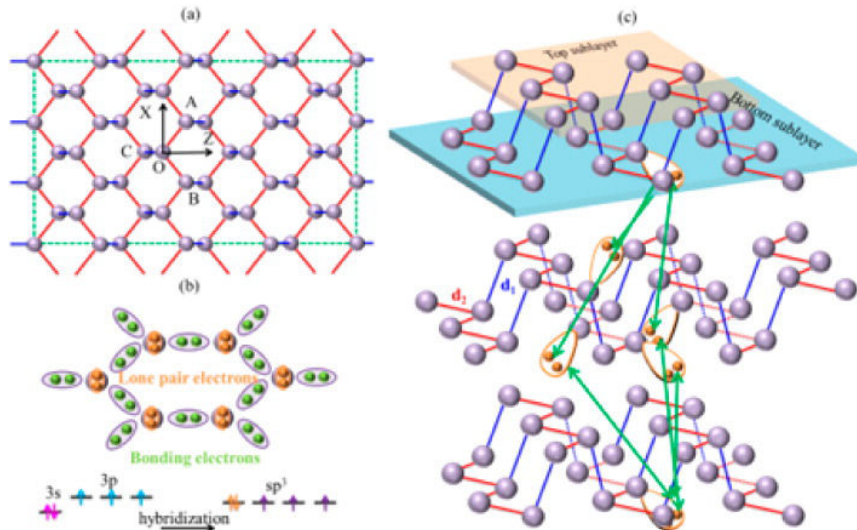


Figure 2.2: Schematics of (a) the structure of phosphorene, (b) the bonding structure and sp^3 hybridization process, and (c) the mechanism of van der Waals force formation between adjacent layers. The small yellow and green balls represent the lone pairs and bonding electrons, respectively. The separation distance between neighboring layers is approximately 5.0 - 5.5 Å [13]

$$r_{1,2} = \pm t_1 + he_y \quad (2.2.1)$$

$$r_{3,4} = \pm t_2 + he_y \quad (2.2.2)$$

Where h is a multiplier in the vertical (stacking) axis, and 2h is 2.15 Å.

$$t_1 = \left(\frac{L}{2} \cos\left[\frac{1}{2}\beta\right], 0, \frac{L}{2} \sin\left[\frac{1}{2}\beta\right] \right) \quad (2.2.3)$$

$$t_2 = \left(\frac{L}{2} \cos\left[\frac{1}{2}\beta\right] + SL, 0, \frac{L}{2} \sin\left[\frac{1}{2}\beta\right] \right) \quad (2.2.4)$$

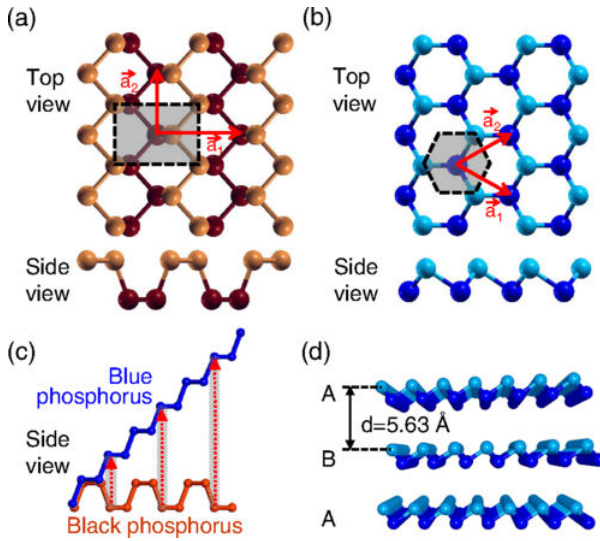


Figure 2.3: The layered structure of (a) black and (b) blue phosphorus in top and side views. Atoms at the top and bottom of the nonplanar layers are distinguished by color and shading, and the Wigner-Seitz cells are shown by the shaded region. (c) Schematic of the conversion of black to blue phosphorus by dislocations, highlighted by the shaded regions and arrows. (d) Equilibrium structure of AB stacked blue phosphorus in side view. [112]

are the in-plane vectors. This gives the form factor, given by:

$$S_K = \sum_{j=1}^{N_b} f_j \exp^{ir_j \cdot K} \quad (2.2.5)$$

as:

$$S_K = 4f_p [\cos(k_y h) \cos(\frac{t_1 + t_2}{2} \cdot k) \cos(\frac{t_1 - t_2}{2} \cdot k) - i \sin(k_y h) \sin(\frac{t_1 + t_2}{2} \cdot k) \sin(\frac{t_1 - t_2}{2} \cdot k)] \quad (2.2.6)$$

2.2.2 Phosphorene

When the layer number of BP decreases towards a 2D material, the lattice constants along the armchair (AC) direction increase and along the zigzag (ZZ) direction decrease. This is derived from an increase in bond angle seen through DFT calculations [20,53]. This change in structure, and hence in electronic and optical structure leads to interesting effects observed for few layer BP, and has sparked much interest in the research community.

Note that few layered BP has no z axis translational symmetry and so aren't CMCA crystals.

2.3 Physical and air stability

2.3.1 Physical

2.3.1.1 Black Phosphorus

Many papers have investigated the physical properties of BP, both in bulk and few layer (FL) form. This is of interest to researchers for investigating novel properties, as well as for potential applications of the materials. Here we discuss the investigated physical properties, including the sensitivity of BP to ambient conditions and

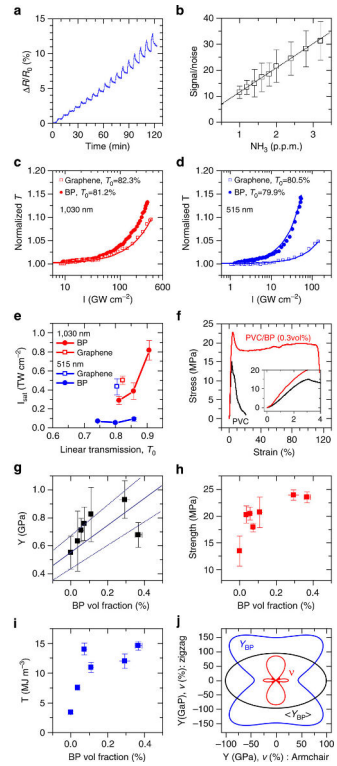


Figure 2.4: Applications of FL-BP. (a,b) Sensing of NH_3 gas using BP films. (a) Sensor response plot shows percentile resistance change versus time with a bias voltage of 1V at room temperature (b) Plot of signal-to-noise ratio as a function of NH_3 concentration from 1 to 3 p.p.m. (c-e) Saturable absorption of std-BP and graphene in CHP for femtosecond pulses excited at (c) 1,030nm and (d) 515 nm. Linear transmission T_0 is given in the legend. (e) Saturation intensity of FL-BP and graphene as a function of T_0 . (f) Representative stress-strain curves for PVC and PVC: FL-BP (0.3 vol%). Inset: low strain regime. (g-i) Young's modulus, including the theoretical constant-strain rule-of-mixtures modulus prediction (g), tensile strength (h) and tensile toughness (i) plotted as a function of FL-BP volume fraction. (j) Calculated orientation dependence of the in-plane two-dimensional Young's modulus (Y_{BP} , blue) and Poisson's ratio (n , red), of black phosphorus, together with the Voigt-Reuss-Hill averaged in-plane modulus ($\circ Y_{BP4}$, black). [24]

the impact of this on research activities.

2.3.1.2 Phosphorene

BP thin films have been shown to be efficient when used as gas sensors [24, 38]. This works by measuring the resistance change when the nanosheets are exposed to gases such as ammonia (two-probe measurements). The resistance increase seen is consistent with NH_3 donating electrons to the p-type FL-BP film. The detection threshold is estimated to be 80p.p.b. in this application.

Coleman et al. tested the mechanical properties of BP by producing a composite of PVC and BP [24]. The mechanical properties in the high and low strain regimes increase significantly when BP is in the PVC composite. The Young's modulus increases from 500MPa to 900MPa (note this is 0.3% volume of BP). The measured strength of the composite doubles whilst its tensile toughness increases sixfold. These increases compete with similar composites formed from graphene.

2.3.2 Oxidation and stability

2.3.2.1 Introduction

BP is known to be unstable in ambient conditions due to oxidation of the surface, this is attributed to the lone pair on the phosphorus atoms and high valence bond angles of an average 102 degrees [20, 45], as seen in figure 2.1. Many variations on theories for how degradation occurs in BP have been proposed, however there are

two main routes proposed.

2.3.2.2 Dominant oxidation reaction

The first is the dominant reaction occurring in BP, this occurs due to oxidation of the surface, here we discuss the components which have been investigated around this process.

Many papers have shown that surface roughness of BP increases with time, and that Raman signals which disappear or degrade are linked to this surface roughness [15, 28, 30]. Early work by Castellanos-Gomez suggests that BP has an implicit dipole moment out of plane which makes it hydrophilic, however immersion in DI and de-aerated water does not produce visible droplets, suggesting this is not correct [7, 28, 30, 45, 113]. The surface of BP is in fact only made hydrophilic following oxidation, due to dangling oxygen bonds [113]. In addition the roughness is due to 'bubbles' of liquid, and also etched regions due to oxidation. It appears that this liquid is not only water as previously thought, but also contains dissolved degradation products [28].

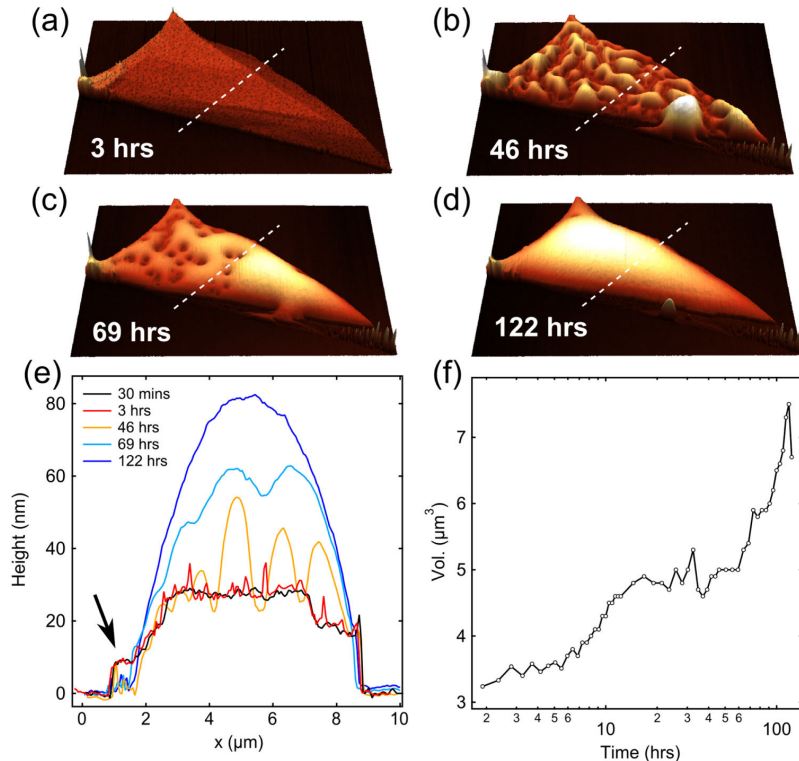


Figure 2.5: (a)-(d) Selected AFM scans of a BP flake in air taken at (a) 3 hours, (b) 46 hours, (c) 69 hours, and (d) 122 hours after exfoliation. Dotted white lines indicate the position of the line profiles shown in (e). (e) Line profiles taken across the BP flake from the scans in (a)-(d) as well as a line profile for the AFM scan taken directly after exfoliation. (f) Total volume of the flake and water over the measurement period. [30]

Favron finds that visible light alone does not induce a change, however they also see no degradation when either oxygen or water are exposed alone [17]. This is

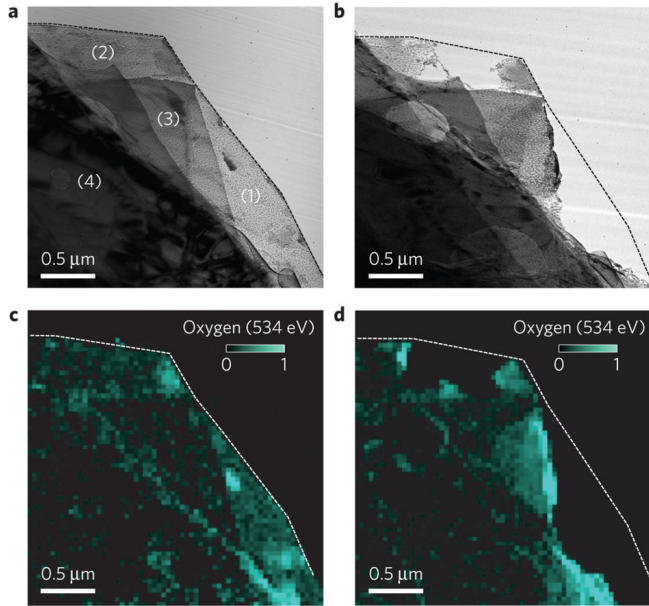
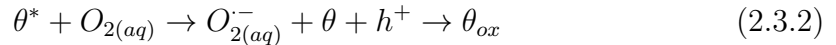


Figure 2.6: Evolution of the photooxidation reaction in ambient conditions of multilayer 2D-phosphane probed by TEM-EELS analysis. a,b, TEM images at 80kV of a flake recorded right after exfoliation in air (a) and after a further 20s in normal light (b). c,d, Energy-filtered TEM images extracted from the data cube at the oxygen K-edge (534 eV) in the same conditions as in a and b, respectively. Colour scale bars: normalized intensity relative to the maximum. [17]

different to other recent research, which suggests oxygen alone does cause degradation, however other experiments do not control for reducing ambient light. They see a slow nucleation step, but rapid exponential degradation follows. A bubble is observed with degradation around it, suggesting an initial nucleation step, then growth out from that spot.

The proposed mechanism can be described as:



i.e. optical excitation produces excitons, which then produce charge carriers at surface to transfer towards aqueous oxygen at surface. This then forms a hole in the phosphorene flake, and a super-oxide radical, which immediately oxidises the flake to form oxides [17].

Marcus-Gerischer theory (MGT) gives:

$$\frac{d\theta}{dt} = -\theta J_{ph}[O_2] \cdot \exp\left[-\frac{(|E_{g,n})|/2 + E_i - E_{f,redox}^0 - \lambda)^2}{4k_B T \lambda}\right] \quad (2.3.3)$$

where J_{ph} is the laser flux, $[O_2]$ is the concentration of oxygen in the surface water, E_i is the intrinsic Fermi level, $E_{g,n}$ is the bandgap energy of n layers flake, $E_{f,redox}^0$ is the energy level of the oxygen acceptor states and λ is the re-normalization energy of oxygen in the water. This leads to an exponential dependence on square

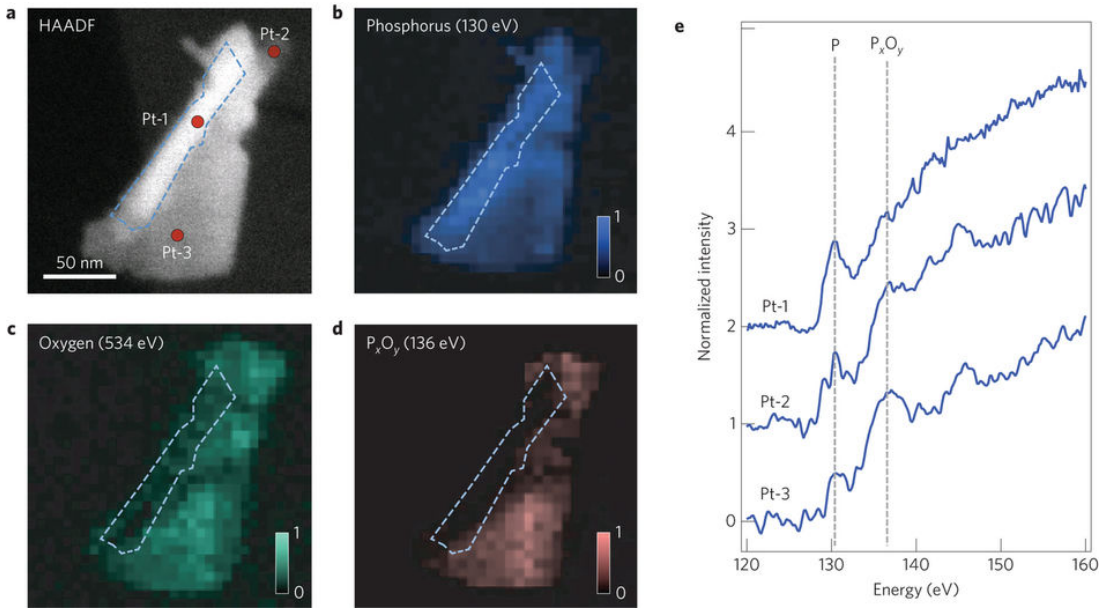


Figure 2.7: Chemical analysis by hyperspectral TEM-EELS spectroscopy of a multilayer 2D-phosphane exfoliated under ambient light in air. a, High-angle annular dark-field (HAADF) contrast image taken at 80kV. b-d, EELS images extracted from the data cube at the energy of phosphorus L_{2,3}-edge (130.2 and 136 eV) and oxygen K-edge (534 eV), as indicated. e, EELS spectra corresponding to the selected areas in a. Colour scale bars: normalized intensity relative to the maximum. [17]

of energy gap, see figure 2.8.

They suggest that water adsorption forms phosphoric acid which stops oxide accumulation, this is contradictory to other work performed by Huang [28]. They also note reducing layers increases bandgap and increases overlap with oxidation states. The MGT theory does not describe all observed characteristics, but does give an indication of some of the features and their physical basis.

Previously the bubbles seen on the surface of FL-BP were thought to be adsorbed water, this was explained due to oxidation leaving dangling O bonds on the surface and increasing hydrophilicity [28,113]. (note that Castellanos-Gomez originally suggested that BP is naturally hydrophilic). Huang has shown that water does in-fact play a role in speeding up the degradation of BP, however it does not appear to directly degrade BP [28]. This is useful as it allows the use of BP in photo-catalysis applications which require the use of water.

The droplets on the surface can be removed via vacuum [28], which supports the notion that these are liquid drops. They are removed (cannot be spotted under optical microscopy or AFM) when heated to a temperature of 250C under UHV for 2 hours which suggests they are not just water, but a liquid or dissolved species with a much lower vapour pressure than water such as P_xO_y species.

Bubbling N_2 through deionized water reduces the O_2 in the water from about 8.27mg/L at room temperature by 3-4 orders of magnitude [28]. BP held in these conditions for two days and showed no observable changes, suggesting it does not

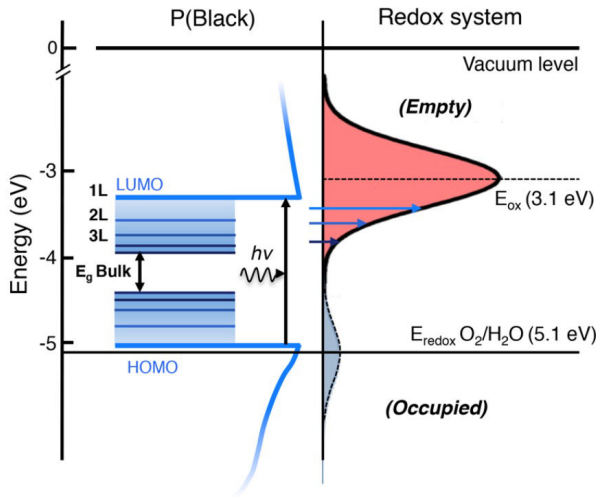
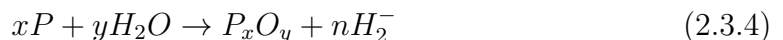


Figure 2.8: Sketch of the density of states (DOS) of aqueous oxygen acceptor and of n -layer 2D-phosphane, as predicted by Marcus-Gerisher theory. On the left: DOS of mono-, bi- tri-layer 2D-phosphane and bulk P(black). On the right: the energy diagram of the DOS of aqueous oxygen acceptor states with the enlargement of the DOS due to the solvent reorganization. The figure also illustrates by the blue arrows the proposed CT reaction induced by photo-excitation of n -layer 2D phosphane. [18]

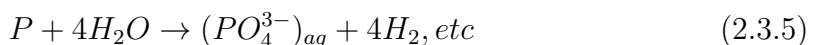
degrade in water. When bubbling O_2 through water the flakes were completely destroyed in the same number of days under identical conditions.

A mechanically exfoliated flake suspended in deionized water (non deaerated) causes degradation in 2 weeks, the thinnest parts seem to disappear, suggesting etching [28]. Note that this does not produce roughness on the surface, but a change in optical contrast (hence the etching). This is thought to be because the droplets are formed due to soluble degradation compounds. The lack of droplets on the surface here suggests that pristine BP is not actually hydrophilic.

Electron energy loss spectroscopy (EELS) performed on the degradation products suggest a shift in the P $L_{2,3}$ edge from 130eV to 136eV, and the O k edge appears at 532eV [28]. When this is performed with de-aerated deionized water there is no shift, and the P edges are all elemental, suggesting no degradation. Additionally no change in the TEM images is observed. The ratio of P: P_xO_y intensities for air and in DI water of 0.24 and 2.3 respectively suggests that water doesn't play a major role, and that oxygen is the main factor in degradation. This suggests BP cannot oxidise in water via the following reactions:



or



but instead reacts exclusively with O_2 in water and air.

FET measurements show a small increase in conductance upon initial oxidation, likely due to current annealing which lowers the contact resistance, however a de-

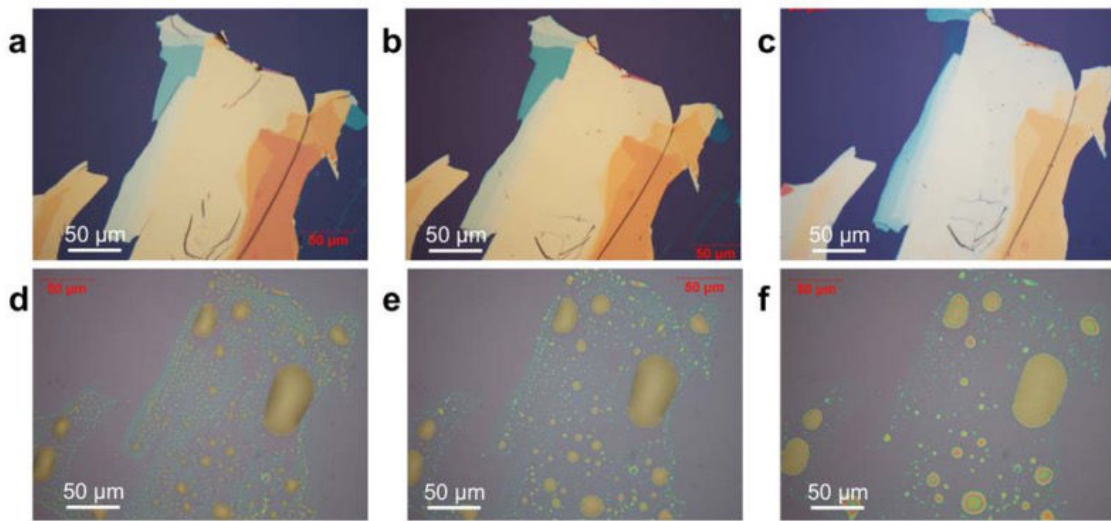


Figure 2.9: Morphology change of an exfoliated black phosphorus flake on SiO_2/Si after exposure to water and air. a. Optical images of a freshly exfoliated black phosphorus flake. b. Same flake after being submerged in DI water for 1 week. c. Same flake after a total of 2 weeks exposure to water. d. Image after removal of the flake from DI water and exposure to air for 1 week, e. Same sample after annealing at 120°C for 2 hours in ultrahigh vacuum (10^{-9} Torr). f. After additional annealing at 250°C for 2 hours in ultrahigh vacuum. [28]

crease in conductance follows [28]. DI de-aerated water as an electrolytic top gate leads to high carrier mobilities in few-layer TMDCs [29]. For BP the conductance increases from $9 \mu\text{A}$ to $41 \mu\text{A}$, this suggests that water induced impurity scattering because of screening. BP in DI water has a 6% drop in performance during the first 20 hours of operation, however this stabilises after, whereas O_2 rich water does not, this is suspected to be due to water dissolving the P_xO_y species to form phosphoric acid and allow further oxidation [15].

Edmonds investigated whether a stable oxide could be formed on BP, and used as a passivating layer, or as an interface for further dielectric deposition in FETs [15]. They note that phosphate glasses P_xO_y are transparent in the UV, and so could be used for UV applications [76, 98]. They initially showed via XPS that the P 2p core level gives an indication of the BP composition. They monitor this and see a shift indicating degradation after 2 days in air, however note that it does not penetrate into the crystal - they verify this by using more energetic photons. The average thickness of the oxide layer found was $0.4 \pm 0.3\text{nm}$, this matches the diameter of a single P_2O_5 molecule which is the most prevalent species in XPS. They also note a minimal doping effect as the work function increases by only 0.1eV (from 3.9eV).

Note this paper has some good XPS data if you want to put in specifics.

They also found that complete etching doesn't occur for the bulk crystal in air. This was confirmed via AFM. Once the liquid species on the surface were annealed off, no further etching occurred.

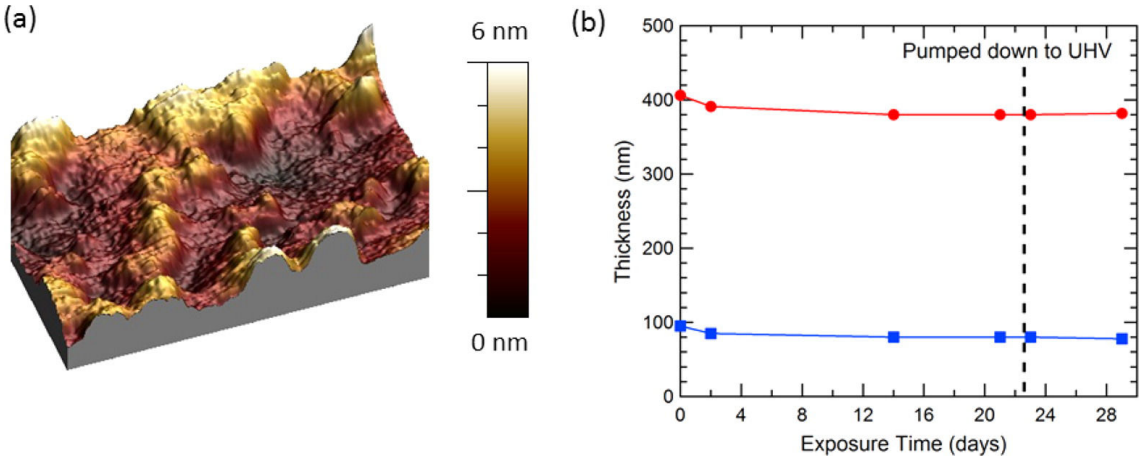


Figure 2.10: (a) AFM topography image ($500 \text{ nm} \times 500 \text{ nm}$) of oxidized black phosphorus with an RMS roughness of 1.5 nm . (b) Thickness of two exfoliated black phosphorus flakes on SiO_2/Si as a function of exposure time, where red circles represent a 406 nm as-cleaved flake and blue squares represent a 95 nm as-cleaved flake. [15]

Wang shows via DFT that O_2 interacts with phosphorene at room temperature, and that water does not, however it can dissociate when the phosphorene is already oxidised [90]. This agrees well with experimental data suggesting that the proposed reaction of oxidation followed by removal of species via dissolving in water occurs. They also note that water can adsorb to the surface of phosphorene via hydrogen bonds, even though it does not chemically bond. This is supported by some experimental data, however does disagree with some.

Utt et al performed DFT and found that dislocations in the crystal are optimal points for oxidation, and also that the curvature of phosphorene increases the oxidation rate, which in turn increases the curvature, which casts doubt on the stability of phosphorene nanotubes if they could be produced [88].

2.3.2.3 Secondary oxidation mechanism

The other proposed mechanism of degradation is not dominant for mechanically exfoliated FL-BP, however it is noticeable for solvent ex-foliated or capped BP and starts at the edges [24]. Coleman (Hanlon) finds that the photo-luminescence spectra of dispersed nano-sheets of BP does not change with time, which they correlate to a lack of degradation. It is possible therefore that the solvent ‘protects’ the nano-sheets. They also find that the smaller sheets degrade faster in the solvent, suggesting that the decomposition starts at the edges due to their smaller area. Coleman et al. do not comment on the smaller sheets also being thinner, so this potentially corresponds to previous work [17] suggesting that the degradation rate is exponentially dependent on the bandgap which scales with thickness.

Coleman also finds that increasing the water and O_2 content of the solvents increases the degradation rate significantly, this correlates well with recent work suggesting that O_2 is the biggest factor in degradation, and water acts only as a catalyst in the degradation process [28]. Coleman suggests that degradation starts

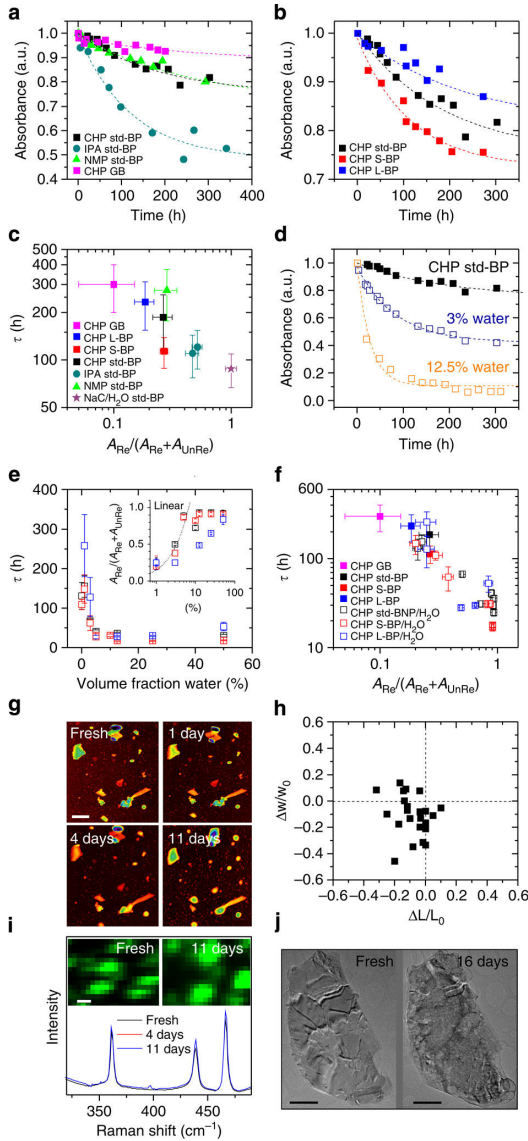


Figure 2.11: Stability of exfoliated black phosphorous nanosheets. (a,b) Relative absorbance at 465nm, measured as a function of time, for (a) the standard dispersion exfoliated in solvents labelled. (b) std-BP in CHP compared with size-selected dispersions containing small (S-BP) and large nanosheets (L-BP). The dashed lines represent exponential decays: $A = A_{UnRe} + A_{Re} e^{-\frac{t}{\tau}}$, where A_{Re} represents the component of BP, which reacts with water/O₂, A_{UnRe} represents the unreacted component and t represents the reaction timescale. (c) Reaction timescale, τ , plotted versus the fraction of BP which reacts, $\frac{A_{Re}}{A_{UnRe}} A_{Re}$, for a number of different systems. (d) Fitted time-dependent absorbance (465nm) data for std-BP in CHP and std-BP dispersions with 3 vol% and 12.5 vol% of water added. (e) Plot of τ versus volume fraction of added water. The inset shows the fraction of unstable BP plotted versus water content. (f) Plot of τ versus $\frac{A_{Re}}{A_{UnRe} + A_{Re}}$ for BP exfoliated in CHP with and without the addition of water. (g) Sequence of AFM images of the same sample region of an as-prepared sample, and after 1, 4 and 11 days of exposure to ambient conditions, respectively (scale bar, 600nm). (h) Map showing both fractional length, L , and width, w , changes as measured by AFM immediately after exfoliation after day 4. Negative values of $\frac{\Delta w}{w_0}$ and $\frac{\Delta L}{L_0}$ indicate that the nanosheets are getting smaller over time. (i) Mean Raman spectra (633nm excitation) summed over the same sample region of an as-prepared sample, after 4 days and 11 days, respectively. Inset: Raman A_g^1 intensity map of the sample region (freshly prepared and after 11 days). (j) TEM images of the same flake deposited from a freshly prepared dispersion and after 16 days. [24]

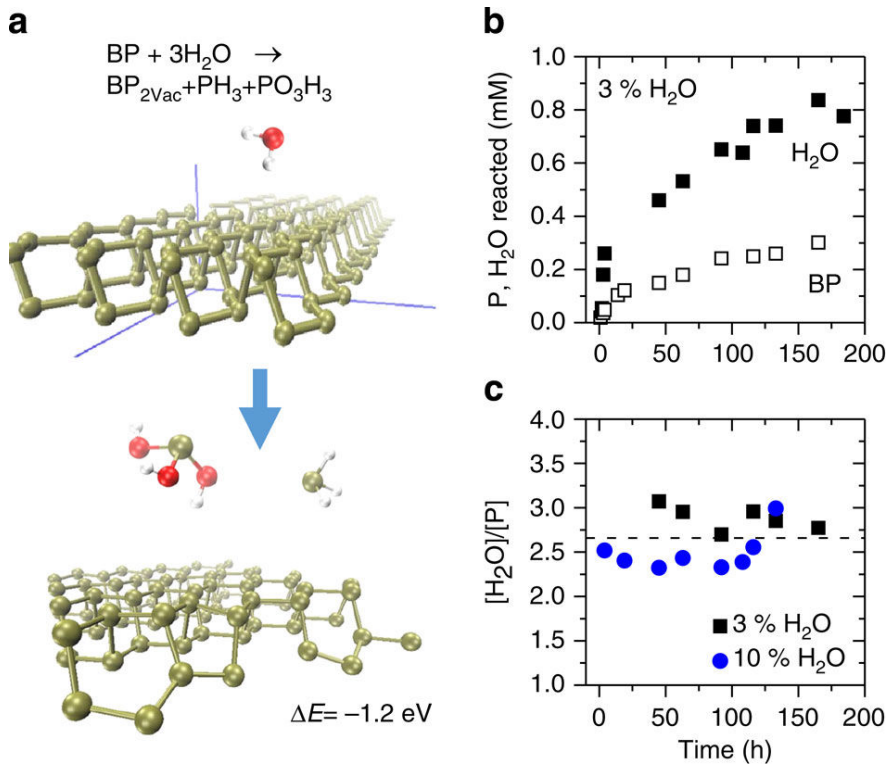
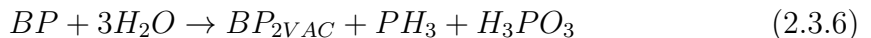


Figure 2.12: Reactivity of solvent-stabilized Black Phosphorous with water. (a) Edge selective degradation model for BP exposed to pure neutral water. Top and bottom panel represent reagent (BP edge + three water molecules) and reaction products (BP defective edge+phosphine+phosphorous acid), respectively, with the reaction energy also given. Green, red and white balls represent P, O and H atoms, respectively. (b) Experimental data for amount of reacted phosphorous and water, respectively, as a function of time for std-BP GB in CHP after addition of 3 vol% of water. The data was obtained from tracking both water and BP concentrations by ultraviolet-visible spectroscopy. (c) Molar ratio of water/ BP as a function of time measured for a std-BP GB dispersion in CHP after addition of 3 and 10 vol% of water. The molar ratio is centred at 2–3. [24]

at the edges in these solvents due to a different solvent interaction, they note that the edges show significant degradation but the central regions remain undamaged. The degradation pathway suggested is:



$\text{BP}_{2\text{VAC}}$ is a defective structure with two P vacancies in the BP super-cell. They find via considering the energies involved of forming BP vacancies that the reaction is exothermic at the edges and endothermic on the basal plane. Calculations show that BP can react with water via this mechanism. It is possible this reaction is extremely suppressed, as experiment shows deionized (DI), de-aerated water does not degrade BP [28].

The role of water was also been investigated in liquid phase exfoliation by Serrano-Ruiz [79]. They found that by adding varying amounts of water to solvents and using the Coleman method, they saw degradation of the BP for large amounts of water, and poor exfoliation for small amounts. They did not control for oxygen content so it is possible that DI de-aerated water could be a good addition

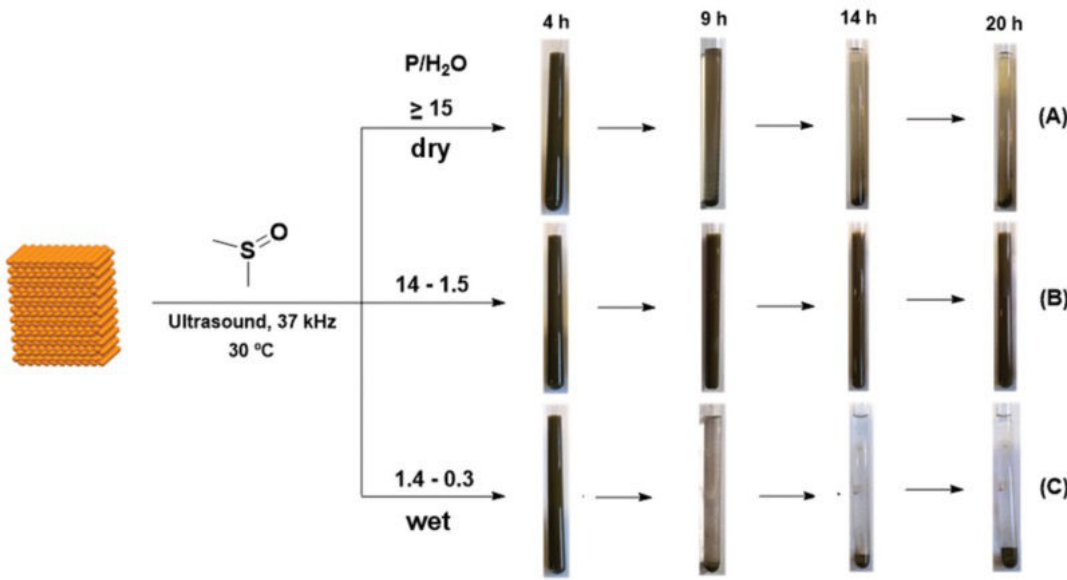


Figure 2.13: Influence of water amount in the liquid exfoliation process of BP in DMSO at different times (4, 9, 14, 20 h). [79]

to exfoliate thinner BP. They also used DMSO as the solvent which degraded the BP when pure.

2.3.2.4 Passivation

Numerous attempts have been made to passivate BP nano-sheets against environmental degradation [14, 34, 59, 66, 94]. Doganov capped BP with hexagonal boron nitride (hBN) and graphene to make FETs. They then compared the performance between capped regions and exposed regions to deduce that capping reduced the electronic degradation. They also made use of AFM and Raman spectroscopy to confirm that the surface roughness did not increase (as rapidly or severely) and the phononic structure remained intact. They did notice that after 48 hours the edges of the graphene covered regions did degrade. This is in agreement with the degradation process proposed by Coleman et al. They note that the data measured via the FETs suggests that electron traps are formed in degraded BP. This prevents the Fermi level from shifting into the conduction band under positive gating, which could be formed by oxygen point defects or the oxygen/water redox couple.

Another notable attempt of passivation was by Pei et al. [66]. They etched away at the surface of BP using an oxygen plasma, leaving a thin oxide on the surface which is stable. They then passivated this with Al_2O_3 to protect it from moisture which would degrade BP. Another is by Kim et al. [34]. They studied the effects of thin and thick capped BP with Al_2O_3 . They found that thick capped works much better than thin, but double capping with Al_2O_3 then with a DuPont Teflon-AF fluoropolymer. Others such as Wood [?] and Na [59] have investigated Al_2O_3 capping only to find that it is stable for multiple months.

Initial work on passivating BP found that in 36% humidity the flakes quickly

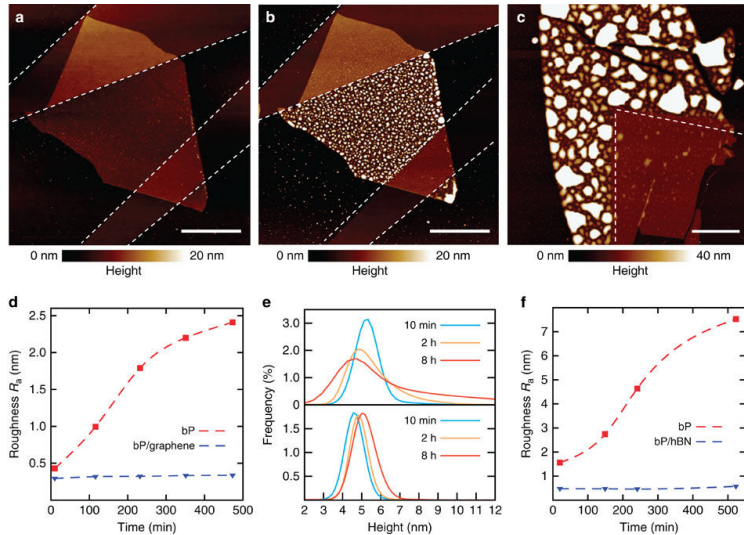


Figure 2.14: AFM study of the surface integrity of passivated and exposed BP sheets in ambient conditions. (a-b) Atomic force microscopy (AFM) scans of a 5-nm-thick bP crystal partly covered with graphene. The images are acquired, respectively, 10min and 24h after exposure to ambient conditions. The white dashed lines outline the passivating graphene crystal. (c) AFM scan of a 10-nm-thick bP crystal partly covered with hexagonal BN (hBN) after 5 days in ambient conditions. Scale bar, 4mm (for all images). (d) Average roughness (R_a) versus time in ambient conditions for the passivated (blue triangles) and exposed (red squares) bP surface of the bP/graphene sample from a,b. (e) Height distribution of the exposed (top) and encapsulated bP surface (bottom) at different times after exposure to ambient conditions for the bP/graphene sample from a,b.(f) Average roughness (R_a) versus time for the passivated (blue triangles) and exposed (red squares) bP surface of the bP/hBN sample from c. . [14]

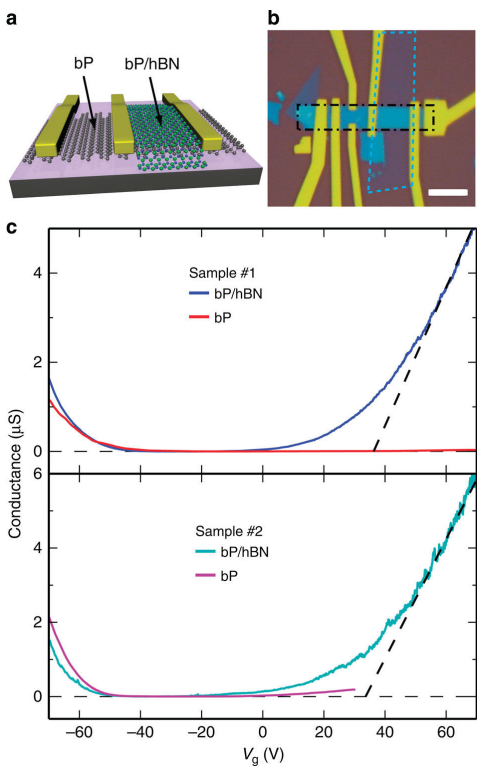


Figure 2.15: Comparison of encapsulated and exposed ultrathin BP FETs. (a) A schematic three-dimensional illustration of the device geometry. (b) Optical image of a typical device with outlines of the ultrathin bP crystal (black dashed-dotted line) and the passivating hexagonal BN crystal (blue dashed line). Scale bar, 3μm. (c) Four-terminal conductance versus backgate voltage (V_g) of the passivated and exposed channels of two bP FETs at source-drain bias $V_{sd} = 50$ mV and temperatrure $T = 300$ K. Field-effect mobilities were extracted from the line fit (black dashed line). [14]

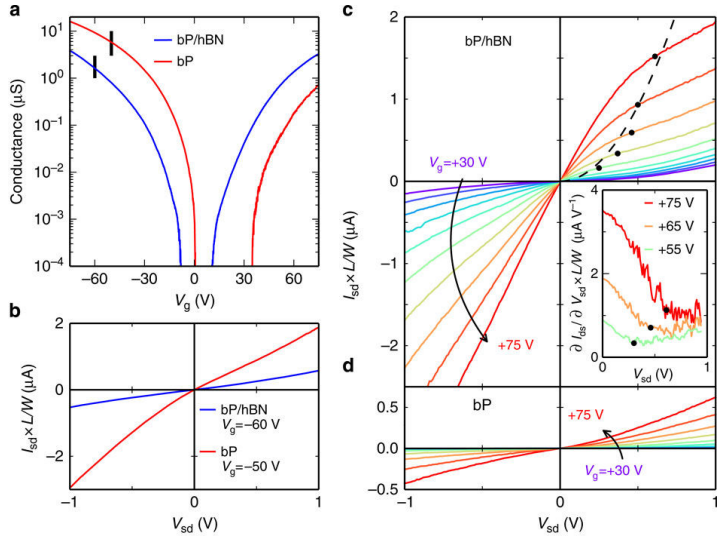


Figure 2.16: I-V characteristic of the passivated and exposed channels of a black phosphorus field-effect transistor. (a) Two-terminal sheet conductance versus backgate voltage (V_g) for the passivated (solid blue curve) and exposed (solid red curve) channel at temperature $T = 200\text{K}$. (b) I-V characteristic of the device on the hole side for the passivated (solid blue curve) and exposed (solid red curve) channel (c) Source-drain current (I_{sd}) versus source-drain voltage (V_{sd}) for the passivated channel The inset shows the output conductance qI_{sd}/qV_{sd} (d) I_{sd} versus V_{sd} for the exposed region on the electron conduction side [14]

degraded, with bubbles occurring regardless of thickness [94]. Suggesting that BP is intrinsically hydrophilic due to oxides being formed negligibly in the bulk. They find that hydrophobic substrates increase degradation rate, as water (and therefore dissolved oxygen) diffuses faster on these substrates therefore increasing the rate of degradation.

FETs were produced with deposited AlO_x which they found had a passivating effect [94]. They notice minimal degradation, although others have found that multiple capping is better [14,34]. They note that O_2 which is chemi-absorbed doesn't form P-O bonds, however interstitial O_2 may. This would cause a volume expansion and also hydrophilic dipoles which would adsorb more water to the surface!

Dielectric capping with AlO_x does increase stability, however capping this with fluoropolymer films makes the surface hydrophobic and increases the stability further. They note that without this second capping layer that the edges degrade in a similar fashion to that described by Coleman in solvents. They also noted that a very thick capping layer works well, but not as well as double capping, this is because of adsorbates diffusing through the layer. Note they use the MIM technique to measure the electrical properties and topography within 10-100nm resolution [34]. They have a GHz signal on a probe and measure the reflected signal. an get a resistance estimate from this. Note they get a new Raman peak at $800\text{-}900\text{cm}^{-1}$, which is consistent with p oxide compounds, similar to seen in doped multi wall carbon nanotubes. In the end they found that double capping had the sample last several weeks.

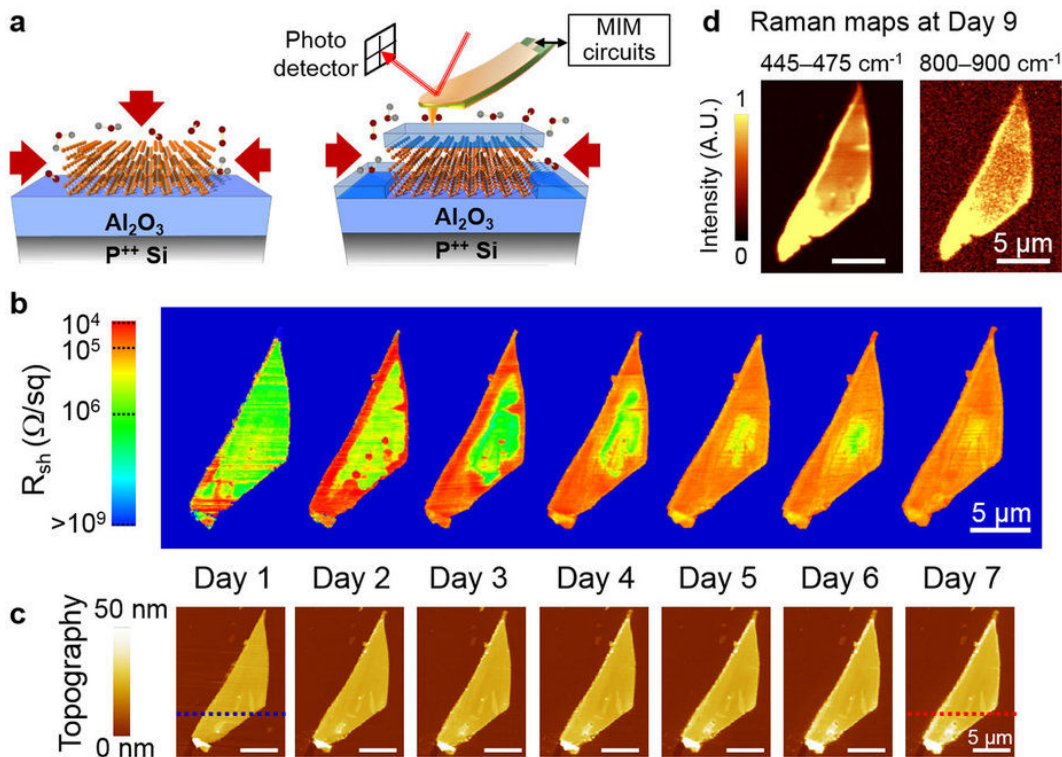


Figure 2.17: Evolution of black phosphorus with thin dielectric capping. (a) Schematics of BP samples on $\text{Al}_2\text{O}_3/\text{Si}$ substrates without (left) and with (right) a thin Al_2O_3 capping layer. Red arrows indicate the possible pathways of oxygen and moisture to react with the sample. The MIM setup is also sketched on top of the thin-cap sample. (b) Local sheet resistance maps derived from the MIM-Real data of a 24 nm-thick flake capped by 3 nm Al_2O_3 layer. (c) AFM topography of the same flake simultaneously acquired during the same time duration. (d) Raman intensity maps integrated over 445–475 cm² 1 (A_g^2 mode of phosphorene) and 800–900 cm² 1 (consistent with P-O stretching modes) measured at Day 9. All scale bars are 5 mm. [34]

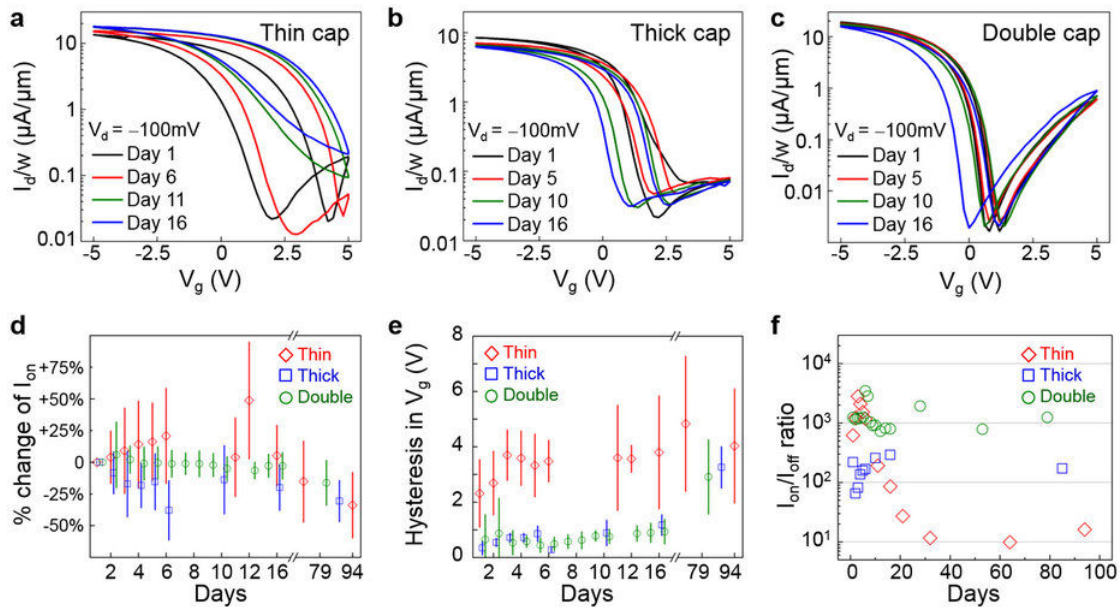


Figure 2.18: Aging of black phosphorus FETs. (a-c) I_d - V_g plot of BP devices with various capping schemes. (a) FETs with thin capping (5 nm ALD-deposited Al_2O_3) experienced significant degradation, such as reduced ON/OFF ratio and the increase of gate hysteresis. (b) Thick-cap devices (25 nm ALD Al_2O_3) showed less aging effect. (c) Devices with double-layer capping (25 nm ALD Al_2O_3 followed by DuPont Teflon-AF fluoropolymer) showed the least aging. (d-e) Statistical analysis of BP FET devices with different capping methods. (d) The change of ON current (I_{on}) with respect to the values at Day 1. (e) Hysteresis in V_g between forward and reverse sweeps. The best stability is obtained in devices with double-layer capping. (f) I_{on}/I_{off} ratio of three selected devices. Thin capped device showed sharp degradation. In contrast, I_{on}/I_{off} ratio of thick capped device was preserved to 70% compared to Day 1. Double capped device showed the best preservation of I_{on}/I_{off} ratio, with negligible change after 79 days. [34]

2.3.3 Thermal

In graphene the thermal conductivity is high due to the Z acoustic (ZA) phonon mode, i.e. the out of plane vibrations. This phonon mode contributes up to 75% of the thermal conductivity in graphene, however phosphorene has a much lower thermal conductivity, in part due to the large scattering in the ZA mode due to the puckered structure [20, 42].

The thermal conductivity in BP is much larger along the ZZ direction, due to anisotropy in sound velocities stemming from the structure [19, 21, 110]. Biaxial strain reduces the thermal conductivity, whilst uniaxial along the ZZ direction enhances the thermal conductivity whilst reducing the AC conductivity [19].

A thermoelectric device is one which utilises the Seebeck effect in order to generate electricity. These can be used in power plants, cars and space applications in order to produce electricity from thermal sources. The Seebeck effect occurs due to a heat difference shifting the electron energies in different parts of a material, thus creating a voltage which allows the flow of electricity. They operate at an atomic level in a similar manner to heat engines, and thus they have a limited efficiency. This efficiency can be characterised by the figure of merit. The figure of merit for thermoelectric devices is given by:

$$ZT = \frac{S^2 \sigma T}{\kappa} \quad (2.3.7)$$

Where S is the Seebeck coefficient, σ is the electrical conductivity and κ is the total thermal conductivity of phonons and electrons. ZT values of greater than one are needed for realistic applications [20]. It has been shown that phosphorene can possess a ZT greater than one in ambient conditions [19, 108]. A ZT value of infinity approaches the Carnot efficiency, so the higher the ZT the better for practical applications.

2.3.4 Strain and Stress

Wei showed that the Young's modulus of BP is greatest along the ZZ direction [24, 47, 93, 99]. This is due to the anisotropic nature of the crystal structure. The ZZ direction is around 4 times stiffer than the AC direction. The puckered lattice gives good flexibility, better than found in graphene or the TMDCs, additionally stresses of upto 30% can be withstood [20, 93].

It has been shown by Wei, that strain in BP (uniaxial and biaxial) can induce an indirect bandgap, or a transition to a metallic or semi-metallic state [20, 93]. In addition to modification of the band structure/band convergence, the Seebeck coefficient can also be modified.

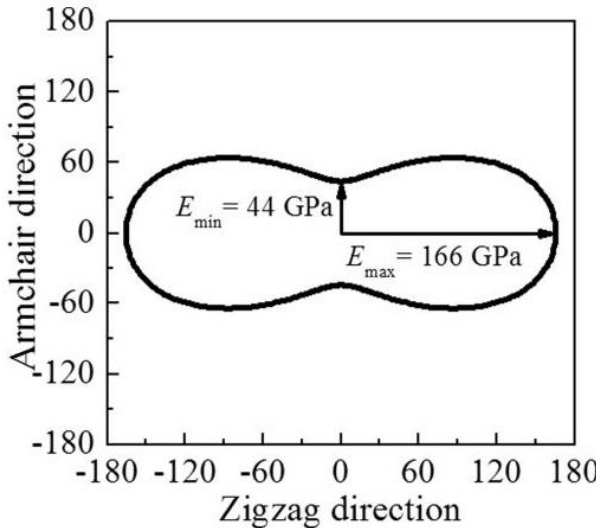


Figure 2.19: The direction dependence of Young's modulus of a monolayer phosphorene. [93]

2.4 Electronic and optical

2.4.1 Band structure

2.4.1.1 Black Phosphorus

The band structure of BP is shown in figure 2.20 [7, 91]. BP possesses a direct band gap at the Γ point of the Brillouin zone. The size of the band gap can be tuned by altering the number of layers, between 0.3eV and 2eV (with an optical binding energy of about 0.8eV for monolayer BP). The $1-5\mu m$ wavelength range is useful for applications in the near infrared (NIR), BP has a good optical conductivity in this range, which could lead to applications in thermal imaging, night vision and optical communications [4, 43].

The band structure of BP can be estimated using the LCAO method (this is not exact as it uses a finite number of Fourier terms) [20]. The LCAO calculation predicts an anisotropic band structure along the $\Gamma - X$ and $\Gamma - Y$ directions, and the effective carrier mass is lighter along the X (AC) direction. The ratio of the Y/X masses is 6.6 for electrons and 42 for holes for phosphorene, however the mass anisotropy can be reversed with a 5% tensile strain.

BP has 16 bands, split into two sets [20]. The lowest two pairs, three pairs below the gap, and three above can be regarded as the 3s, 3p and sp anti-bonding bands respectively. A large direct gap opens at the Γ point between the 3p bonding and anti-bonding bands. The dispersion of the valence band around the Γ point is anisotropic, which leads to the discrepancy in hole mass along the AC and ZZ directions, with a lighter effective mass and therefore greater conductivity along the AC direction.

(EDGE STATES??) - see electronic properties of BP paper.

The bonding-like feature of the valence band is in the interlayer region, so the overlapping of wavefunctions in this region is the origin of the interlayer interaction [20], it is also shown elsewhere that the van der Waals interaction is mostly Keesom

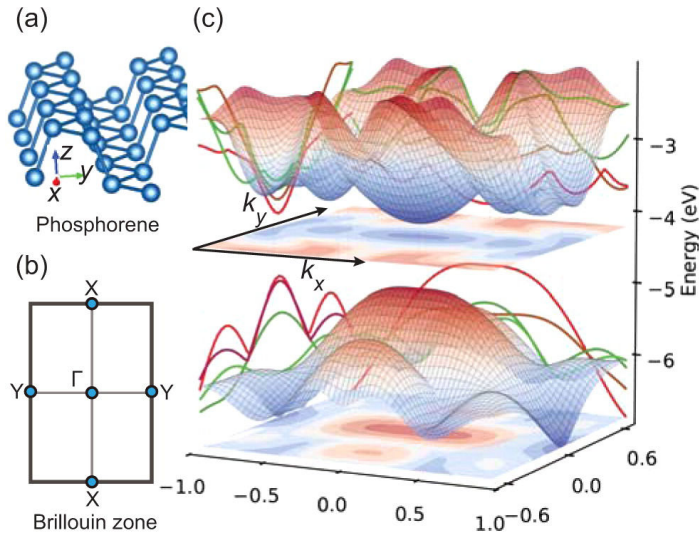


Figure 2.20: (a) Layered structure, (b) two-dimensional Brillouin zone, and (c) the highest valence and lowest conduction bands of monolayer phosphorene. Green and red curves are the projections of global band edges of the monolayer onto the xz and yz planes. The energy level of vacuum is set to zero. [91]

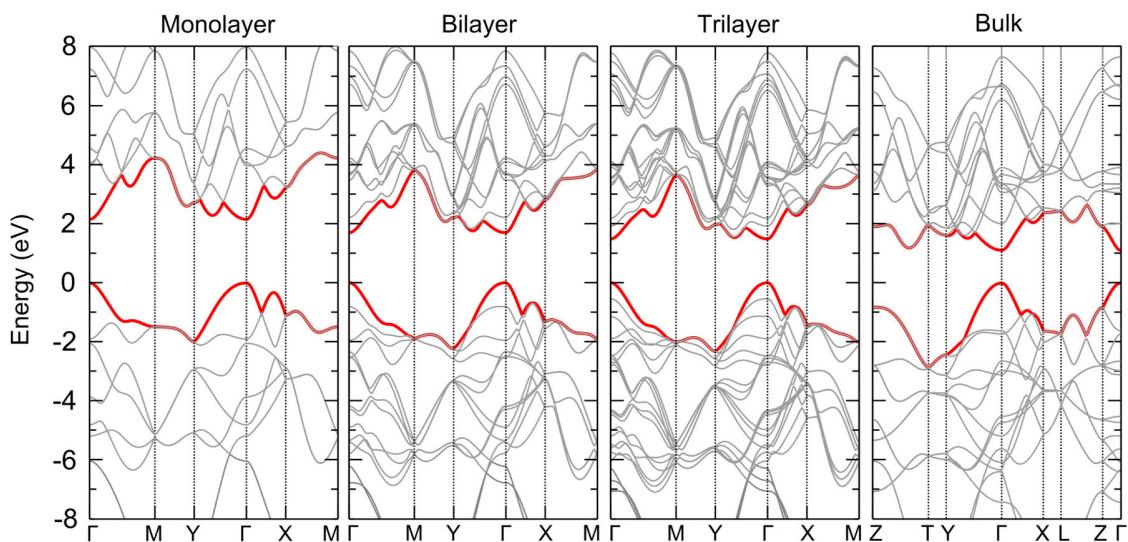


Figure 2.21: Calculated band structure. Calculated electronic band structure for monolayer, bilayer, trilayer and bulk black phosphorus sheets at all high-symmetry points in the Brillouin zone. The energy is scaled with respect to the Fermi energy E_F . [5]

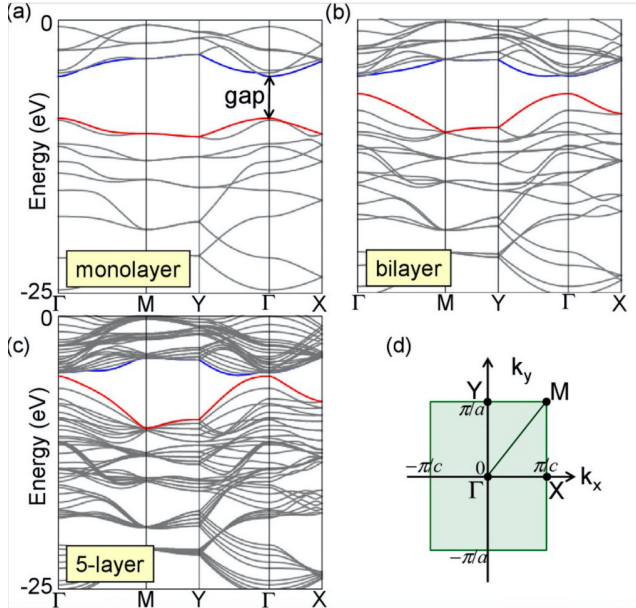


Figure 2.22: LCAO band dispersion of (a) monolayer, (b) bilayer, and (c) five-layer phosphorene. Only the nearest-neighbor and next-nearest-neighbor in-plane couplings and the nearest-neighbor interlayer coupling are taken into account. (d) Symmetric points in the 2D Brillouin zone. [20]

forces from out of plane dipole interactions [30] (see figure 2.2). This introduces a band dispersion along Z, which explains the change in band gap with decreasing layers.

The band gap also shifts with decreasing width due to quantum confinement [22, 32, 57, 87, 96, 107]. Therefore nanoribbons have been predicted to have interesting properties, AC nanoribbons (long axis is in AC direction) are predicted to be semiconducting whereas ZZ are metallic, due to the emergence of edge states. H passivated edges makes both types of ribbon indirect gap semiconductors. (The edge state is in the gap due to the merging of two Dirac cones for phosphorene, in bilayers this edge state overlaps with the valence band and so hole doping occurs ([20] and expand)).

BP is naturally a p-type semiconductor [20], it is currently unclear what the origin of the p-doping is, however it has been shown that oxidation can cause minor p-type doping [15, 30].

The puckered nature of BP layers also means that the electronic structure of one layer can be modified by a vertical electric field as there are two layers of atoms per layer [20]. There is a similar effect for transverse magnetic fields, this allows usage in FETs.

Matrices can be inserted here (Electronic structure and the properties of the phosphorene systems) and (REF).

2.4.2 Transport

2.4.2.1 Black Phosphorus

BP has been shown to have high hole mobilities in the range of $100\text{-}1000\text{cm}^2\text{V}^{-1}\text{s}^{-1}$ [12, 17, 28, 46, 60, 71, 99], and has been predicted to be as high as $10000\text{cm}^2\text{V}^{-1}\text{s}^{-1}$

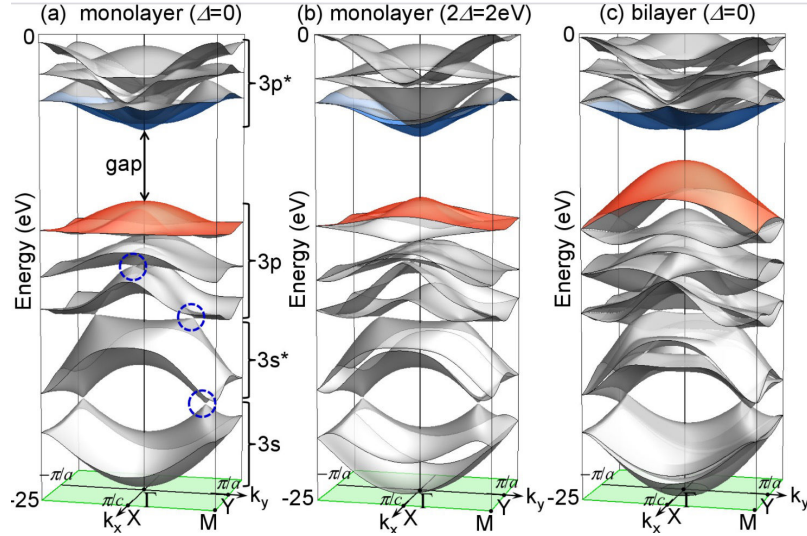


Figure 2.23: Global band structure of (a) monolayer phosphorene, (b) monolayer phosphorene under the vertical electric field, and (c) bilayer phosphorene. Several Dirac points are indicated by dashed circles. [20]

[72], or even higher at low temperatures [60]. This, combined with the large inter-layer spacing (3.08\AA vs sodium ion size of 2.04\AA) has attracted interest from battery engineers as a possible anode for sodium-ion batteries [8, 11, 25, 48, 82, 100, 101, 104–106].

In addition the on/off ratios for BP have been shown to be in the range of 100–10000, attracting interest from the FET community [36, 46, 96, 97]. There has also been interest from the photovoltaic (PV) community due to the ambipolar field effect in BP ([4, 7, 12, 45, 111]). This allows an electric field to be placed across a P-N junction made from BP with two local gates to generate electron-hole pairs via photons.

(Side note: The field effect is the modulation of electrical conductivity by applying an external electric field effect. This effect is used in field effect transistors. Band bending diagrams can be used to explain why this happens, but it is essentially due to altering the bands to change the occupancy of the conduction band of a semiconductor. If a positive voltage is applied to the material then the electrons will gain energy, which will thus mean the bands bend down in this region, which will cause the conduction band to lower towards the Fermi level. Deep into the material the field is sufficiently screened by the movement of charges that it is not 'felt', and so this is a surface effect. Note that for low voltages the valence band is lowered and so all p-type acceptors are balanced by electrons, this full occupancy screens the field and is caused a depletion zone. For higher voltages the conduction band lowering causes an increase in the number of electrons, this is called an inversion layer. Beyond a certain voltage the conduction band raises above the Fermi level and the inversion layer stops abruptly, leading to a depletion zone further in until the field is fully screened.)

The ambipolar field effect occurs in materials in which a thin film has source and drain contacts which are ohmic for majority and minority carriers exhibits n-channel

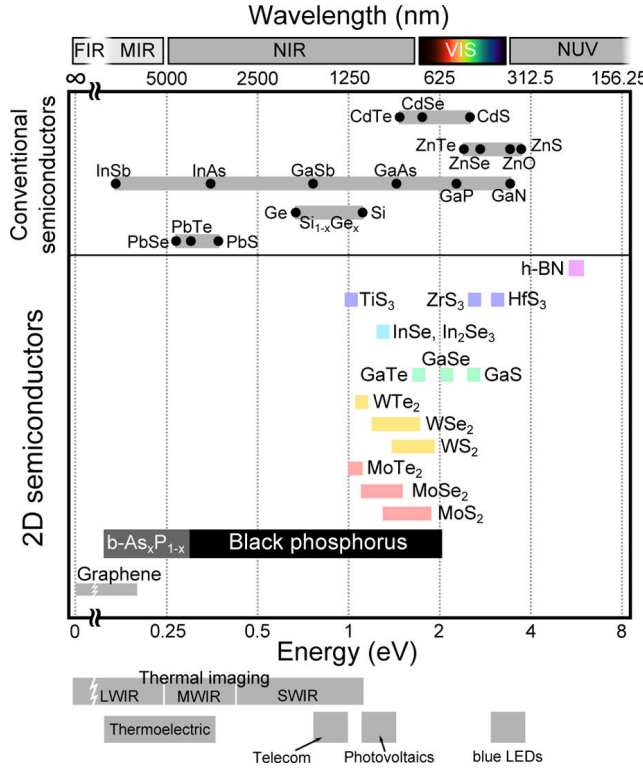


Figure 2.24: Comparison of the band gap values for different 2D semiconductor materials and some bulk semiconductors. The horizontal bars spanning a range of band gap values indicate that the band gap can be tuned over that range by changing the number of layers, straining, or alloying. In conventional semiconductors, the bar indicates that the band gap can be continuously tuned by alloying the semiconductors (e.g., $Si_{1-x}Ge_x$ or $In_{1-x}Ga_xAs$). [4]

and p-channel operations.

BP belongs to the D_{2h} point group, this leads to an effective mass of carriers along the ZZ axis 10 times larger than those along the AC axis ([1, 43] WHY!?), this is again a consequence of the unusual anisotropic structure. This could potentially lead to applications in plasmonic device, or thermoelectric applications, due to the thermal and electronic favoured conduction directions being perpendicular (ZZ and AC respectively) [20]. This anisotropy leads to a high figure of merit, ZT, which is maximised for high electrical and low thermal conductivity, see eq 2.3.7. The in plane conductivity is also much larger than the interlayer conductivity.

2.4.3 Optical

2.4.3.1 Black Phosphorus

Linear di-chroism is seen in the optical spectra along the Z axis in BP, when polarized along the X or Y directions [70]. The first absorption peak has a strong layer dependence, if polarized along X the first peak is 1.55eV for monolayer BP - increasing with layer number to 0.46eV in the bulk. For Y polarized light this is 3.14eV in the monolayer and 2.76eV in the bulk.

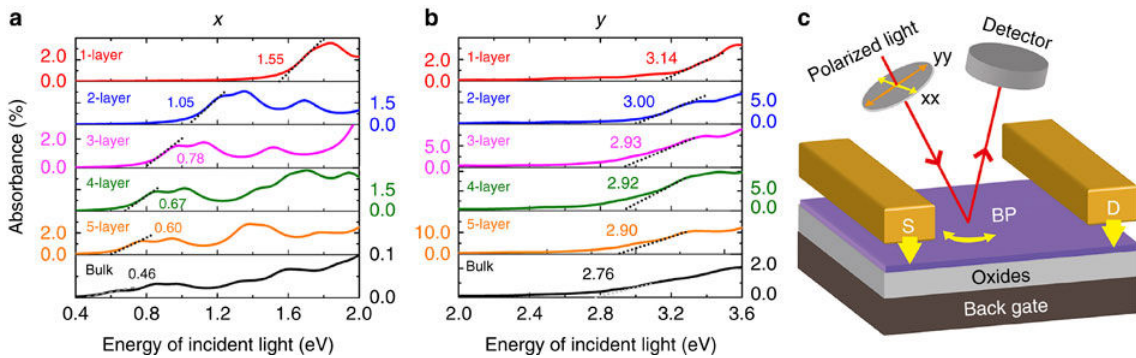


*Figure 2.25: Optical absorption spectra. (a,b) Optical absorption spectra of few-layer BP for light incident in the *c* (*z*) direction and polarized along the *a* (*x*) and *b* (*y*) directions, respectively. (c) Schematic illustration of a proposed experimental geometry to determine the orientation of few-layer BP structures using optical absorption spectroscopy, and thus to utilize the anisotropic electronic properties of BP. [70]*

In the IR spectrum BP strongly absorbs when the light is polarized along X, but is transparent with polarization along Y [70]. This is due to the dipole operator connecting valence and conduction bands for X polarization, but being symmetrically forbidden for Y polarization.

Raman and IR can make use of this anisotropy to ascertain the orientation of nano-flakes, as discussed later. The T dependence for optical spectra is around 30% higher than that in graphene, this reflects the flexibility of phosphorene [108].

In Phosphorene there is a strong layer dependence on the electronic band gap, and the optical band gap also has this dependence. Zhang et al. found via PL that the optical band gaps were 1.29eV, 0.98eV, 0.88eV 0.8eV for two to five flakes respectively. Wang et al found that monolayer BP has an optical band gap of 1.3eV. Yang also finds optical exciton energy is 0.4eV [102].

2.4.4 Superconductivity

BP has also been predicted to potentially superconduct. This has been predicted for electron-doped ($T_C = 10\text{K}$) [80], and compressed ($T_C = 10\text{K}$) [26] BP - and T_C can be increased to 17K with Li doping [78].

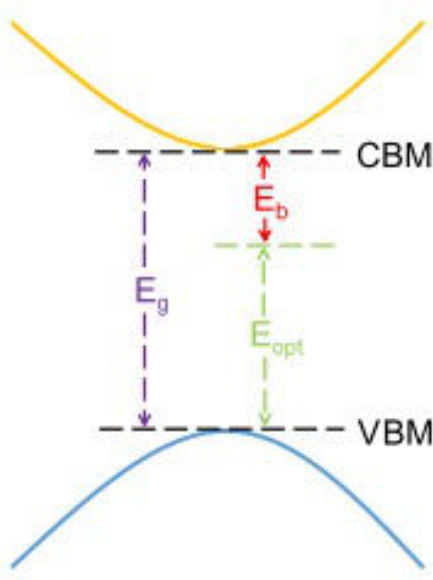


Figure 2.26: [102]

2.5 Phononic

2.5.1 Black Phosphorus

There are 4 atoms in the unit cell of phosphorene (shown in figure 2.27). There are therefore 12 phonon modes, 3 acoustic and 9 optical [20, 81]. The optical modes at the Γ point can be classified as $B_u^1, B_u^2, B_g^2, 2B_g^3, 2A_g, A_u$ and B_g^1 . These arise due to the orthorhombic symmetry of the cell. All the even parity modes are Raman active, and the odd B_u^1 and B_g^1 modes are IR active. So 12 phonon modes which are:

$$\Gamma = 2A_g + B_{1g} + B_{2g} + 2B_{3g} + A_{1u} + 2B_{1u} + B_{3u} \quad (2.5.1)$$

As seen in figure 2.28.

The acoustic phonon modes can be classified into two in-planes modes, the TA and LA, and an out of plane modes ZA [19]. The two in-plane modes have linear dispersion, and Z is parabolic. The acoustic phonon modes are anisotropic due to the structure, so the sound velocity of LA in AC direction is different than in ZZ [20]. ZZ has a larger sound velocity, which is where the anisotropy in thermal conductivity arises.

The Raman active modes [56] in BP are $A_g^1, A_g^2, B_{1g}, B_{2g}, B_{3g}^1, B_{3g}^2$. Given the usual choice of crystallographic axis, with the incident light along the stacking axis (y axis), the Raman active modes are given by [74]:

$$2A_g + B_{1g} + B_{2g} + 2B_{3g} \quad (2.5.2)$$

These can be represented in Raman tensor forms as [56, 74]:

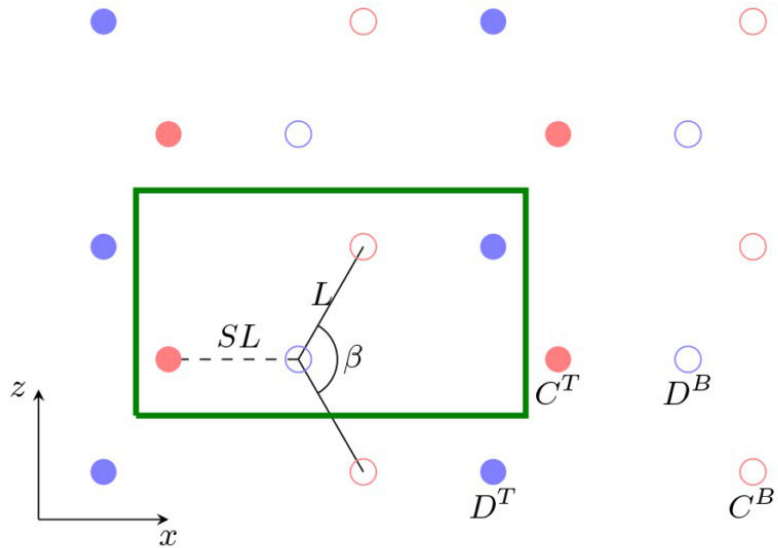


Figure 2.27: Top view of a single layer of black phosphorus, with the definition of the unit cell (green rectangle) and of the parameters to locate the basis atoms. Open (closed) circles represent the atoms at the bottom (top) part of the puckered structure. [73]

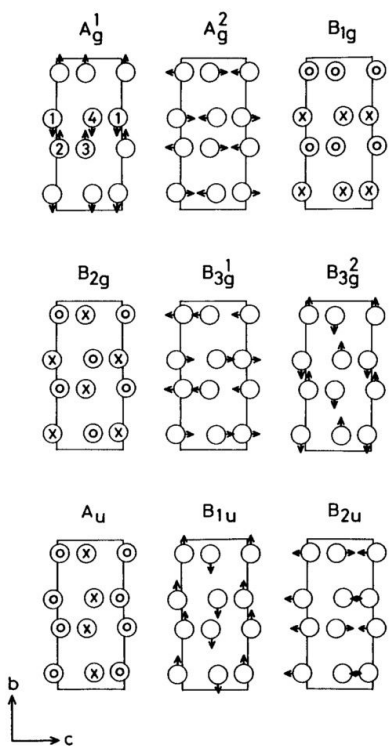


Figure 2.28: Normal modes of the Γ -point optical phonons in black phosphorous. [81]

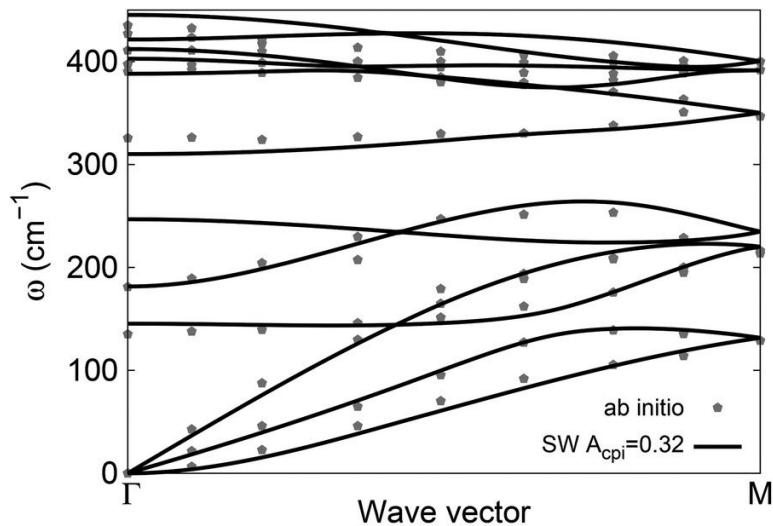


Figure 2.29: Phonon dispersion for SLBP along ΓM from the fitted SW potential is compared to the data from ab initio calculations. [33]

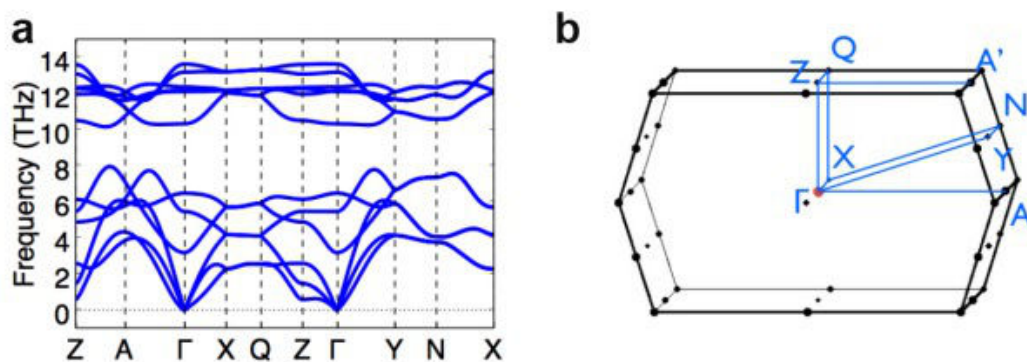


Figure 2.30: Calculated full phonon dispersion (a) Phonon dispersion along high symmetry q points. (b) The high symmetry q path in the Brillouin zone. The Γ -A and Γ -X directions are corresponding to the ZZ and AC directions, respectively. [86]

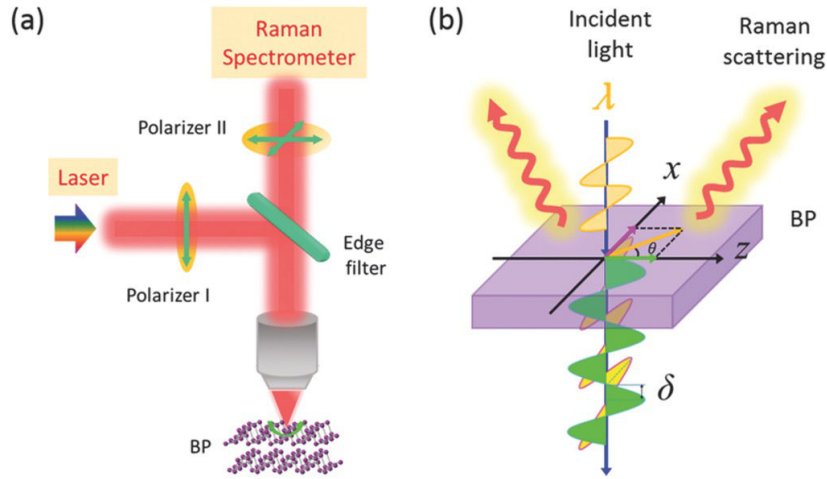


Figure 2.31: Experimental scheme and birefringence phenomenon in BP crystals. a) Schematic diagram of angle-resolved polarized Raman scattering of the BP sample. b) Schematic illustration of the birefringence effect in the BP crystal. The x and z axes are along the zigzag (ZZ) and armchair (AC) directions, respectively. θ is the angle between the AC direction and the polarization direction of the incident laser. The phase delay between the two components of the incident due to birefringence is represented by δ [56]

A_g :

$$\begin{bmatrix} a & 0 & 0 \\ 0 & b & 0 \\ 0 & 0 & c \end{bmatrix}$$

B_{1g} :

$$\begin{bmatrix} 0 & d & 0 \\ d & 0 & 0 \\ 0 & 0 & 0 \end{bmatrix}$$

B_{2g} :

$$\begin{bmatrix} 0 & 0 & f \\ 0 & 0 & 0 \\ f & 0 & 0 \end{bmatrix}$$

B_{3g} :

$$\begin{bmatrix} 0 & 0 & 0 \\ 0 & 0 & g \\ 0 & g & 0 \end{bmatrix}$$

Note that for backscattering geometry usually investigated, the Raman modes which are probed and measured are the A_g and B_{2g} modes, as these are the only two tensors with non-zero xz components (ie in-plane compared to incident and analysed light).

The Raman cross section, which gives the intensity of scattering, is given by ([56, 74]):

$$S \propto |e_i \cdot R^k \cdot e_s|^2 \quad (2.5.3)$$

The unitary vectors for incident and scattered light in backscattering geometry, along the stacking axis, are given by:

$$e_i = (\sin\theta 0 \cos\theta) \quad (2.5.4)$$

$$e_s^{\parallel} = (\sin\theta 0 \cos\theta) \quad (2.5.5)$$

$$e_s^{\perp} = (\cos\theta 0 - \sin\theta) \quad (2.5.6)$$

Ribeiro et al. investigated the unusual angular dependence of the Raman response in BP [74]. They noted that although the Raman modes had been thoroughly investigated in early work on BP, and that initial work on FL-BP had revealed the relationship between intensities and thickness, that no study on the angular dependence had been conducted.

They found that in BP it is essential to use the imaginary parts of the Raman tensors, against usual convention. This is because the phase differences in the totally symmetric modes in BP, which is an orthorhombic crystal, do not cancel out due to BP's absorption of light.

The Raman tensor is given by ([51, 54, 74]):

$$R_{ij}^k = \frac{\partial \epsilon_{ij}}{\partial q^k} \frac{\partial \epsilon'_{ij}}{\partial q^k} + i \frac{\partial \epsilon''_{ij}}{\partial q^k} \quad (2.5.7)$$

This includes the dielectric constant imaginary part due to absorption of light. This means that the Raman tensors in BP, previously given, can have their elements represented as:

$$\begin{aligned} a &= |a| e^{i\phi_a} \\ c &= |c| e^{i\phi_c} \\ f &= |f| e^{i\phi_f} \end{aligned}$$

And the phases are given by:

$$\begin{aligned} \phi_a &= \arctg \left[\frac{\frac{\partial \epsilon''_{xx}}{\partial q'_{Ag}}}{\frac{\partial \epsilon'_{xx}}{\partial q'_{Ag}}} \right] \\ \phi_c &= \arctg \left[\frac{\frac{\partial \epsilon''_{zz}}{\partial q'_{Ag}}}{\frac{\partial \epsilon'_{zz}}{\partial q'_{Ag}}} \right] \\ \phi_f &= \arctg \left[\frac{\frac{\partial \epsilon''_{xz}}{\partial q'_{B2g}}}{\frac{\partial \epsilon'_{xz}}{\partial q'_{B2g}}} \right] \end{aligned}$$

If these are used in conjunction with the formula for S, and the unitary vectors, then the complex values of S can be extracted. They are:

$$S_{A_g}^{\parallel} = (|a| \sin^2\theta + |c| \cos\phi_c \cos^2\theta)^2 + |c|^2 \sin^2\phi_c \cos^4\theta \quad (2.5.8)$$

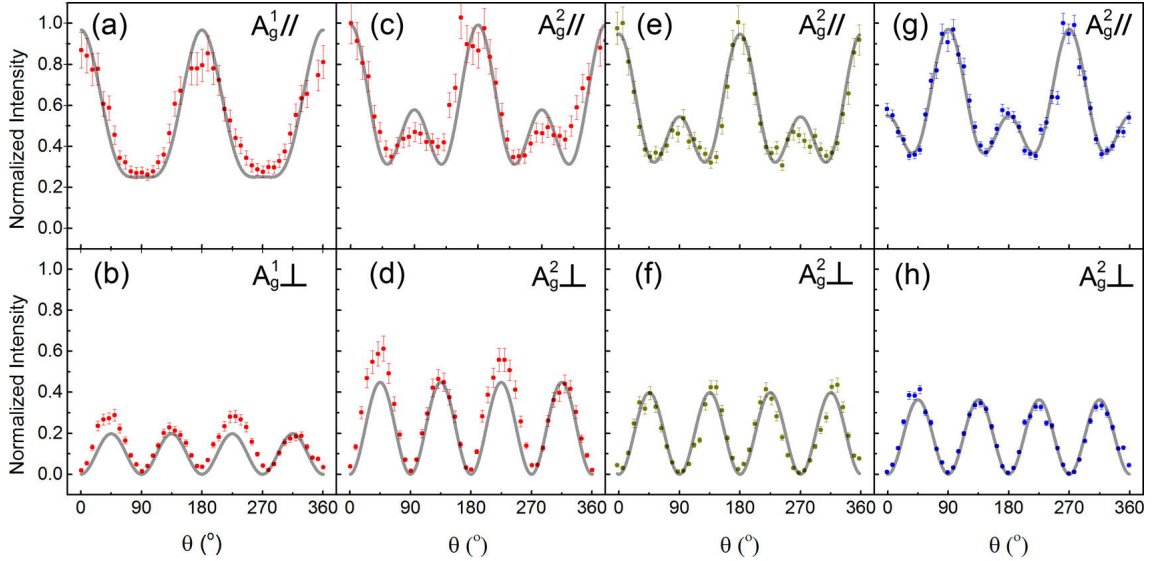


Figure 2.32: Angular dependence of the Raman intensities measured with the (a,d) 633 nm, (e,f) 532 nm, and (g,h) 488nm laser lines. The polarization configurations (parallel or cross) and the different Raman modes are indicated in each panel. Dots are experimental data, and solid curves correspond to the best fits to the data using eqs 10 and 11 for each configuration and Raman mode. [74]

$$S_{A_g}^\perp = [(|a| - |c|\cos\phi_{ca})^2 + |c|^2\sin^2\phi_{ca}]\sin^2\theta\cos^2\theta \quad (2.5.9)$$

$$S_{B_{2g}}^\parallel = (2|f|\sin\theta\cos\theta)^2 \quad (2.5.10)$$

$$S_{B_{2g}}^\perp = [|f|\cos 2\theta]^2 \quad (2.5.11)$$

Note that ϕ_{ca} is the phase $\phi_c - \phi_a$.

When these equations are fitted to the experimental data, they produce good fits. If the complex components are ignored then the A_g modes are not fitted well. The equations for the B_{2g} modes are identical to the non-complex case. This is because the phases cancel for these modes when taking the square modulus.

They also noted that there is a dependence of the Raman factors on the laser intensity.

The complex values can be traced back to the electron-phonon interactions [73]. This is because a full quantum approach (as opposed to the semi-classical approach here) is needed to account for the electron-photon interactions. When this is done the electron-photon matrices are the same for the totally symmetric modes, however they have different phases. This can only be due to the electron-phonon interaction. The full quantum description is given below:

The semi-classical model is based on the electronic polarizability tensor α . It is a second-order process, which involves only the absorption and emission of a photon.

This is explained quantum mechanically via the Kramers-Heisenberg equation for polarizability [2]:

$$\alpha(E_L) = K \sum \frac{\langle f | H_{e-r} | a \rangle \langle a | H_{e-r} | i \rangle}{E_L - E_a - i\Gamma} \quad (2.5.12)$$

where E_L is the laser energy, $|a\rangle$ is an excited state with energy E_a , H_{e-r} is the electron-radiation Hamiltonian and sum is over all intermediate states $|a\rangle$, Γ is the damping constant related to the finite lifetime of the intermediate state.

There is no implicit quantum description of the electron-phonon interaction in this equation. Instead we expand the polarizability in a Taylor's series:

$$\alpha(Q) = \alpha_0 + \alpha_1 Q + \dots \quad (2.5.13)$$

where

$$\alpha_1 = \frac{\partial \alpha}{\partial Q}|_0 \quad (2.5.14)$$

This is valid far from resonance, where the zeroth order term gives elastic Rayleigh scattering, and first order term gives Raman scattering. Therefore we have α_1 as a second rank tensor (as polarizability is too) which we call the Raman tensor. This is therefore related to the dielectric function indirectly.

The quantum mechanical approach is to describe Raman scattering as third order process, with an intermediate process of the creation or destruction of a phonon, instead of just incident photon absorption and scattered photon emission [50, 68]. This is given by:

$$\alpha(E_L) = K \sum \frac{\langle f | H_{e-r} | b \rangle \langle b | H_{e-ph} | a \rangle \langle a | H_{e-r} | i \rangle}{(E_L - E_a - i\Gamma_a)(E_L - E_b - r\Gamma_b)} \quad (2.5.15)$$

As before, with b another intermediate state.

So for this method, each element of the Raman tensor is associated with a sum that includes the matrix elements of the electron-phonon interaction term above.

The magnitude of the e-radiation elements depends on the light polarization in BP, therefore the phase is polarization dependent. So the imaginary parts of the Raman tensor are due to BPs electronic band structure, which explains which absolute values and phases of Raman tensors depend on laser energies [73].

Mao et al disagree that the complex absorption is the main factor in explaining the polarization angle dependence in BP Raman response, they instead attempt to explain this using birefringence [56]. By accounting for birefringence they alter the actual incoming and scattered light by a phase difference due to the lower velocities of E fields in some directions. This leads to a phase lag between the axes, and allows them to successfully model the A_g modes. They note that accounting for birefringence in the B_{2g} mode does not change anything, however accounting for absorbance in this mode does give a good fit. Accounting for absorbance in A_g does not show any change in the results, which is why they suggest birefringence is the main cause of the polarization dependent Raman response.

$$e_i = (\sin\theta, 0, \cos\theta) \quad (2.5.16)$$

but the E fields travel at different velocities with a phase difference δ . So the actual incident E field is:

$$e'_i = (\sin\theta, 0, e^{-i\delta} \cdot \cos\theta) \quad (2.5.17)$$

Similarly, e'_s is:

$$e'_s = R e'_i \quad (2.5.18)$$

R is the Raman tensor mode. So for Ag mode:

$$e'_s = \begin{bmatrix} a & 0 & 0 \\ 0 & b & 0 \\ 0 & 0 & c \end{bmatrix} \begin{bmatrix} \sin\theta \\ 0 \\ \cos\theta \cdot e^{-i\delta} \end{bmatrix} = \begin{bmatrix} a\sin\theta \\ 0 \\ c\cos\theta \cdot e^{-i\delta} \end{bmatrix}$$

Scattered Raman signal has the same phase difference, so:

$$e_s = \begin{bmatrix} a\sin\theta \\ 0 \\ c\cos\theta \cdot e^{-2i\delta} \end{bmatrix}$$

We can decompose e_s into parallel and perpendicular components compared to e_i , as $e_{i\parallel}$ and $e_{i\perp}$:

$$e_{i\parallel} = (\sin\theta, 0, \cos\theta) \quad (2.5.19)$$

$$e_{i\perp} = (\cos\theta, 0, -\sin\theta) \quad (2.5.20)$$

So I_{\parallel} and I_{\perp} for the A_g mode can be given by:

$$I_{\parallel} = a^2 \sin^4\theta + c^2 \cos^4\theta + 2a\cos^2\theta \sin^2\theta \cos 2\delta \quad (2.5.21)$$

$$I_{\perp} = \sin^2\theta \cos^2\theta (a^2 - 2a\cos 2\delta + c^2) \quad (2.5.22)$$

Additionally, birefringence allows an estimate of the phase lag:

$$\delta = \frac{2\pi}{\lambda} (n_z - n_x) \Delta d \quad (2.5.23)$$

which gives an indication of the main parameters which affect the Raman response, which agrees with experimental observation, although only qualitatively.

2.5.2 Phosphorene

The Raman active modes in usual geometry are:

$$2A_g + B_{1g} + B_{2g} + 2B_{3g} \quad (2.5.24)$$

These are shown in figure 2.33.

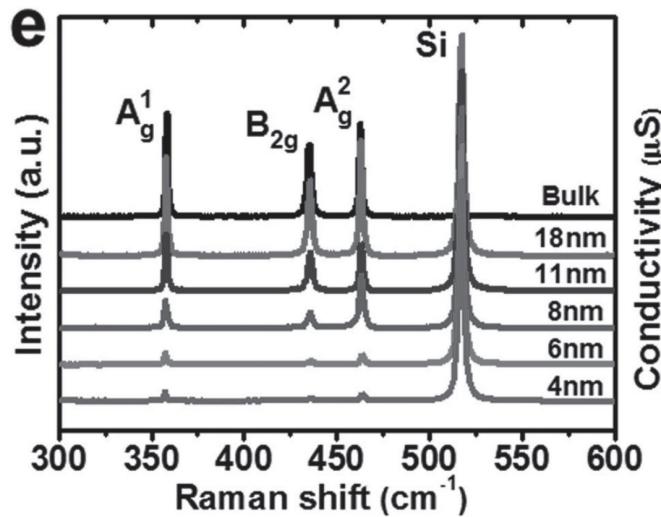


Figure 2.33: Raman spectra of BP flakes with different thicknesses [8]

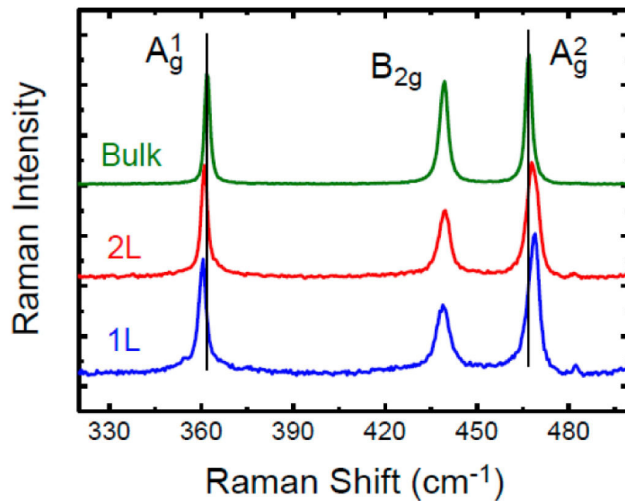


Figure 2.34: Raman spectra of single-layer and bilayer phosphorene and bulk black phosphorus films [60]

The peaks are centred at: 362.1cm^{-1} , 439.5cm^{-1} and 467.7cm^{-1} (and a silicon substrate peak seen at 520.9cm^{-1}). These correspond to A_g^1 , B_{2g} and A_g^2 phonon respectively. For decreasing number of layers, a slight shift is seen in the position of these peaks but may not be resolvable. Additionally, the intensity of the modes A_g^1 vs the silicon peak shifts in intensity linearly up to 15nm thickness, which allows the thickness to be identified, as seen in figure 2.35 [9]. Additionally the A_g^1 and A_g^2 modes also show shifts in their positions, which move together slightly with decreasing thickness, as seen in figure 2.34 [60].

This is because of stiffening of the A_g^1 out of plane mode with decreasing thickness.

Note that these peaks should be normalised against a silicon background as many factors can affect intensity. By normalising against a constant background the relevant

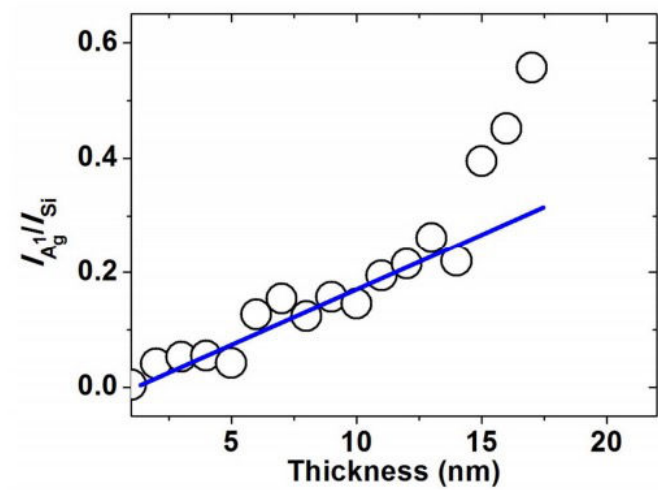


Figure 2.35: Thickness dependence of $I_{A_g^1}/I_{Si}$ [9]

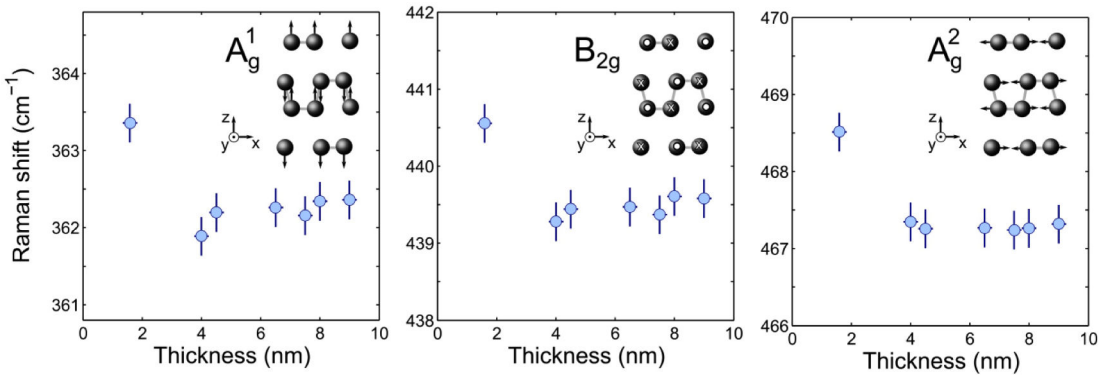


Figure 2.36: The Raman shift of the A_g^1 , B_{2g} and A_g^2 modes measured for black phosphorus flakes with different thicknesses. [6]

vant information can be extracted from the spectra. There is a small shift seen for Raman positions with decreasing figures, as seen in figure 2.36

Low frequency lasers should be used, as Kim et al. [35] found that the use of 514.5nm or longer may give varying intensity ratios due to other modes present.

Also, the anisotropy factor between the armchair and zigzag directions changes with changing thickness [56]. This is due to thickness dependence of the phase difference due to birefringence in BP discussed in section 2.5.1. This relationship is shown in table 2.1.

Table 2.1: The dependence of the fitted anisotropic factor (a/c) on the laser wavelength, the thickness of the BP sample, and the Raman modes [56].

a/c	Thin region (9.6nm)		Thick region (70nm)	
	A_g^1	A_g^2	A_g^1	A_g^2
488.0nm		2.33		1.86
514.5nm	1.29	2.05		1.47
632.8nm		1.44	0.70	0.91

Chapter 3

Synthesis

3.1 Black Phosphorus

BP is produced via vapour phase deposition of red phosphorus onto catalysts of tin and tin iodide. The red phosphorus, tin and tin iodide are sealed in a glass ampoule in an inert atmosphere, then slowly heated to 863K from room temperature. They are then kept at this temperature for 2 hours, then temperature reduced to 758K and kept at this temeprature for two more hours, then slowly decreased to 393K. Then they were cooled to room temperature naturally. These crystals grow into needle-like formations, with the long axis along the [001] (armchair) direction [37].

Zhao et al. [109] investigated this method of producing BP and tuned the parameters in order to maximise the yield and increase the crystallite size. They found by tuning the temperature and time heating, an ideal amount of BP with minimal side products can be produced.

Tellerium doped BP has been produced [3], as has lithium-doped BP via gas-phase deposition [78], however these methods only dope the surface, not the bulk.

Doping of sodium has been achieved via electro-chemistry, however the use of binders meant the material could not be recovered to be studied further than with XRD. They did confirm an increase in the stacking (b) axis of [82] 2.5 \AA .

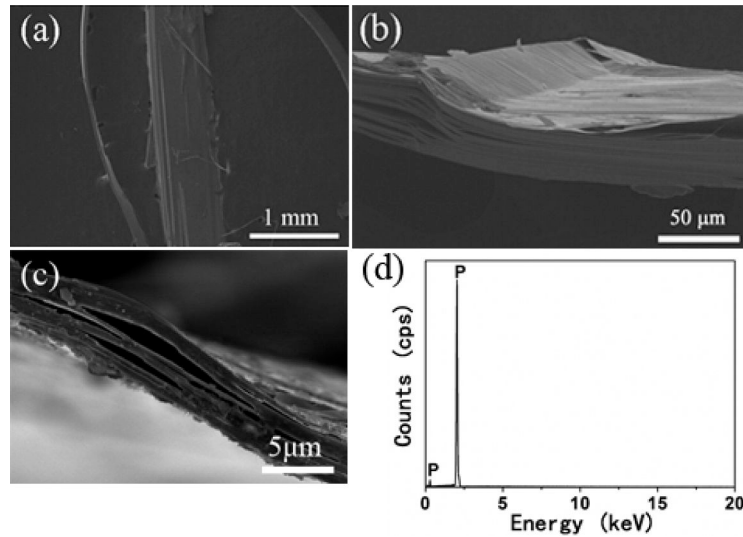


Figure 3.1: (a) Low-magnification SEM image of an individual B-P ribbon, (b) the high-magnification SEM image of the B-P ribbon, (c) the high-magnification SEM image of a thin ribbon, and (d) EDAX pattern of the grown B-P. [109]

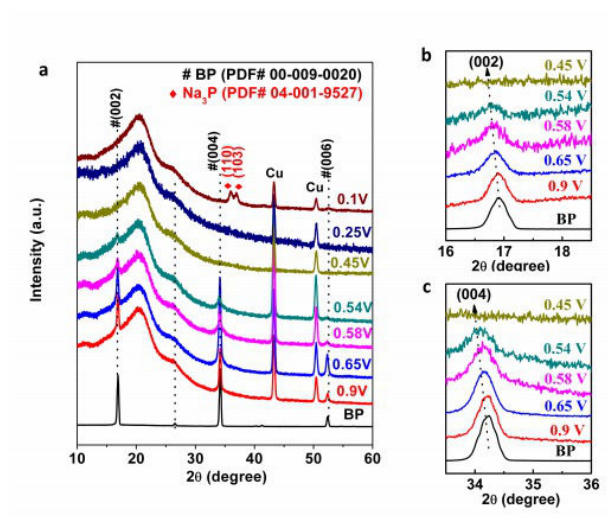


Figure 3.2: Ex-situ XRD patterns of black phosphorus taken before charging and after charging down to different voltages. a, In wide range. b, Amplification of (002) diffraction peaks. c, Amplification of (004) diffraction peaks. [83]

3.2 Phosphorene

The weak interlayer interaction in BP allows exfoliation via several methods. As with other 2D materials, the main two types of exfoliation are mechanical and liquid-phase. BP is difficult to grow epitaxially, however one group has reported this as will be discussed.

3.2.1 Mechanical

Black phosphorene is exfoliated mechanically using a small variation on the usual technique [5]. The usual method of adhesive tape left adhesive on the surface and gave a low yield. An intermediate viscoelastic surface to exfoliate the flakes increases the yield and reduces the contamination of the flakes. It is cleaved several times using blue Nitto tape, then pressed against a PDMS (poly-dimethylsiloxane) substrate and peeled off.

Favron modified this further by pressing BP onto PDMS to first exfoliated large flakes, then a spherical PDMS stamp is used to further exfoliate the flakes and transfer to a suitable substrate [18]. This technique is derived from work published by Meitl et al. [58].

3.2.2 Liquid-Phase

The Coleman method involves grounding up BP crystals and mixing with either CHP or NMP (other solvents have also been tried) [24]. These mixtures are then ultrasonicated, sheer mixed or sonicated to produce dispersion of nanosheets. TEM confirms that a bimodal distribution of widths is found (see figures 3.4 and 3.5) of 100nm and 3um, with a mean thickness of 9.4 layers for BP. In IPA the mean length is around 1um. .

The dispersions can also be filtered through alumina membranes to remove larger flakes, this is confirmed with Raman and SEM [24].

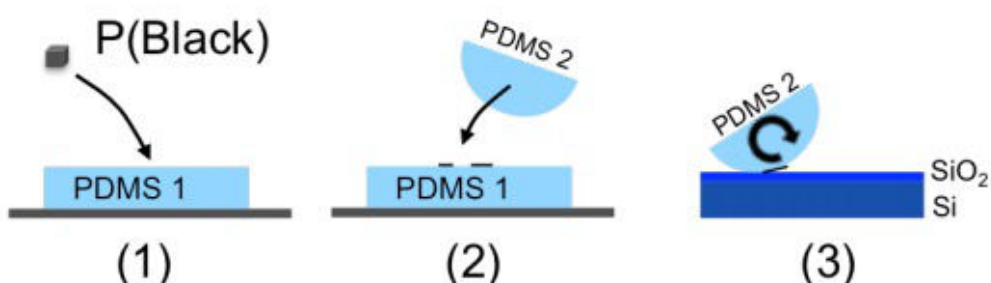


Figure 3.3: Three step exfoliation procedure of P(black). Step 1: Exfoliation done on the flat PDMS-1. Step 2: The flakes were reported on semi-spherical PDMS-2 stamp. Step 3: the stamp was rolled on the substrate (SiO₂ on Si) with an estimated speed of 0.1 cm/s. [18]

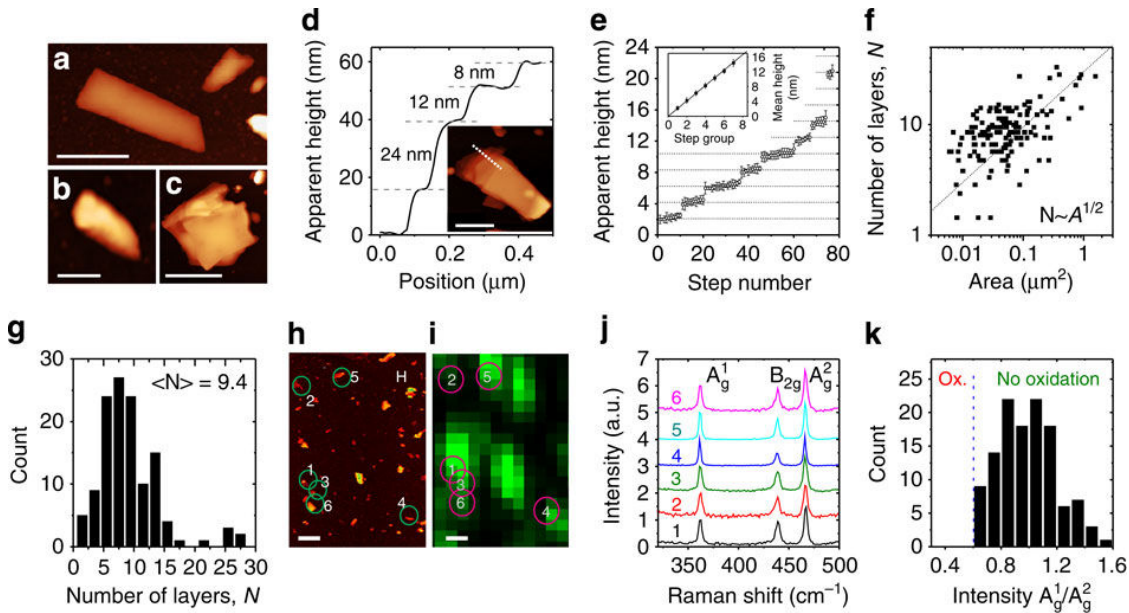


Figure 3.4: Characterization of individual nanosheets. (a-c) Representative atomic force microscopic (AFM) images (scale bars in a, b and c: are 500, 200 and 1000 nm). (d) Height profile of the nanosheet in the inset a (scale bar, 500 nm). (e) Heights of 470 steps of deposited FL-BP nanosheets in ascending order. The step height is always found to be a multiple of 2 nm, which is the apparent height of one monolayer. 2.06 ± 0.18 nm. (f) Plot of number of layers per nanosheet as a function of flake area determined from AFM. The dashed line indicates N / pA behaviour. (g) Histogram of number of monolayers per nanosheet (sample size= 126). The mean number of layers is determined as 9.4 ± 1.3 nm (h,i) Large area AFM image (h, scale bar, 1 mm) and Raman A_g^1 intensity map (i, excitation wavelength 633 nm) of the same sample region. (j) Raman spectra (normalized to A_g^2) of the nanosheets indicated in h and i. (k) Histogram of the intensity ratio of the A_g^1 / A_g^2 modes obtained from the analysis of 120 baseline-corrected spectra acquired over an area of 2525 mm^2 (sample size=120) The absence of spectra with an intensity ratio 0.6 strongly suggests that no basal plane oxidation has occurred. [24]

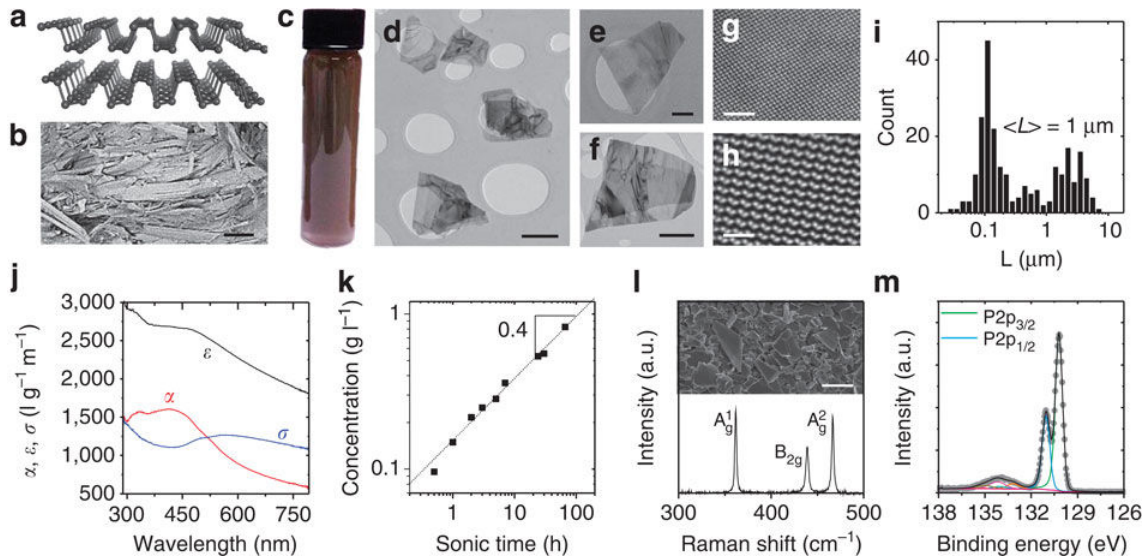


Figure 3.5: Basic characterization of exfoliated black phosphorous. (a) Structure of black phosphorus (BP). (b) SEM image of a layered BP crystal (scale bar, 100 nm). (c) Photograph of a dispersion of exfoliated FL-BP in CHP. (d-f) Representative low-resolution transmission electron microscopy (TEM) images of FL-BP exfoliated in N-cyclohexyl-2-pyrrolidone (CHP) (scale bars in d-f: 500, 100 and 500 nm). (g) Bright-field scanning transmission electron microscopy (STEM) image and (h) Butterworth-filtered high-angle annular dark field (HAADF) STEM image of FL-BP (exfoliated in isopropanol) showing the intact lattice (scale bars in g and h, 2 and 1 nm). (i) Nanosheet length histogram of the exfoliated FL-BP obtained from TEM (sample size=239). (j) Extinction, absorbance, scattering coefficient spectra of FL-BP in CHP. (k) Concentration of FL-BP as a function of sonication time. The dashed line shows power law behaviour with exponent 0.4. (l) Raman spectrum (mean of 100 spectra, excitation 633 nm) of a filtered dispersion. Inset: scanning electron microscopic image of thin film (scale bar, 2 mm). (m) X-ray photoelectron spectroscopy P core-level region. [24])

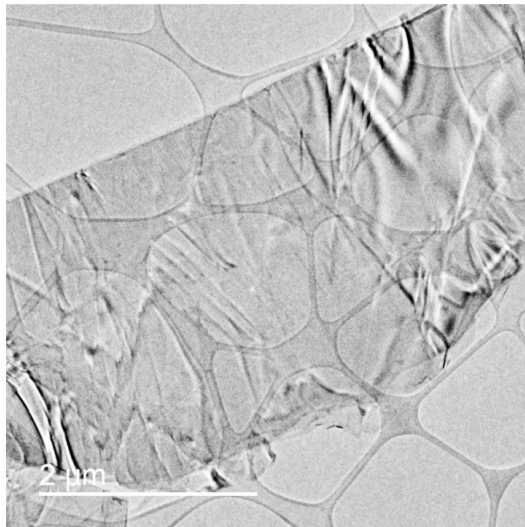


Figure 3.6: TEM image of phosphorene nanobelt. [82]

Liquid-phase exfoliation using the Coleman method by Sun et al. showed that clean cut edges are present on exfoliated phosphorene along the ZZ long axis [82]. They see nano-belt objects, microns long, which are wide but have ribbon like aspect ratios.

Woomer et al. [95] used a similar technique, but instead utilised low power bath sonication, for a period of 13 hours under an inert atmosphere. They then centrifuged at 3000g for 30 minutes to remove unexfoliated BP, and utilised further dialysis purification to remove small ($\approx 2.5\text{nm}$) BP fragments. They tested 18 different solvents, and found that the best solvent was benzonitrile, with a concentration of $0.11 \pm 0.02 \text{ mg/ml}$. They claim this method can give thin phosphorene flakes of lateral dimensions up to $50\mu\text{m}$, however no value for the thickness of these large sheets is given.

They utilised mass fractionation via centrifugation to separate larger sheets, starting at 120g up to 48000g. Finding that centrifugation at 20000g gave a dispersion of 40% monolayers, as seen in figure 3.7. Thin flakes which were displayed in the data have lateral dimensions of ca. 500nm, however it is not clear from the data how thin the larger flakes they observed were. The data indicates that above 120g centrifugation they appear to get no flakes with linear dimensions larger than $3\mu\text{m}$.

3.2.3 Growth

Thin film growth has been achieved by growing a thin film of red phosphorus, and then applying pressure to induce a transition to black phosphorus, yielding a film of thickness 40nm (which may potentially be improved to 5nm) with grain sizes of the order of 10nm [41]. The drawback of this technique is that the reported domain size is much smaller than that from other techniques.

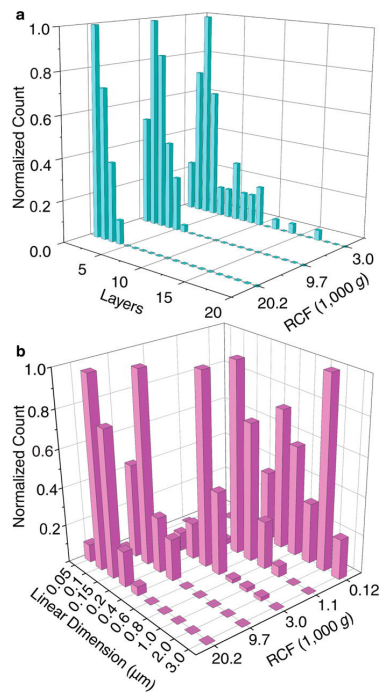


Figure 3.7: Selective variation of the centrifugation rate allows for control over flake thickness (a) and flake lateral size (b). [95]

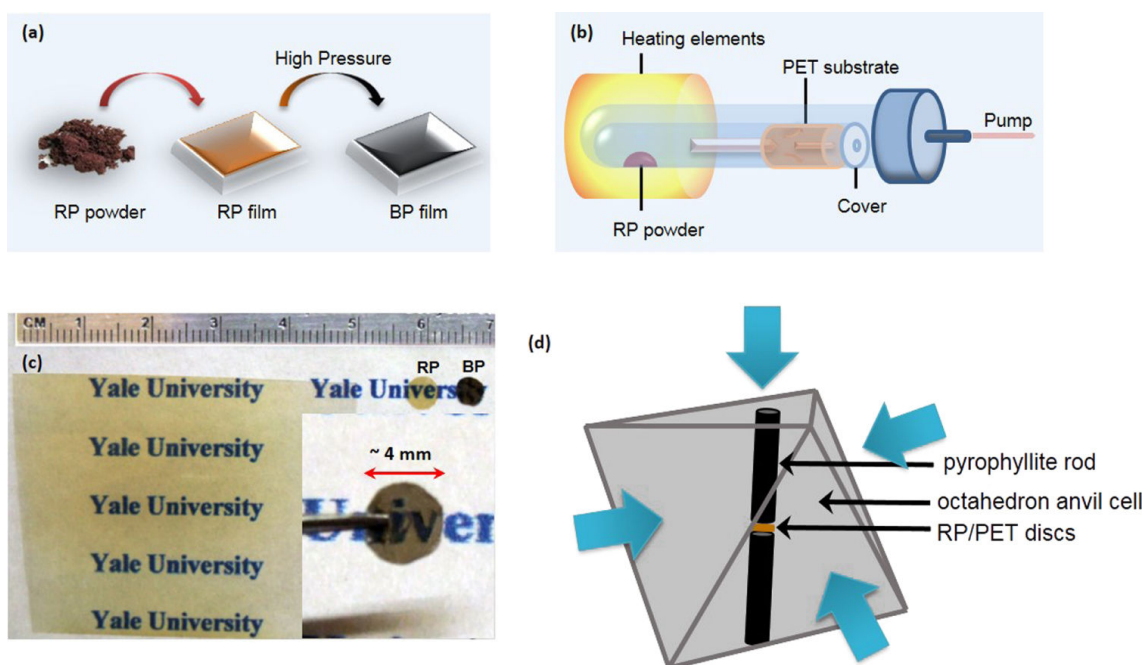


Figure 3.8: (a) Strategy for the synthesis of thin BP films. (b) Schematic apparatus for the deposition of RP film. (c) Photos of thin RP film on PET substrate (left), RP/PET disc for pressurization (middle) and BP/PET disc after pressurization. (d) Schematic of the high pressure anvil cell for conversion. The arrows indicate the directions along which the pressure is applied in conversion process. [41]

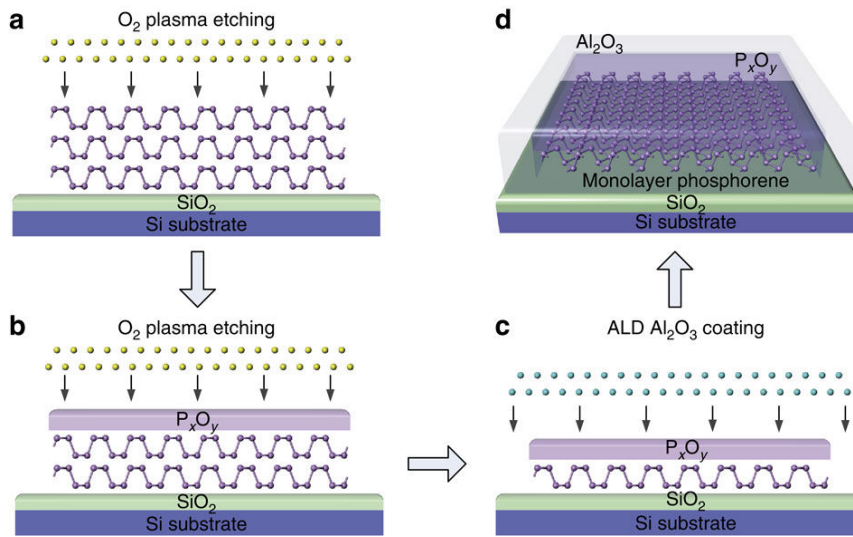


Figure 3.9: Schematically showing the fabrication of air-stable mono- and few-layer phosphorene samples. (a) A thick phosphorene flake is firstly exfoliated onto a SiO_2/Si substrate and the sample is then treated with O_2 plasma etching (yellow balls). (b) During the O_2 plasma pre-treatment process, the top layers of the phosphorene flake are oxidized to become P_xO_y , which then serves as a protective layer for the remaining phosphorene sample underneath. With further O_2 plasma etching, oxygen plasma can penetrate the P_xO_y layer by diffusion and oxidize the underlying phosphorene, and this thins down the phosphorene layer and also increases the thickness of the P_xO_y . Meanwhile, the O_2 plasma physically sputters away the P_xO_y layer from the top because of the collisions by oxygen plasma. After the plasma pre-treatment, a dynamic equilibrium is reached between oxidation of the phosphorene and physical removal of the P_xO_y layer, such that the P_xO_y layer approaches a constant thickness and the etching rate also becomes constant. (c) Because of the constant etching rate, any designated number of layers of phosphorene down to a monolayer can then be precisely fabricated and the degradation of the remaining layers is inhibited because of the protective nature of the P_xO_y . (d) To further improve the lifetime of the phosphorene sample, the sample was also coated with an Al_2O_3 protective layer by ALD. In this case the P_xO_y layer prevents the underlying phosphorene from reacting with the precursor gases used in the ALD process, which is especially important for samples less than a few layers thick [66]

3.2.4 Etching

Pei et al. utilised the stable oxide on BP by developing a technique to produce monolayer phosphorene using an oxygen plasma [66]. They use this plasma to oxidise the surface, and then etch the oxidised BP away, this results in a stable rate of etching and leaves a thin (11nm) layer of oxide on the surface. They show this can be used to engineer defects by over-etching the surface, and allow controllable production of few-layer BP, with small changes in PL and Raman intensities, although their techniques were not rigorous enough to prove that the monolayers behaved as pristine BP.

Chapter 4

Characterisation

4.1 Introduction

Here we discuss the techniques and key results relevant to characterisation of BP. The main characterisation sections fall into: physical, electronic and optical, and phononic. The focus here is on technique specific properties which can aid researchers and key results relating to characterisation.

4.2 Physical

4.2.1 Introduction

Here some of the physical characterisation techniques of BP are discussed, AFM, the Young's modulus, and diffraction is discussed.

4.2.2 AFM

AFM can be used to characterise flake thickness, however often the minimum height on AFM is found to be larger than expected, and this may be due to adsorbed solvent on the layers and capillary forces and adhesion [24,61,65,75]. This is especially prevalent in liquid phase exfoliation experiments, where damage or adsorbed liquid gives a layer thickness larger than that of a single layer, see figure 3.4 for an example.

4.2.3 Optical Microscopy

Transmission mode optical microscopy can be used to identify the thickness of large sheets, usually found via mechanical exfoliation. This relies of the use of multiples of % light transmission, with the common multiple being attributed to the monolayer.

Bright field optical microscopy can also be used to identify/spot larger flakes. This works based on the interference principle, usually using Si/ SiO_2 substrates. The light reflects from multiple boundaries, through materials with different refractive indexes and dielectric constants (plasma frequencies?). This means a thin enough layer of material causes interference which shifts the contrast/colour compared to the substrate alone, allowing thin flakes to be easily identified. Further

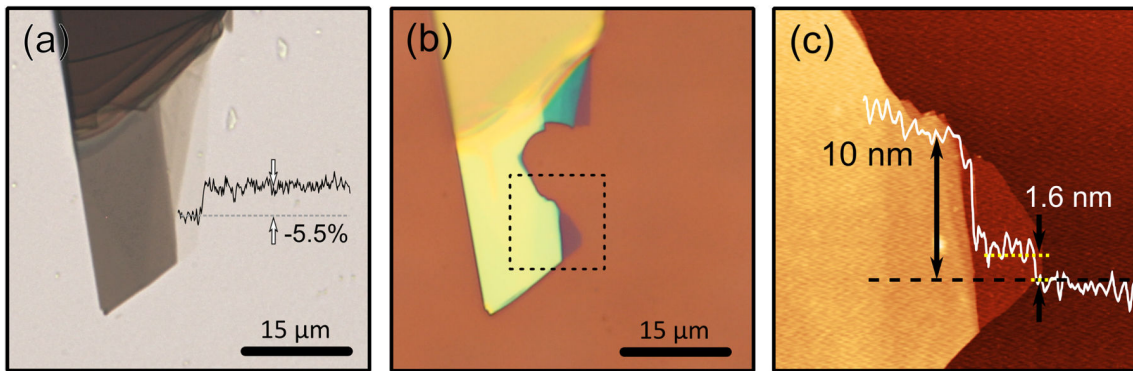


Figure 4.1: Isolation of few-layer black phosphorus flakes. (a) Transmission mode optical microscopy image of a few-layer black phosphorus flake exfoliated onto a PDMS substrate. An optical transmittance line profile has been included in the figure to highlight the reduction of about 5.5% in the optical transmittance in the thinner part of the flake. (b) Bright field optical microscopy image of the same flake after transferring it onto a SiO_2/Si substrate. Note that part of the flake was broken during the transfer. (c) Atomic force microscopy topography image of the region highlighted with a dashed square in (b). A topographic line profile, acquired along the horizontal dashed black line, has been included in the image. [5]

detailed analysis of this technique can identify monolayers, however it is much more complex than transmission mode microscopy or AFM, although tabulated values for common materials are available which make it significantly easier [40, 77]. For few layer BP 275nm of SiO_2 on Si gives the right contrast to be identified via optical microscopy [108]. This allows mechanical exfoliated BP to be identified using optical microscopy.

Yang [102], uses optical path lengths to find the thicknesses of flakes.

$$OPL_{BP} = -\frac{\lambda}{2\pi}(\phi_{BP} - \phi_{\text{SiO}_2}) \quad (4.2.1)$$

even with flakes less than 1nm, the effective path length is over 20nm due to multiple interfacial light reflections.

4.2.4 Young's Modulus

The Young's modulus has been investigate via calculations [89, 93], as well as experimentally [24]. Note that the Young's modulus was measured experimentally as an increase in the Young's modulus of a plastic composite, increasing from 500MPa to 900MPa for 0.3% volume composite with PVC.

4.2.5 Diffraction

XRD experiments of synthesised BP at 1.2GPa and 1100K (using a different method to current commercial production) have taken place [10]. Rietveld refinement of the data lead to the lattice parameters and unit cell that is often used in BP literature today.

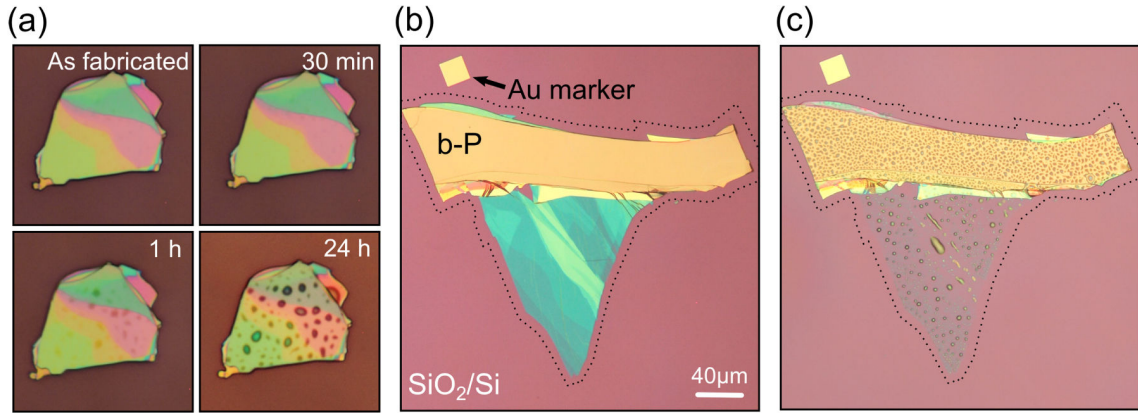


Figure 4.2: Aging of black phosphorus flakes. (a) Sequence of optical images acquired at different times after the transfer of the exfoliated black phosphorus flakes. The sequence shows how one hour after the transfer some droplet-like structures become visible on the surface of the flakes and how they keep growing when the samples are kept in air. (b) and (c) shows the comparison of a sample right after the transfer and after two weeks in air, respectively. [5]

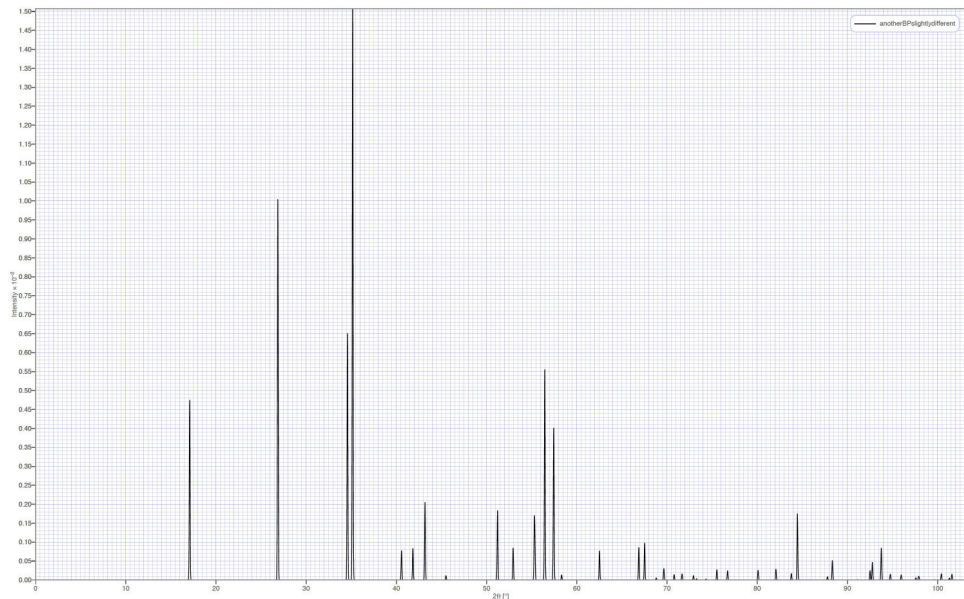


Figure 4.3: XRD simulated powder diffraction pattern from cif file via Reitveld refined experimental powder diffraction of BP [10]

Due to exfoliation being along the b (stacking) axis in BP, we expect that TEM will be looking down this axis (i.e. the stacking axis is the zone axis) at flakes. This can allow ease of identification when using HRTEM (when viewing atoms) or when performing electron diffraction as seen in figure 4.4 [7, 23, 28]. A report by Castellanos-Gomez [5] shows this diffraction pattern, along with some simulated data to characterise thickness. Note that the 101 reflections are forbidden, however due to the strong interaction of electrons with matter, multiple reflections occur on each layer of BP. This means that for odd numbers of layers these reflections are not cancelled out, and the 101 peaks can be seen (note a very tiny intensity may be seen for even numbers of layers).. They find that for odd numbers of layers disallowed peaks (101) are seen, and the intensity of these compared to the (200) allowed peaks gives an indication of thickness according to table 4.1. Note that this only works for extremely flat regions which are over vacuum. In addition to this, they notice "forbidden" reflections $h + l = 2n + 1$, for example (102). They suggest this could be due to a distortion of the lattice or the presence of adatoms on the surface of the BP.

Number of layers	$\frac{I(101)}{I(200)}$
1	2.557
2	0.001
3	0.286
4	0.001
5	0.104
6	0.001
21	0.009

Table 4.1: Thickness dependence of the electron diffraction patterns. We display the thickness dependence of the intensity ratio between the 101 and 200 reflections. The experimental data acquired on two spots of the thin flake and one spot of the thicker area has been included for comparison. [5]

In addition, some researchers utilise mass contrast using STEM to estimate the thickness, however this often relies on calibration with other techniques. Woomer et al. [95] also use the difference in counts through TEM, taking account for many factors such as exposure time, aperture selection, lens currents, magnification, and defocus value to study the change in count rate. From this they deduce the thickness, much like in optical transmission characterisation.

Note that experimenters have seen that BP is usually damaged somewhat by a 200kV beam, however a 300kV beam has been observed to damage flakes quickly, 80kV beams have been seen to not damage FL-BP ([7, 16]).

Lu et al studied the TEM patterns of BP in conjunction with Raman and electronic transport properties [52]. They first characterised the lattice directions using TEM, then confirmed with polarized angle dependent Raman spectroscopy the lattice directions, then later used this to confirm electronic transport measurements. Interestingly they found that the mobility, and conductance is higher along the ZZ direction than the AC direction, in contrast to other papers. They also found a different orientation from the Raman spectra. They found TEM lattice parameters to be

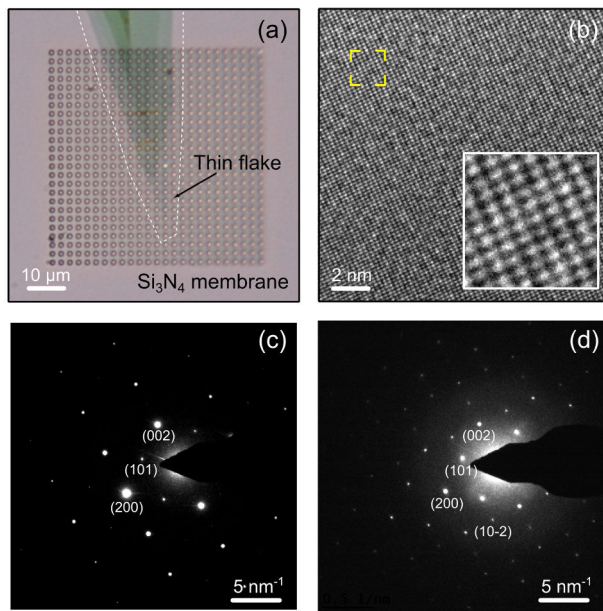


Figure 4.4: Transmission electron microscopy study of few-layer black phosphorus flakes. (a) Optical image of a black phosphorus flake transferred onto a holey silicon nitride membrane. (b) High resolution transmission electron microscopy image of the multilayered region of the flake (~13-21 layers). (c) and (d) are electron diffraction patterns acquired with a 400 μm spot on the thick (~13-21 layers) and the thin (~2 layers) region of the flake. [5]

$3.37 \pm 0.01 \text{ \AA}$ and $4.42 \pm 0.01 \text{ \AA}$ along the 100 and 001 directions respectively. Given the different results they obtained for other measurements, these results should be treated with caution.

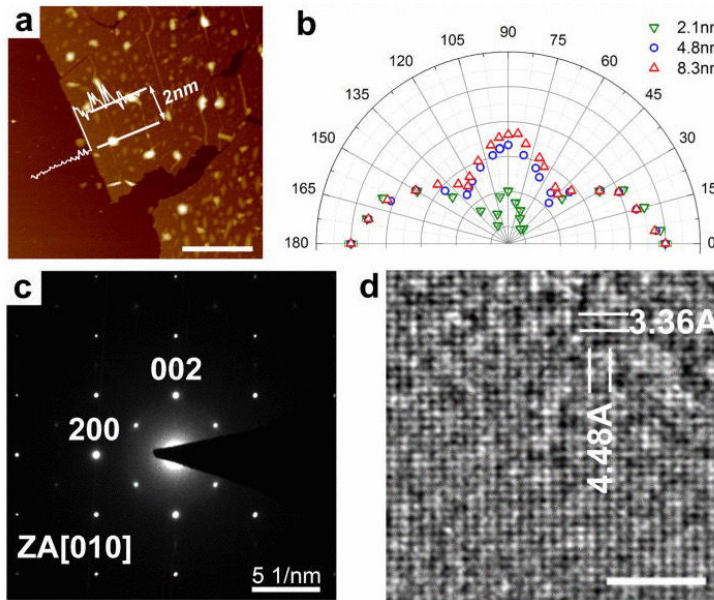


Figure 4.5: (a) An AFM image of a few-layer BP sheet with a height of 2.0 nm. (b) Polar plots of the angle-resolved normalized intensities of A_g^2 mode recorded on three typical flakes with different thicknesses. (c) and (d) The SAED and HRTEM images recorded on the tri-layer BP flake [52]

4.3 Electronic and Optical

4.3.1 PL

Coleman uses PL [24] to investigate the properties of nanosheets of BP in solution. PL of the solution (510nm source) revealed clear emission lines at 600nm and 900nm, with other weaker features at 1150nm, 1260nm and 1325nm. They associate these with PL from 1L to 5L of BP respectively. They fitted the spectrum to Gaussian (inhomogeneous broadening) peaks for 1 to 5 layer sheets, and compared to mechanical exfoliation literature, and saw good agreement with position and widths of components. They also calculated the PL quantum yield by dividing the peak area for each layer number by the volume fraction calculated via AFM. They find strong dependence on thickness for the quantum yield, due to the thickness dependent band structure.

Other work on mechanically exfoliated sheets revealed similar conclusions [60, 102, 108]. Zhang gets: 1.29, 0.98, 0.88, and 0.80 eV peaks for 2-5 layers. Yang gets: 1.75 ± 0.04 , 1.29 ± 0.03 , 0.97 ± 0.02 , 0.84 ± 0.02 , and 0.80 ± 0.02 eV for 1 to 5 layers respectively. Yang also finds optical exciton energy is 0.4eV.

Yang [102] used optical microscopy to find flakes thickness and then did PL normal way at -10C to reduce oxidation. They found the samples can survive more than fifteen hours under -10C and for several hours at room temp. They observed minor temperature shifts for PL peak energies. The peak energy in PL is the difference between the electronic band gap and the exciton binding energy, the 0.4eV they got was due to the substrate, they expect it to actually be 0.8eV.

The non-linear optical response of BP was utilized by Coleman et al. to mea-

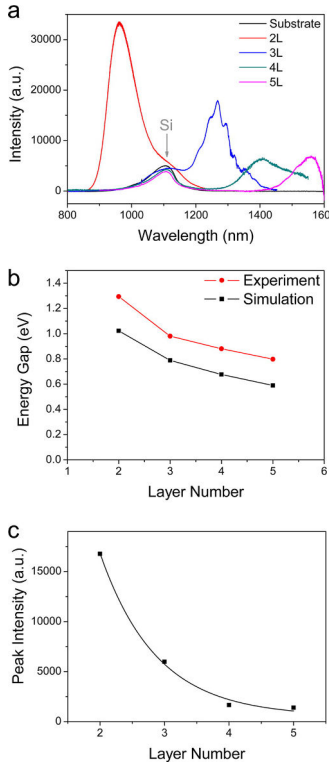


Figure 4.6: Photoluminescence (PL) spectra of thin-layer phosphorene. (a) PL spectra of 2L, 3L, 4L, and 5L phosphorene. (b) Energygap of 2L, 3L, 4L, and 5L phosphorene from experimental PL spectra and theoretical simulation. (c) Layer dependence of PL peak intensity that is normalized by layer number. [108]

sure the saturated absorber response of FL-BP [24]. They found The transmission increases with increasing laser intensity at both 1030nm and 515nm. Broadband saturable absorber response is useful, and potentially applicable to ultra-fast laser science. Graphene is known to have a similar broadband SA response, and when compared in the same experiment the FL-BP has much stronger SA response at both wavelengths [24, 85].

Zhang et al characterised the strong PL of BP flakes [108]. They noted that the PL intensity was much higher than that of the Si substrate, and suspect this is due to the direct bandgap in BP, compared to indirect in Si. They found a highly layer dependent spectra, measuring down to two layer flakes. They found PL energies of 1.29eV 0.98eV 0.88eV 0.8eV for two to five flakes in order. Quantum confinement is expected to be responsible for this, as has also been explained in DFT papers [46]. They speculate that increasing the number of layers increases the valleys in the band structure, which in turn shifts the DOS in the crystal. This will decreases relaxation time, especially for peaks and valleys of off- Γ points, leading to lower quantum efficiency due to the following equation for internal PL quantum efficiency estimate:

$$\eta_{PL} = \frac{k_{rad}}{k_{rad} + k_{defect} + k_{relax}} \quad (4.3.1)$$

Wang et al found that PL is strongly polarised along the AC direction [92]. This is suspected to be due to the lighter effective mass along this direction. This leads to an extended electronic wave-function along the AC direction, thus the carriers are more mobile along this direction as it is dispersive, than the flat ZZ band. So the isotropic coulomb interaction binds the carriers most strongly in the y direction and this gives rise to anisotropic polarization in emission.

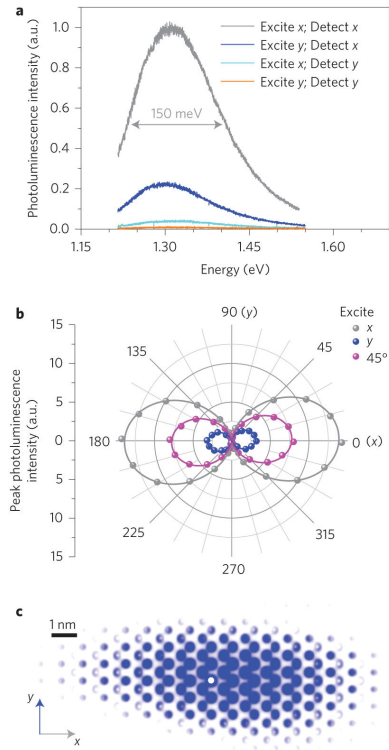


Figure 4.7: Exciton photoluminescence with large in-plane anisotropy. a, Polarization-resolved photoluminescence spectra. The excitation 532 nm laser is linearly polarized along either x (grey curves) or y (blue curves) directions.. b, Photoluminescence peak intensity as a function of polarization detection angle for excitation laser polarized along x (grey), 45° (magenta) and y (blue) directions. Solid lines are fitted curves using a $\cos 2\theta$ function (θ denotes the angle between the x axis and the polarization detection angle). c, Top view of the square of the electron wavefunction of the ground-state exciton in monolayer black phosphorus. Because the carriers are more mobile along the x direction with low effective mass and the Coulomb interaction is isotropic, the exciton is anisotropic, forming striped patterns as shown. The white spot at the centre represents the hole. Scale bar, 1 nm. [92]

No matter the polarization, the PL peaks at 1.3eV with a FWHM of 150meV [92]. They also find PL is most intense with a 2.2eV excitation, which suggests a quasi-particle band edge. This matches calculations.

In summary they found an optical band gap of 1.3 ± 0.02 eV and a quasi-particle bandgap of 2.2 ± 0.12 eV.

4.3.1.1 Extinction coefficients

Coleman et al. [24] use extinction coefficients to estimate the concentration of few layer BP in their solutions. The extinction coefficient is defined as:

$$T = 10^{-\epsilon Cl} \quad (4.3.2)$$

Where l is the cell length, C is the nanosheet concentration, T is the optical transmittance and ϵ is the extinction coefficient. This includes contributions from the absorbance and the scattering. The scattering is size dependent, therefore the extinction coefficient does not give an accurate estimate of nanosheet concentration. The absorbance coefficient can however be used for concentrations of material in solution.

4.4 Phononic

4.4.1 Black Phosphorus

Sugai investigated the Raman modes of BP in 1985. Nothing new from their paper but use as a reference [81].

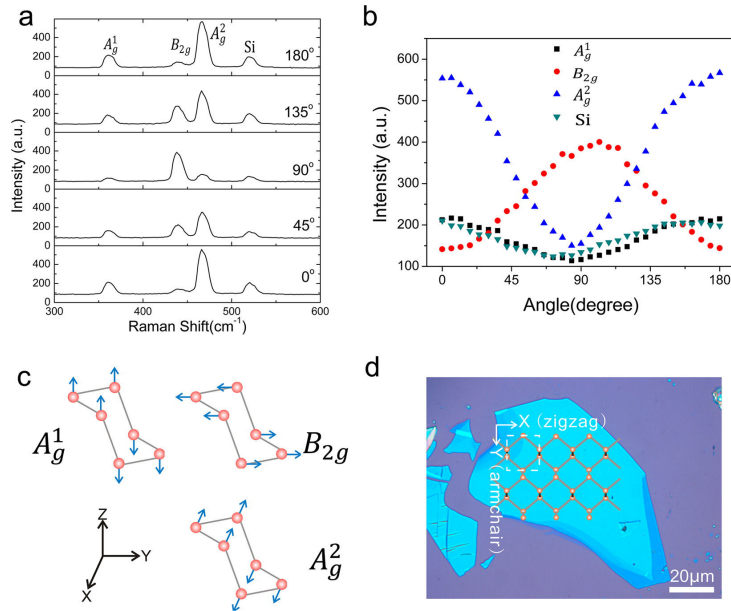


Figure 4.8: Phosphorene crystalline orientation determination by polarization Raman spectra. (a) Raman spectra of a 15L phosphorene under different polarization angles. (b) Polarization dependence of A_g^1 , B_{2g} , and A_g^2 modes in a 15L phosphorene and the Raman peaks in silicon. (c) Schematic plot showing the vibration directions of A_g^1 , B_{2g} , and A_g^2 Raman modes. (d) Crystalline orientation of the 15L phosphorene flake, determined by angle-dependent Raman measurement. [108]

Note about the notation: A and B represent the degeneracy, whilst g and u represent if it is odd/even. ie transform through centre of symmetry and if the mode changes then it is odd. Only odd modes are Raman active (REF EXPAND AND MOVE TO TECHNIQUES SUMMARY).

Many researchers have now investigated the angular dependence of the Raman response in BP(REF), as described in section 2.5.1. This allows rapid determination of the orientation of a flake of BP found using optical microscopy or otherwise, simply by investigating the angular response of the Raman spectra, and fitting it to the relevant equations which have been presented.

Zhang et al. also looked at the angle dependent Raman response of BP [108]. They noted the same results as above, however offered no detailed quantitative explanation. They did note that the peaks in intensity make sense due to the geometries of the Raman modes. ie A_g^2 mode will peak when B_{2g} mode hits minima if light is polarized along x direction.

They also studied the temperature dependence of BP, and noted that thin flakes are more temperature sensitive than either graphene or MoS_2 [93]. They see a linear relationship of :

$$\omega = \omega_0 + \chi T \quad (4.4.1)$$

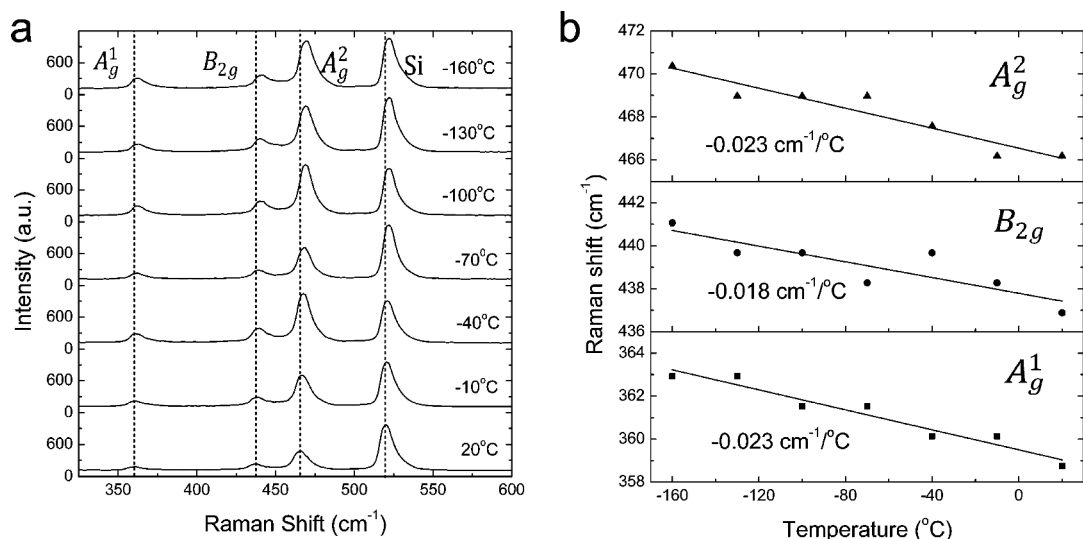


Figure 4.9: Low-temperature Raman spectra of 5L phosphorene. (a) Raman spectra of a 5L phosphorene at temperatures ranging from 20 to $-160\text{ }^{\circ}\text{C}$. (b) Temperature dependence of A_g^1 , B_{2g} , and A_g^2 Raman peak positions. [108]

Chapter 5

Applications

Flexible coated transistors were produced by Zhu et al. which could withstand 5000 bending cycles [111].

Liquid-phase exfoliation using the Coleman method by Sun et al. showed that clean cut edges are present on exfoliated phosphorene along the ZZ long axis [82]. They see nano-belt objects, which are wide but have ribbon like aspect ratios.

They confirmed thickness using TEM and Raman, seeing the characteristic A_g^2 shift due to stiffening, and a change in ratio of A_g^2 to A_g^1 or B_{2g} for decreasing thickness. They used liquid phase exfoliated BP and graphene to produce hybrid materials by mixing these solutions. XPS confirmed that P 2p and C 1s orbitals were unchanged and therefore the layers did not chemically alter each other.

This experiment focused on sodiation of phosphorene structures, and whilst they did manage to intercalate few layer BP, they used binders in an electrochemical set-up so were not able to liquid-exfoliate the intercalated material.

Hembram et al. used DFT to study the sodiation mechanisms in BP [25]. BP is of particular interest for sodium ion batteries (NIBs), as graphite does not allow intercalation of sodium [63]. Also BP is expected to have very high capacity and

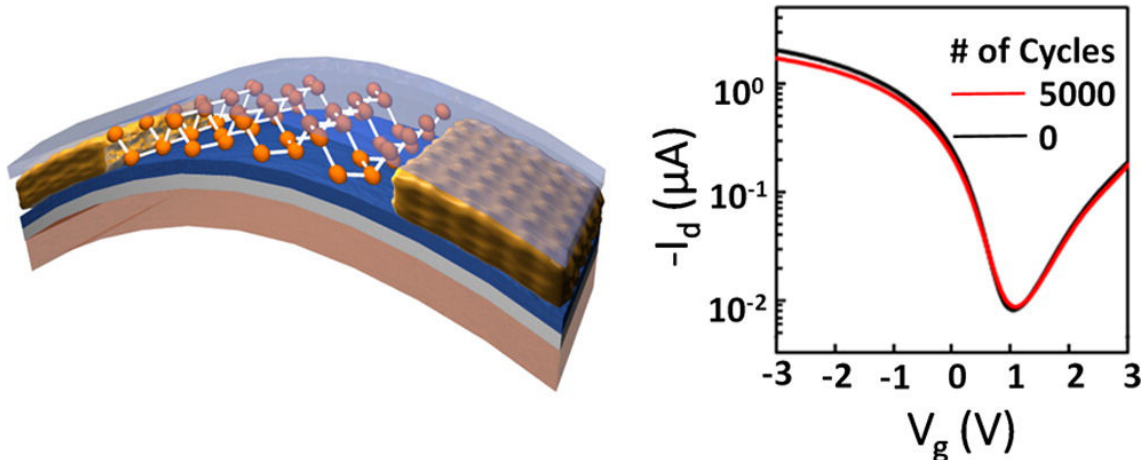


Figure 5.1: [111]

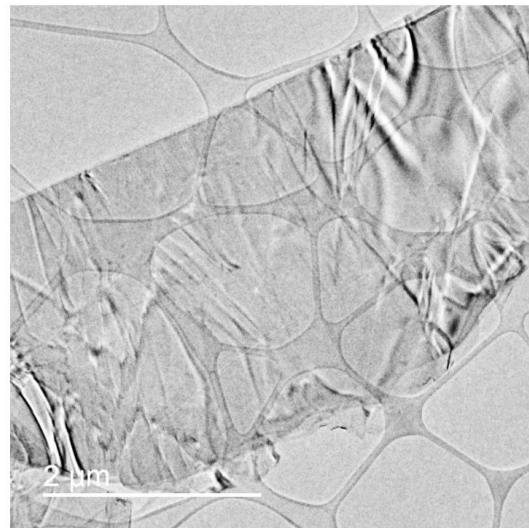


Figure 5.2: TEM image of phosphorene nanobelt. [82]

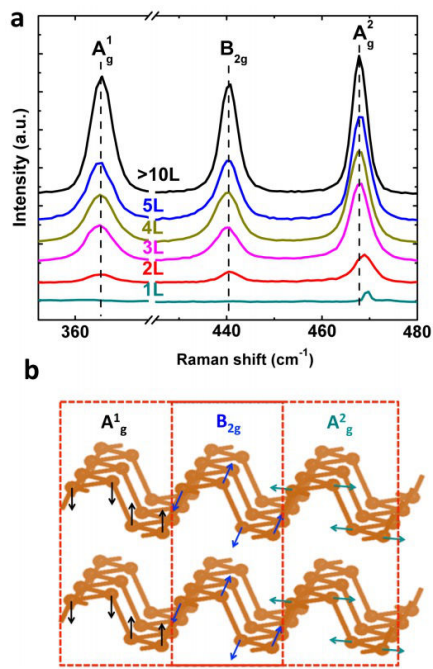


Figure 5.3: Raman of mono-layer and few-layer phosphorene. a, Raman spectra of phosphorene with different number of layers. b, Atomic displacements of Raman active modes. [82]

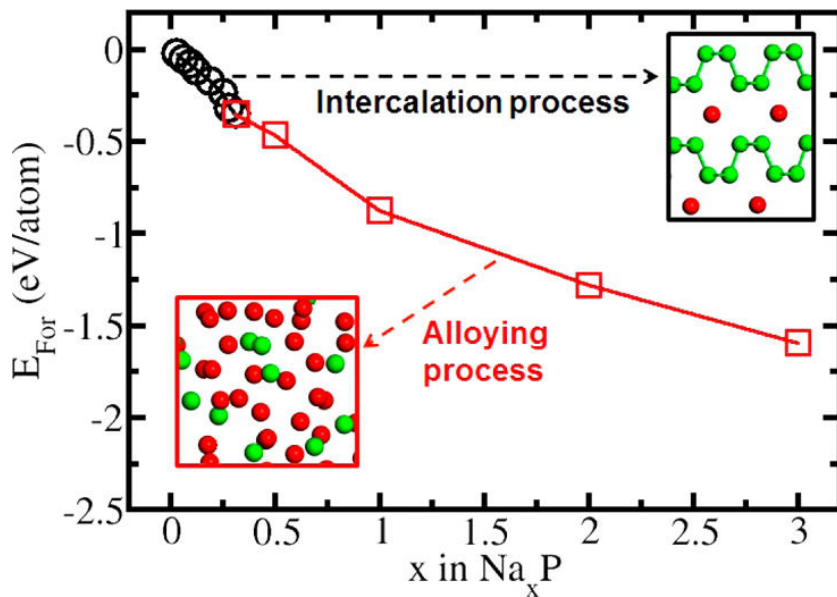


Figure 5.4: [25]

mobilities greater than other allotropes of P. P and Na are also much more environmentally friendly than lithium ion batteries in current use.

The key finding of their study were that Na atoms prefer to intercalate into BP up to $\text{Na}_{0.25}\text{P}$, where they first preferentially intercalate into the same layer, then once covering 25% of each phosphorene layer they intercalate into other layers. This causes an interlayer expansion of 2.26\AA to 6.84\AA . In plane bonds show little change, neither do staggered bonds.

YOUR SAMPLE XRD LI TRIPLE!!!

They found that intercalation above this ratio leads to alloying of BP. The Na breaks p-p bonds, preferentially the staggered bonds. These bonds are longer and require less energy to break. Additionally, in intercalated BP, increasing the interlayer distance leads to lower steric hindrance in the stacking axis, and also phosphorene layers begin to slide over each other generating lateral stress in the staggered bonds. This means that intercalated BP is easier to break p-p staggered bonds than in pristine.

When these bonds break, they see charge transfer from the Na atoms to the p-p dumbbells which are formed. Additionally they see symmetric charge accumulation on the p-p bonds in BP which are unbroken nearby.

They also studied the diffusion mechanism of Na in BP, and found the following diffusion barriers: 0.18eV, 0.76eV and 4.2eV for Na diffusion along the zz direction (ie in the channels), along the Ac direction and along the stacking direction through a p-hexagon respectively. This shows that there is relatively easy diffusion for Na atoms in BP along the channels. They note that a challenge for BP as a sodium anode material would be that it could exfoliate. This could be overcome by forming

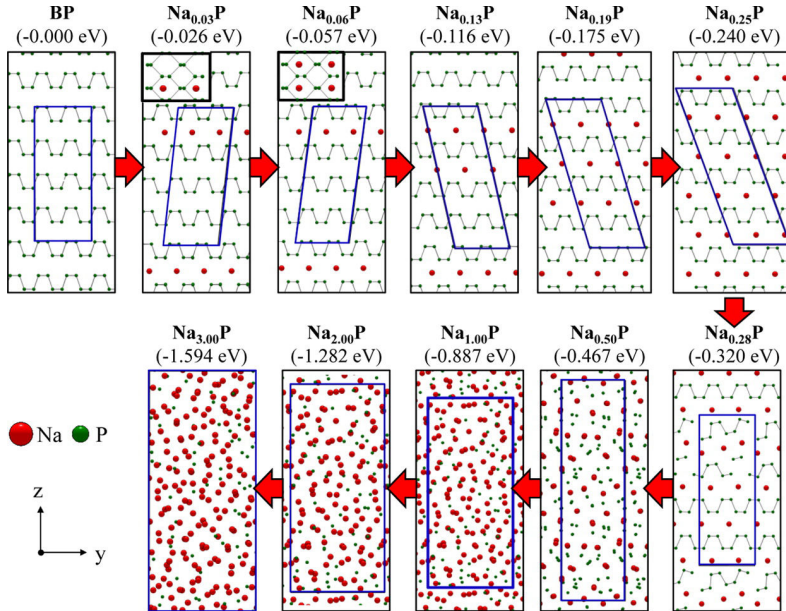


Figure 5.5: A sodiation mechanism of black phosphorus. Here, the numbers in parentheses indicate calculated formation energies of Na_xP structures. The blue solid lines indicate cell sizes of Na_xP including 64 P atoms used in our DFT calculations, and the black insets in $\text{Na}_{0.03}\text{P}$ and $\text{Na}_{0.06}\text{P}$ structures show top views of each structure to clarify positions of Na atoms in the structures. [25]

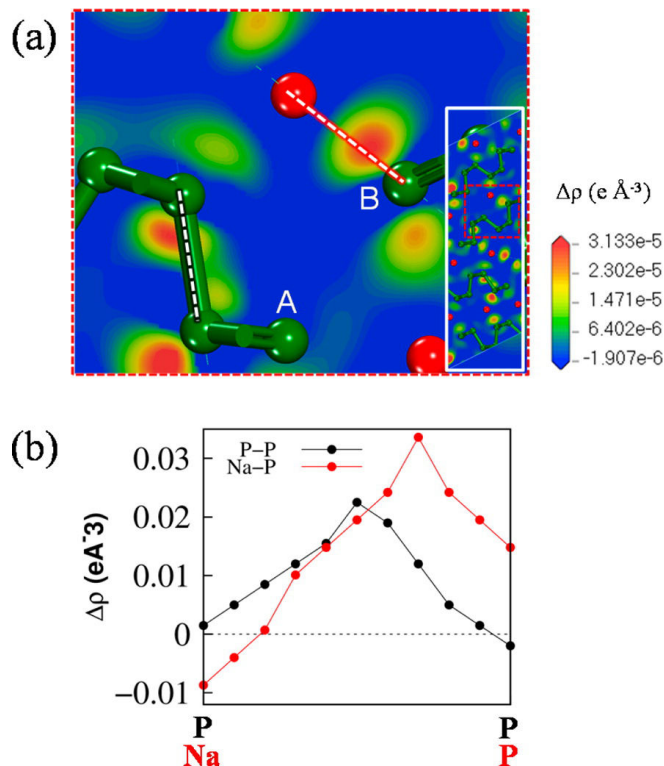


Figure 5.6: (a) Valence electron charge density distribution on a (010) plane in the $\text{Na}_{0.28}\text{P}$. Here green and red atoms are P and Na atoms, respectively. (b) The charge density difference distribution along a P-P bond represented by a black dashed line in (a) and the Na-P bond represented by a red dashed line in (a). [25]

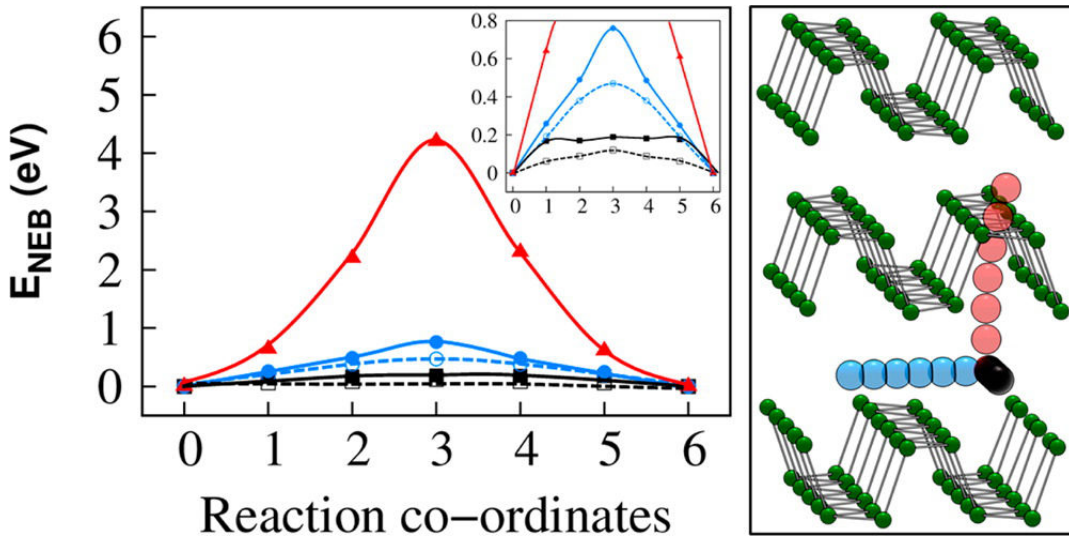


Figure 5.7: NEB calculations on diffusion barriers of a Na atom in black phosphorus (solid symbols) and on a phosphorene single layer (open symbols). The color codes correspond to the diffusion pathways in the right figure [25]

stabilising p-c bonds by using graphene, or forming pillared structures.

Sodium ion-batteries are a potential application of bulk and few layer BP. Sun et al. showed that sodium ion batteries could be produced with good cyclability and mobilities by using phosphorene and graphene [82, 84, 101]. Sodium is much better for the environment, hence why this is interesting. The sandwich structure of graphene and phosphorene provides elasticity which accommodates the volume expansion upon sodiation of BP, and BP allows short diffusion lengths for sodium, whilst graphene provides good electrical conductance.

They saw sodiation via shifting of b-axis peaks in XRD, followed by alloying of BP as described in the theoretical paper by Hembram [25] 3.2

Ling and Ang investigated the effect of thermal annealing on phosphorene via Raman spectroscopy [44]. They noted that Hafnium dioxide (HfO_2) is often used as a high-k dielectric gate material for CMOs transistors. A thermal annealing stage is usually required in this production, and so studying the effect of thermal annealing with this dielectric is valuable for future applications. They see an unexpected blue shift with increasing temperature (in contrast to previous work suggesting a red shift as expected). This is attributed to diffusion of HfO_2 into the phosphorene film. The film was also passivated with SiO_2 which would have prevented thermal expansion and red shift. The diffusion of larger atoms from the dielectric into phosphorene would cause a blue shift due to compressive strain. At about 400C they see a red shift, which they attribute to plastic relaxation of the film, which is also accompanied by a broadening of the FWHM which also supports a loss of crystallinity.

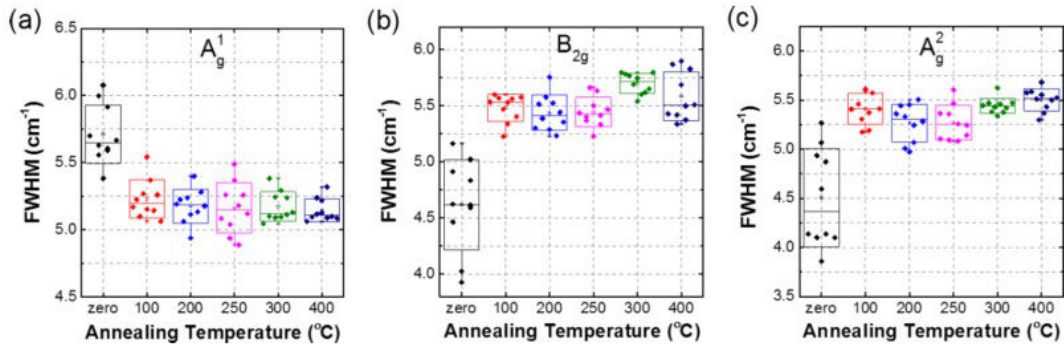


Figure 5.8: Temperature dependence of the full-width at half maximum (FWHM) of the Raman phonons corresponding to the (a) out-of-plane (A_g^1) vibrational mode and (b) and (c) in-plane (B_{2g} and A_g^2) vibrational modes. A1g [44]

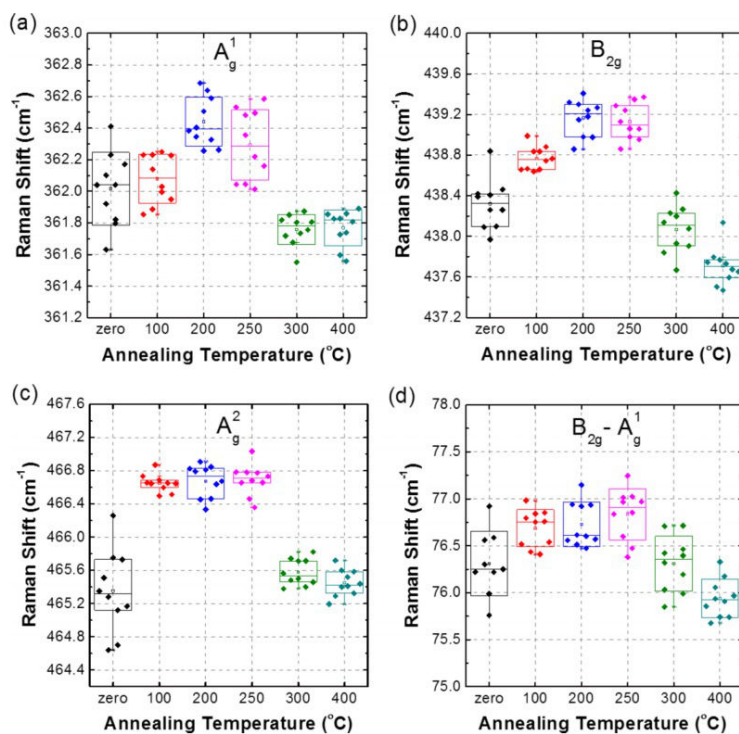


Figure 5.9: Temperature dependence of the Raman shifts corresponding to the (a) out-of-plane (A_g^1) and (b) and (c) in-plane (B_{2g} and A_g^2) vibrational modes. (d) The delta Raman shift between the B_{2g} and the A_g^1 optical modes. [44]

Chapter 6

Phosphorene Nanoribbons

Black phosphorus nanoribbons have only been experimentally isolated via two methods. One production of the ribbons were actually macroscopic and too large to have the quantum confinement effects associated with the predicted unique characteristics. The second production described a method of making them, and confirmed they were structurally intact with TEM, although they were unable to measure any of the interesting properties yet. For this reason the many characteristic of BP nanoribbons are based on theory only.

Here we discuss the methods of production, the properties, a brief overview of the characterisation techniques utilised and a discussion of specific applications of these ribbons.

6.1 Isolation

Lee et al. produced phosphorene nanoribbons via a top-down procedure [39]. They first mechanically exfoliated BP layers, and then used electron beam lithography (ELB) to cut them to dimensions. They then connected contacts via further ELB and ion milling to measure the thermal and electrical transport properties. They only achieved nanoribbons of 50nm thickness, due to difficulty in using a micro-manipulator in order to perform measurements. Furthermore, the ELB method was not precise enough to manufacture very thin ribbons, so the widths of the ribbons were of the order of over 500nm.

Das et al. utilized STEM beams in order to produce a 'lattice' of nanoribbons [57]. They first drill two holes in a BP flake using an STEM, then use the STEM to etch away the area between them until a narrow region is left. This region can be controlled as AC or ZZ and ribbons on the nm scale are formed, with edge roughness of the order of 1-2nm. These nanoribbons had widths of order 5nm and lengths of order 5-10nm (until joining onto the larger lattice). No measurements on their properties were carried out, and it is unclear if they will behave as previously predicted. They also perform DFT to explain pore expansion within the flake once a hole is drilled, which expands preferentially along the AC direction.

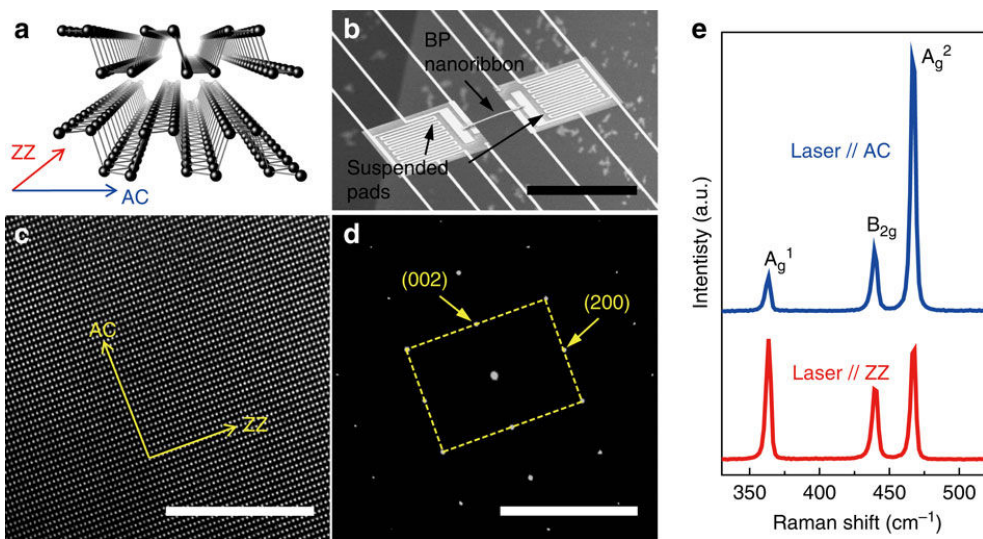


Figure 6.1: Crystal structure of BP and device structure for the thermal transport experiment. (a) Illustration of the crystal structure of BP showing the ZZ and AC axes. ZZ and AC axes correspond to the [100] and [001] direction of the orthorhombic unit cell, respectively. (b) Scanning electron microscopic image of a micro-device consisting of two suspended pads and a bridging BP nanoribbon. Thermal conductivity is measured by transporting heat from the Joule-heated pad to the other pad through the nanoribbon. (c) High-resolution transmission electron microscopy lattice image of a BP flake. (d) Selected area electron diffraction pattern taken from the area shown in c.(e) Micro-Raman spectra of a BP flake with laser polarized in parallel to the ZZ and AC axis, respectively. Scale bars, 50mm(b); 10nm (c); 20nm-1 (d). [39]

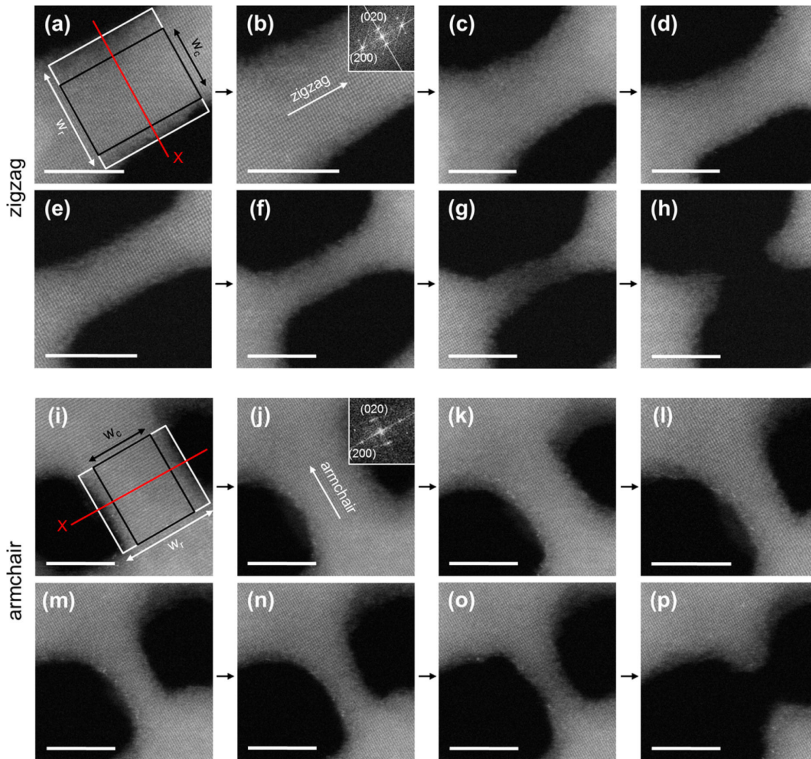


Figure 6.2: STEM nanosculpting of zigzag and armchair few-layer BPNRs. HAADF STEM images of an (a-h) 8.0 nm long zigzag and (i-p) 6.5 nm long armchair nanoribbon. (a,i) wr and wc are the total and crystalline BPNR widths, respectively (see also Figure S6.1). Thinning of the ribbons from (a) to (h) and from (i) to (p) was observed by using the HAADF intensity-thickness correlation for each panel along the red line X (indicated in (a) and (i); see also Figure S11). The fast Fourier transforms in the insets of (b) and (j) indicate lattice spacings of 1.65 and 2.28 Å, consistent with a_1' and a_2' , respectively. For the zigzag case, wr is initially (a) 7.2 nm and subsequently narrowed to (b) 6.0, (c) 5.7, (d) 4.6, (e) 2.8, (f) 2.2, and (g) 1.7 nm. The corresponding wc values are (a) 5.6, (b) 4.6, (c) 4.3, (d) 3.1, (e) 1.9, (f) 1.0, and (g) 0 nm. For the armchair case, the values for wr are (i) 6.3, (j) 5.8, (k) 4.2, (l) 3.1, (m) 2.8, (n) 2.5, and (o) 2.1 nm. The corresponding wc values are (i) 4.9, (j) 4.2, (k) 3.0, (l) 1.4, (m) 0.9, (n) 0.5, and (o) 0 nm. After the BPNRs break, (h) 3.5 and (p) 2.8 nm wide nanogaps remain. All scale bars in (a-p) are 5 nm. [57]

6.2 Properties

Here the properties of BP nanoribbons (BPNRs) are discussed, focusing on the physical, electronic and optical and phononic and thermal properties.

6.2.1 Physical and stability

6.2.2 Electronic and optical

NEW

The [32] paper acute mechano electoronic responses in twisted nanoribbons is a really good paper with good images for twist angle vs band gap. Also the [49] paper on 2d semiconductor wiht inactive defects has good ribbons stuff!

ENDNEW

Ma et al. have investigated the electronic nature of the edge bands in ZZ phosphorene nanoribbons [55]. They find that when a bias is applied between the top and bottom layers of a ZPNR that the edge bands split, this reduces the linear conductance to zero, which could potentially be applicable to FETs. The Seebeck coefficient is also greatly enhanced with this bias. They find that ribbon width has no effect on this behaviour of the edge bands.

They also find that applying a boundary voltage to one layer merges only one of the bands with the bulk. Applying to both merges both, which opens an energy gap in the bulk. This also has the effect of significantly enhancing S.

Nourbakhsh and Asgari investigated the properties of narrow PNRs and their potential applications [62]. They studied H passivated PNRs mostly, as they are predicted to be much more stable. They find that for both ribbon types the band gap decreases with increasing ribbon width. They find that the significant changes in the ribbon properties occur for widths below 3nm.

They find that the quantum confinement effect in ZPNRs is stronger due to the larger bandgap. This is due to APNRs having the conduction band minima (CBM) and valence band maxima (VBM) in the middle of the ribbon, so they 'see' less of the edge states than ZPNRs.

The band gap is very flat for ZPNRs and linear for APNRs. This suggests that ZPNRs behave as classical massive particles, whilst APNRs obey the Dirac equation and are therefore Dirac massless fermions.

They do find that for pristine ribbons, ZPNRs are metallic for all widths and APNRs are indirect semiconductors.

For a hetero-junction of APNR and ZPNR the lowest energy positions for electron and hole are on different ribbons, good for PV!

They also investigated the exciton fine structure (i.e. splitting) and found it is very large PNRs, and largest for narrow ZPNRs. This singlet-triplet splitting

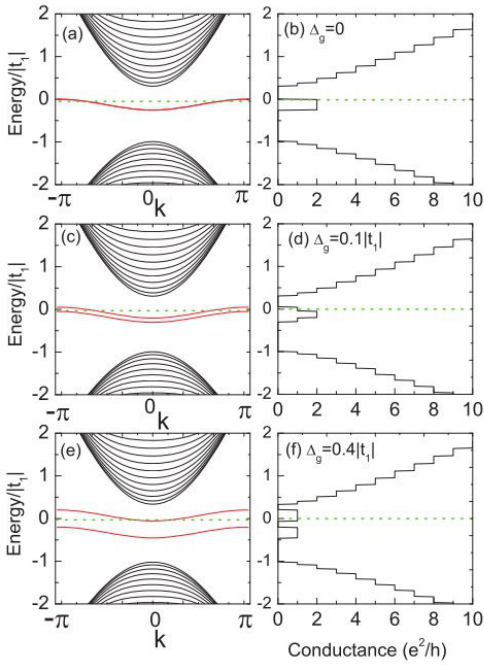


Figure 6.3: Calculated band structure and conductance of the ZPNRs in the presence of an applied bias voltage Δg at zero temperature. (a)-(b) $\Delta g = 0$, (c)-(d) $\Delta g = 0.1 - t_1$, and (e)-(f) $\Delta g = 0.4 - t_1$. Red curves represent the quasi-flat bands, and green lines are the Fermi energy. The width of the ZPNRs is set to $N = 20$. [55]

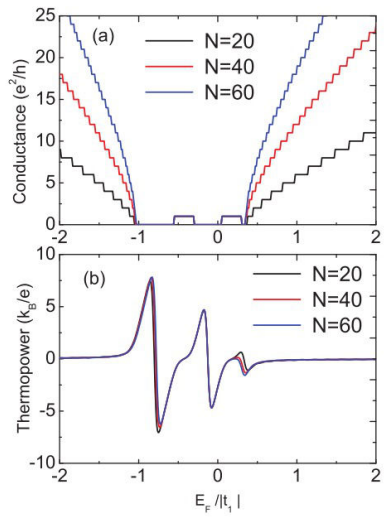


Figure 6.4: Calculated conductance and thermopower of the ZPNRs under bias voltage $\Delta g = 0.6 - t_1$ for three different ribbon widths. The temperature is taken to be $k_B T = 0.03 - t_1$ in the thermopower calculation. [55]

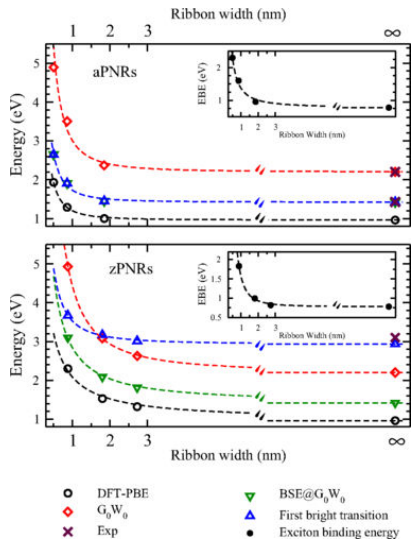


Figure 6.5: The evolution of the band gaps (PBE, G0W0), optical gap (BSE@G0W0) and first bright excitonic state as a function of the nanoribbon width. The insets show the variations of the exciton binding energy (EBE) with the ribbon width. The power law fitting curves are presented by dashed lines. Experimental data of 2D phosphorene are marked by the cross sign [7, 27]. [62]

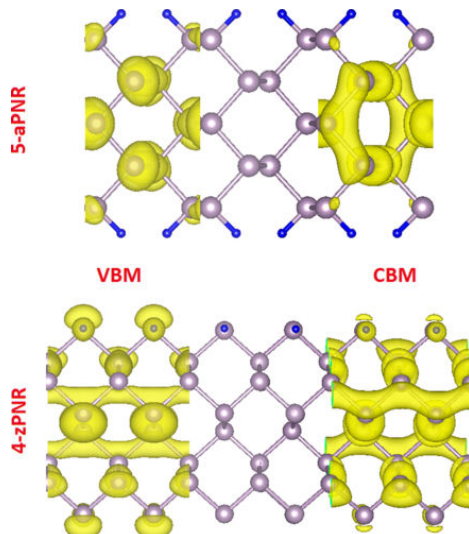


Figure 6.6: Top view of electron charge density of the VBM and CBM states of the 5-aPNR and 4-zPNR. [62]

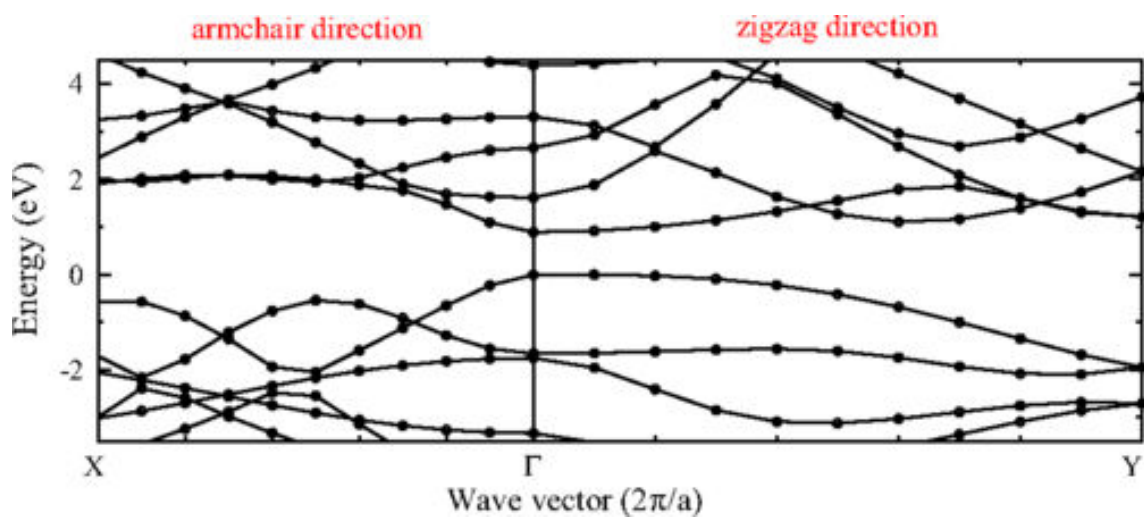


Figure 6.7: Electronic band structure of 2D phosphorene, calculated by DFT-PBE along the ac and zz directions. The top of the valence band is set to be zero. [62]

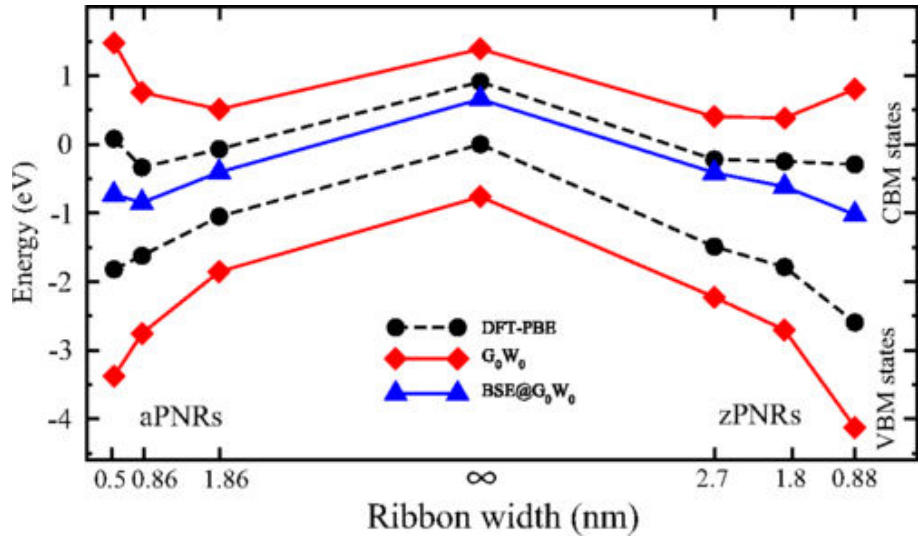


Figure 6.8: The calculated VBM and CBM states of PNRs and 2D phosphorene as a function of their width. [62]

is larger than for systems such as carbon nanotubes, graphyne and doped silicon nanowires which are usually considered impressive [27, 62, 64, 67]. This has potential applications in PV, biomedical, photo-luminescence and quantum information.

They also note that due to the flat band structure in ZPNRs, optical transitions are forbidden near the gamma point. This is because in optical transitions the dipole selection rules ensure that for a one photon transition $\Delta L = \pm 1$ and the parity must be even overall. Since the parity of momentum is odd, the conduction and valence bands must have opposite parity in the direction of light polarization, and the same in all other directions.

In the paper they quote the allowed transitions, which are derived from the condition of the same or different parities for light polarized along the zigzag direction. These are:

$$p_y \leftrightarrow (S, d_{x^2-y^2}, d_{z^2}) \quad (6.2.1)$$

$$p_x \leftrightarrow d_{xy} \quad (6.2.2)$$

$$p_z \leftrightarrow d_{zy} \quad (6.2.3)$$

The states for p_y correspond to ($l=0 m=0$, $l=1 m=\pm 1$, $l=1 m=0$). Therefore, given that the following:

$$L = rxp = -i\hbar(rx\nabla) \quad (6.2.4)$$

and:

$$L_z = xp_y - yp_x \quad (6.2.5)$$

$$L_z = i\hbar p_y \frac{\partial}{\partial p_x} - i\hbar p_x \frac{\partial}{\partial p_y} \quad (6.2.6)$$

for states around Γ , i.e. $p_y=0$, then:

$$L_z = -i\hbar p_x \frac{\partial}{\partial p_y} \quad (6.2.7)$$

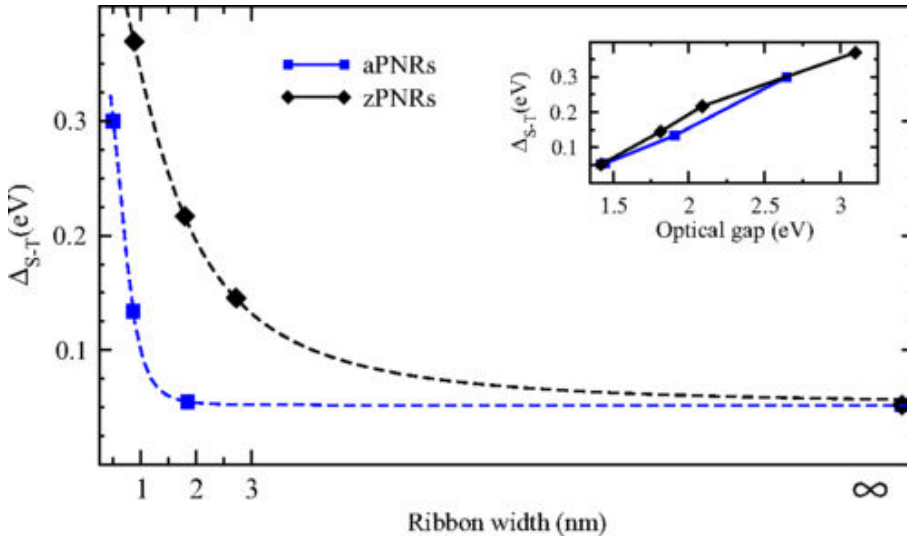


Figure 6.9: Exciton exchange splitting versus ribbon width. In the inset, the exchange splitting as a function of the band gap of PNRs. [62]

Since the bands are flat, we can say that:

$$\frac{\partial E}{\partial p_y} = 0 \quad (6.2.8)$$

Therefore $L_z E=0$ for both the initial and final states. Therefore this means that there is no $\Delta L=\pm 1$ required for a dipole allowed transition near the Γ point and so the transition is not dipole allowed.

Note the assumption in this derivation is that $L_z E$ is a relevant quantity, which is based on the assumption that $L_z \psi$ is equal to $L_z E$. This is valid if we use the time independent Schrödinger equation.

Poljak and Suligoj investigated the immunity of electronic and transport properties of phosphorene nanoribbons to edge defects [69]. They highlight the need for new materials which can aid the MOSFET community in continued development. This is a search for thin and short materials for channels in FETs. 2D materials allow thin channels with control over the whole channel and increased immunity to short channel effects. Digital electronics demand a bandgap, however RF electronics do not. Both applications do require high carrier mobilities, especially RF electronics.

They note that for increasing the defects in PNRs, the DOS near the Fermi level increases due to edge states for both configurations of ribbon, and more Van Hove singularities away from the bandgap too. Also the variability from device to device increases with increasing defect density.

They find that ideal ZNPRs have no density of states at 0eV, which is due to the flat band associated with the edges. A DOS change in both PNRs could lead to increased transmission in the off state. This is highly undesirable for digital electronics.

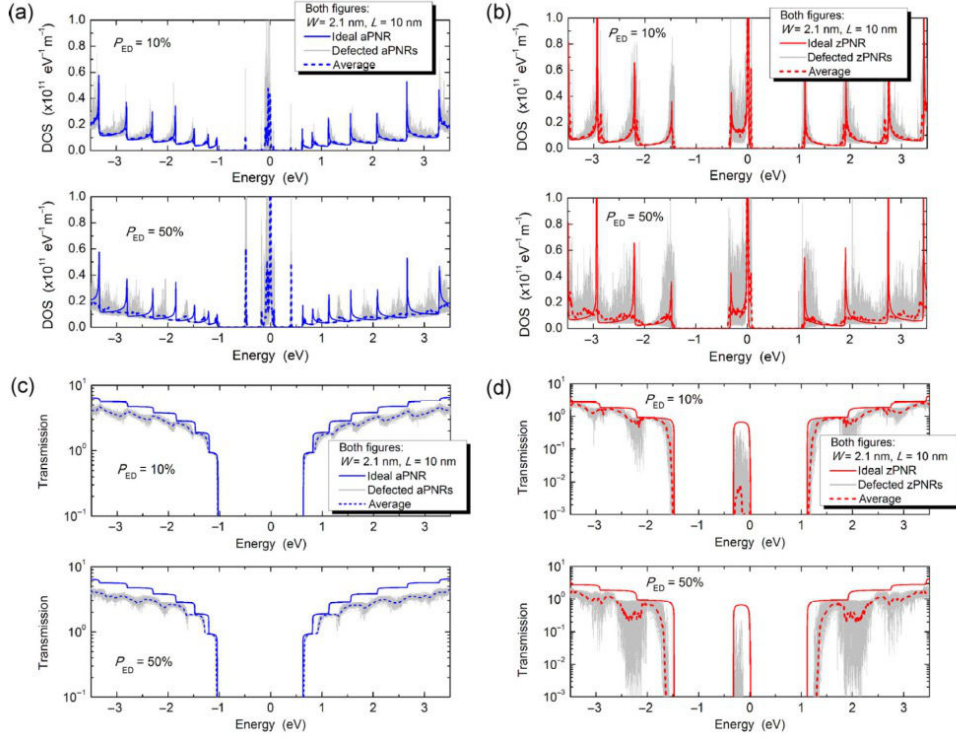


Figure 6.10: Impact of edge defects on DOS and transmission in PNRs. The impact of edge defects is reported for (a) DOS and (c) transmission in aPNRs, and (b) DOS and (d) transmission in zPNRs. The results are shown for $W = 2.1 \text{ nm}$, $L = 10 \text{ nm}$, and a PED of 10% and 50%. Each panel contains results for all ($N = 50$) simulated PNRs with defects (gray line), average DOS or transmission (dashed red/blue line), and DOS or transmission for an ideal PNR (full red/blue line). [69]

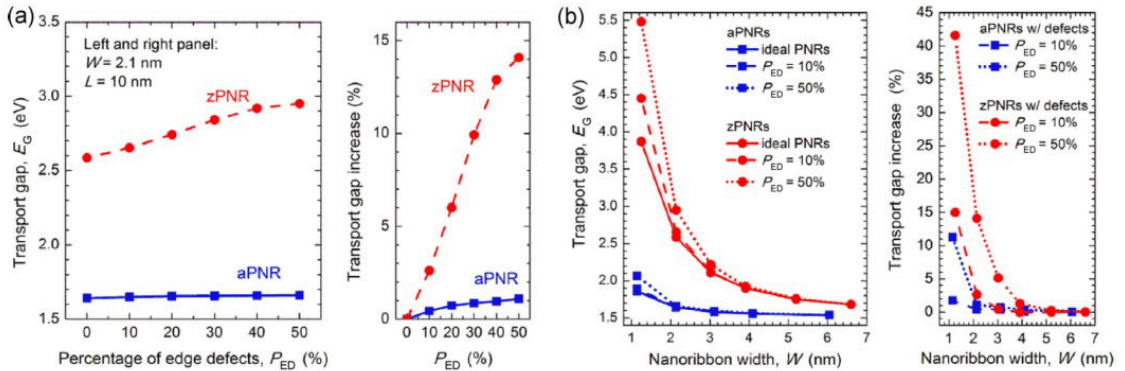


Figure 6.11: Transport gap modulation by PED and PNR width. (a) Left panel: impact of increasing PED on E_G . Right panel: increase of E_G as a function of PED. Results are shown for aPNRs and zPNRs about 2-nm wide and 10-nm long. (b) Left panel: width-dependence of E_G in aPNRs and zPNRs with 10% and 50% edge defects. Right panel: increase of E_G in aPNRs and zPNRs with defects as a function of nanoribbon width. Each data point, except for an ideal device ($PED = 0$), gives an average parameter value obtained by simulating $N = 50$ PNRs with random edge defects. Ideal zPNRs are metallic due to the non-zero transmission around $E = 0 \text{ eV}$, but E_G is nevertheless extracted as the separation between the main valence and conduction bands to allow a comparison with zPNRs with defects that are semiconducting. [69]

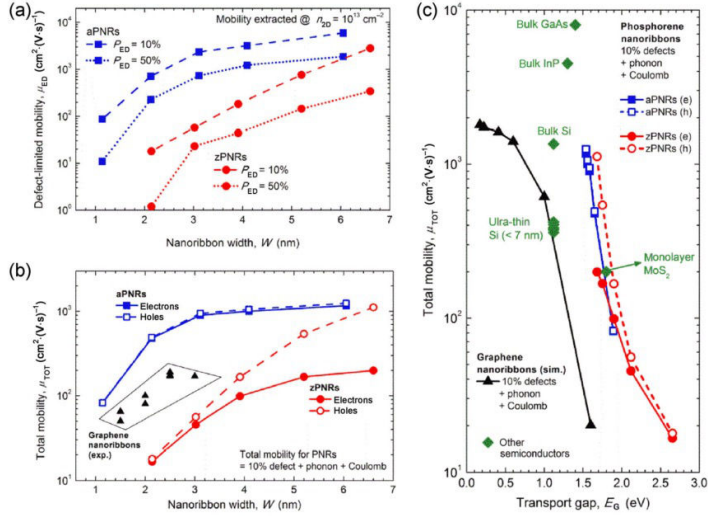


Figure 6.12: Electron and hole transport properties in PNRs with edge defects. (a) Defect-limited mobility as a function of the nanoribbon width in aPNRs and zPNRs with a PED of 10% and 50%. The μ_{ED} is extracted at $n2D = 1013 \text{ cm}^{-2}$, i.e. the typical on state. (b) Total mobility in PNRs compared to experimental mobility in GNRs. The μ_{TOT} for PNRs is obtained by applying Matthiessen's rule to μ_{ED} (reported in this work for PED = 10%), μ_{PH} and μ_{CO} (see the main text for details). (c) Mobility-transport gap plot for electron and hole mobility in aPNRs and zPNRs. The plot also shows the simulation results for GNRs, and experimental data bulk Si, InP, and GaAs, as well as monolayer MoS₂, and UTB SOI with a thickness of less than 7 nm. [69]

They note that the size of the bandgap in APNRs is immune to the density of edge defects, and that localised edge states inside the bandgap do not contribute to the mobility.

For ZPNRs, there is unitary transmission around $E=0\text{eV}$. This therefore makes ZPNRs metallic and so undesirable for digital applications. A gap is however opened at 10% defect density, which is due to a degraded contribution of edges to flat band, which is a similar effect to that reported with H passivation.

ZPNRs are more sensitive to defects than APNRs, with a higher variability in transmission and increasing bandgap. This anisotropy in defect sensitivity is in sharp contrast to GNRs.

They note that increasing the defect density from 10% to 50% in APNRs changes the bandgap of 1.64eV by only 1%, however for ZPNRs this changes from 2.59eV to 2.96eV . There is also a very large variability in bandgap size for each defect density for ZPNRs, much smaller for APNRs.

Quantum confinement along the width gives the opportunity to further tune the bandgap, with a maximum of 1.86eV at 4nm for APNRs and 3.87eV at 7nm for ZPNRs.

The density of defects also hugely influences ZPNR bandgap, however it doesn't have a large effect on APNRs. However both types are much more immune to de-

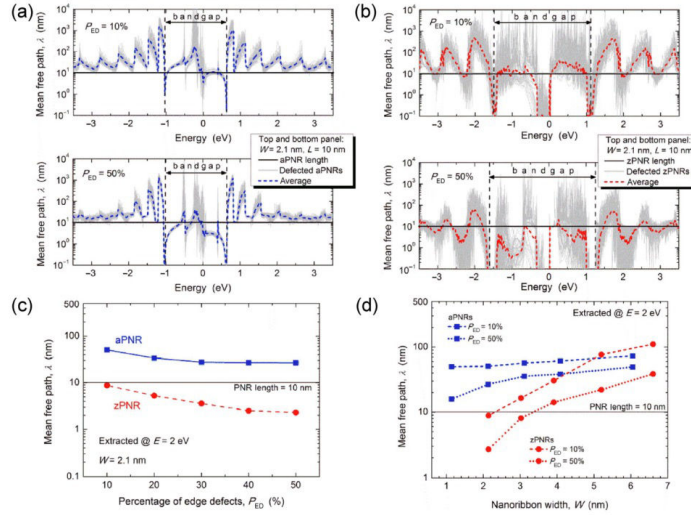


Figure 6.13: Influence of edge defects and nanoribbon width downscaling on mean free path. λ as a function of energy for a PED of 10% and 50% is reported for (a) aPNRs and (b) zPNRs around 2-nm wide. Each panel in (a) and (b) contains the λ results for all ($N = 50$) simulated PNRs with defects (gray line) and average λ (dashed red/blue line). (c) Impact of increasing PED on λ extracted at 2 eV in aPNRs and zPNRs around 2-nm wide. (d) Width-dependence of λ in aPNRs and zPNRs with 10% and 50% edge defects. Each data point in (c) and (d) is an average λ obtained by simulating $N = 50$ PNRs with random edge defects. [69]

fects than GNRs.

They also investigated the mean free path:

$$\lambda(E) = \frac{LT_d(E)}{T_i(E) - T_d(E)} \quad (6.2.9)$$

where L is the ribbon length, and T_i and T_d are the transmission for the ideal and defective ribbons respectively. They note that ballistic transport is possible when $\lambda >> L$, otherwise transport is diffusive.

For both types of ribbon the mean free path decreases with increasing density of defects, and they note that it oscillates with energy which makes it possible to tune transport properties with voltage, however this probably isn't practical for commercial applications.

For ZPNRs the mean free path changes from 9nm to 2nm when changing from 10% to 50% defects. For both decreasing the width also decreases the mean free path, which is a max of 73nm at 6.1nm for APNRs of 10% defects.

This means that APNRs are better than ZPNRs for a low level of defects (10%) only for widths smaller than 5nm, however they are better than any width for high (50%) level of defects.

In all cases increasing the defect density decreases the mobility, as does decreasing the width. The mobility is significantly lower in ZPNRs (2800 to 20 for 7 to 1 nm

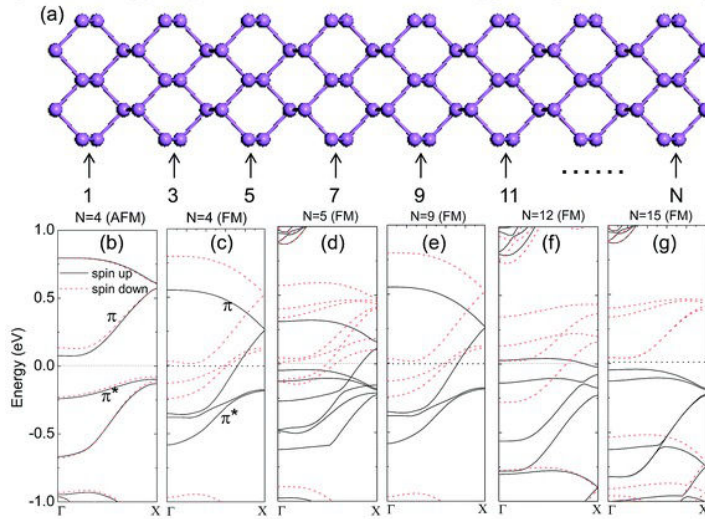


Figure 6.14: (a) Top view of ball-and-stick model of ZBPNRs. (b) and (c) The band structures of the 4-ZBPNR with antiferromagnetic ordering and ferromagnetic ordering, respectively. (d)–(g) Band structures of the ferromagnetic ZBPNRs with different ribbon widths. [103]

at 10% defects) compared to APNRs (5900 to 90 for 7 to 1nm at 10% defects). They note that the edge scattering is the dominant scattering process for widths below 5nm, which removes any anisotropy in ZPNR transport (note it is symmetrical for APNRs).

Variability in devices are high for both, but larger for ZPNRs, however both are smaller than for GNRs with the same defect levels.

APNRs have 3 to 5 times greater mobilities than GNRs, whilst ZPNRs are 3 to 7 times worse (pristine).

The bandgaps of PNRs are larger than GNRs, and also superior in mobilities in practice, with lower mobilities than GaAs and InP but comparable to bulk Si, UTB, SOI and monolayer MoS₂.

Yang et al reported their work on the spin dependent Seebeck effect [103]. They noted that ZPNRs are ferromagnetic (FM), and can have either ferromagnetic or anti-ferromagnetic ordering. They note that FM ordering gives a larger band splitting so is more desirable for the applications of spin caloritronics. They construct a theoretical device made from a ZPNR connected to a source and drain, with a thermal gradient applied between these contacts. They note that due to the band splitting based on spin, and the calculated transmission based on this, that only spin down electrons have a transmission peak above the Fermi level, and so move with a negative spin down current between drain and source. Whilst the spin up electrons have their transmission peak below the Fermi level, and so the holes move to the drain from the source thus creating a positive spin current. They note that the spin current is dozens of times larger than the absolute current, so the transport is dominated by the spin current.

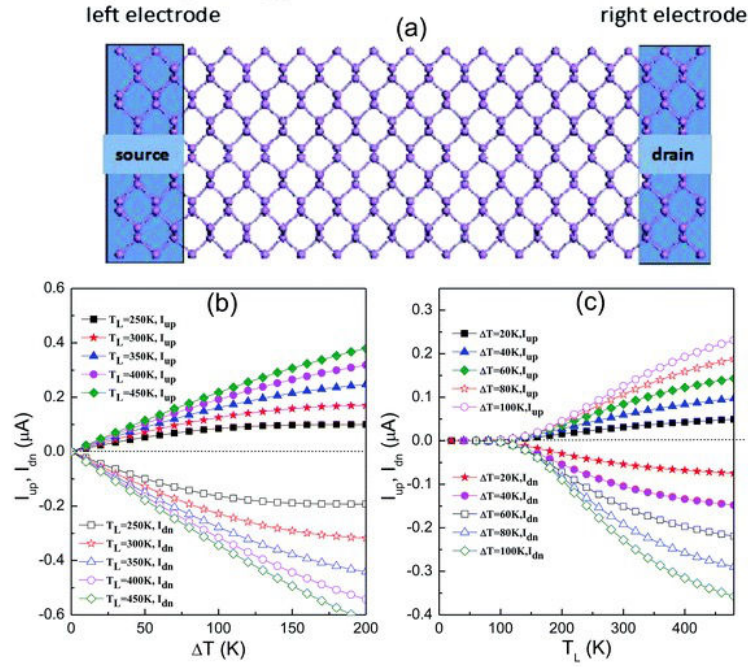


Figure 6.15: (a) The schematic illustration of the ZBPNR junction, where the source, the drain and the central scattering are adopted by the same ZBPNR with ferromagnetic ordering. (b) The spin-up current I_{up} and the spin-down current I_{dn} versus T_L for different values of ΔT . (c) I_{up} and I_{dn} versus ΔT for different values of the source temperature T_L . To [103]

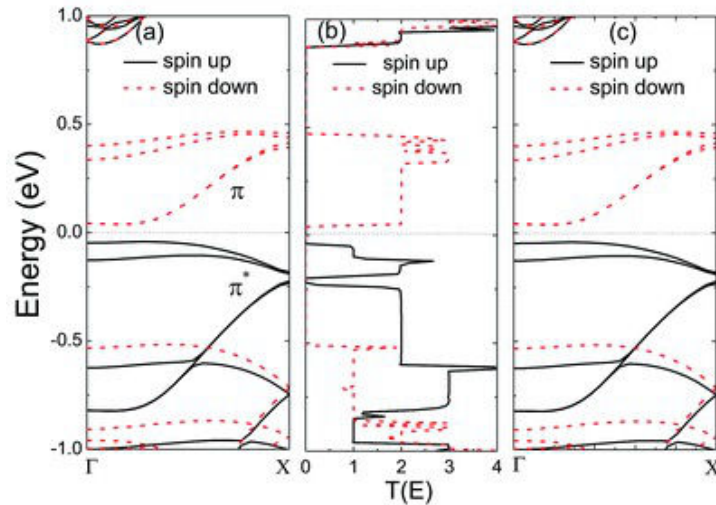


Figure 6.16: (a) and (c) The band structures of the left panel and the right panel of the 15-ZBPNR junction; (b) the spin-dependent transmission spectra of the junction. [103]

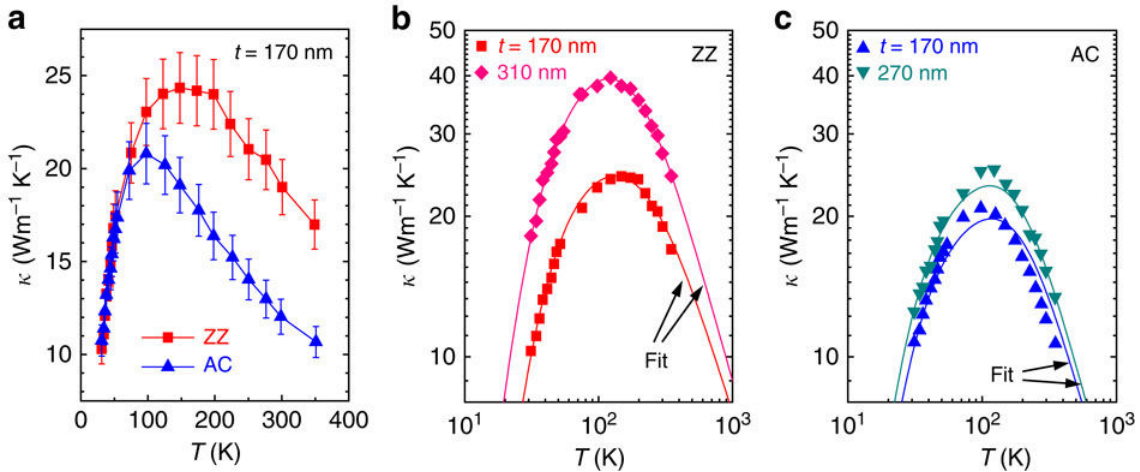


Figure 6.17: Temperature-dependent thermal conductivity of BP nanoribbons. (a) Thermal conductivity (κ) versus temperature (T) plot of BP nanoribbons axially oriented to the ZZ and AC directions, respectively. Thickness (t)/width (W) of the ZZ and AC nanoribbons are 170/540 nm and 170/590 nm, respectively. Error bars include the errors (B8%) from thermal conductance and sample size measurements. (b) κ versus T plots (on logarithmic scale) of ZZ nanoribbons with different dimensions; 170 (t)/540 nm (W) and 310 (t)/540 nm (W). (c) κ versus T plots (on logarithmic scale) of AC nanoribbons with different dimensions; 170 (t)/590 nm (W) and 270 (t)/420 nm (W). The solid lines in b and c are fitted lines by taking into account various phonon scattering mechanisms (phonon-phonon, impurity and boundary). Lengths of the nanoribbons all exceed 10 mm. [39]

6.2.3 Phononic and thermal

Lee et al. measured the electrical and thermal conductivities of their nanoribbons [39]. They note that BP has intrinsic anisotropy in its thermal transport and phonon dispersion. Nanoribbons of graphene exhibit similar anisotropy, however this is due to edge states causing different types of scattering depending on the edges, this effect may also be present in BP nanoribbons.

They found that κ along the ZZ direction is larger than along the AC direction above 100K, this increases with increasing T due to increased Umklapp (phonon-phonon) scattering. At 300K the anisotropy is roughly 2. They explain this as being due to the difference in group velocities. This is because at higher T the phonon states become excited, which saturated the specific heat at the Dulong-Petit limit. If the phonon-phonon scattering rate is the same along each direction then $\kappa \propto \nu^2$. ZZ has higher group velocity due to a lighter effective mass, and so this gives a factor of group velocities of 1.85, close to the measured 2.

They also note that below 100K the thermal conductance of each direction converges. They suggest this is due to freezing out of phonon modes. The higher group velocities above ZZ here mean that there is a lower phonon density along ZZ and so lower κ (this is due to Debye limit of q roughly ω/ν). So this explains the crossover.

They note that using the calculated values in fits they can calculate the phonon scattering rate along each direction. This gives a ratio of 1.25 which suggests that

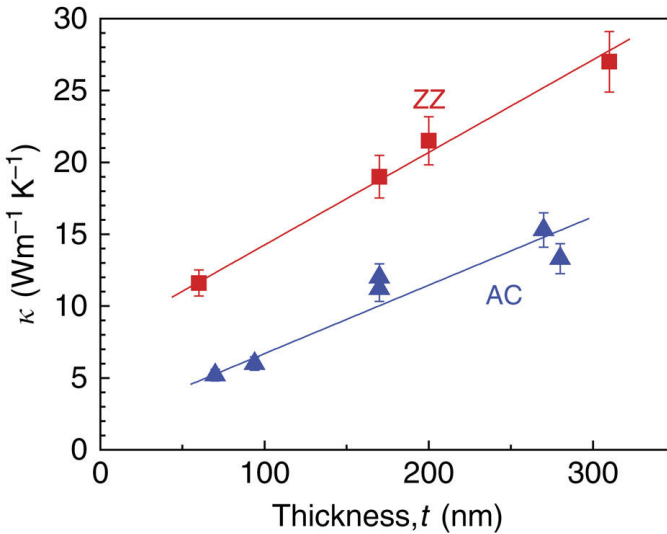


Figure 6.18: Thickness and orientation-dependent thermal conductivity of BP nanoribbons. Thermal conductivity of ZZ and AC nanoribbons, at 300K, as a function of thickness. Error bars include the errors (8%) from thermal conductance and sample size measurements. The lines show linear fitting of the data to guide the eye. [39]

phonon scattering has a lesser contribution to the total thermal transport.

They also find that in BP nanoribbons the TA1 mode contributes most to thermal transport.

They also note that the Seebeck coefficient is slightly larger along AC (320 vs 270), and that the lower factor is three times as large along the AC vs the ZZ. This is due to higher electrical transport along AC.

6.3 Characterisation and DFT

Zhang et al. found that the ZT value, which is an important measure for the effectiveness for thermoelectric applications, can be greatly enhanced for PNRs [107]. They used semi-classical Boltzmann theory (insert equations?), to deduce the thermal and electrical transport properties of ZPNRs and APNRs, as well as H-passivated edges. They found edge reconstructions in pristine ribbons, which caused indirect bandgap for APNRs and a metallic phase for ZPNRs unchanged. They did however see that H-passivation induced a direct bandgap in both types of ribbon.

They noted that the ribbons have positive formation edges, which were small and drop with increasing widths, indicating that they may be realised experimentally as these are smaller than for graphene or silicene nanoribbons. They also noted that ZPNRs were more energetically favourable.

They found that the ZT value in nanoribbons could be as high as 6.4 (which is comparable to current energy conversion methods), for n-type width 9 APNRs. H-passivated ZPNRs had the highest Seebeck coefficients and electrical transport, however they also had much larger lattice thermal conductivity due to dispersive

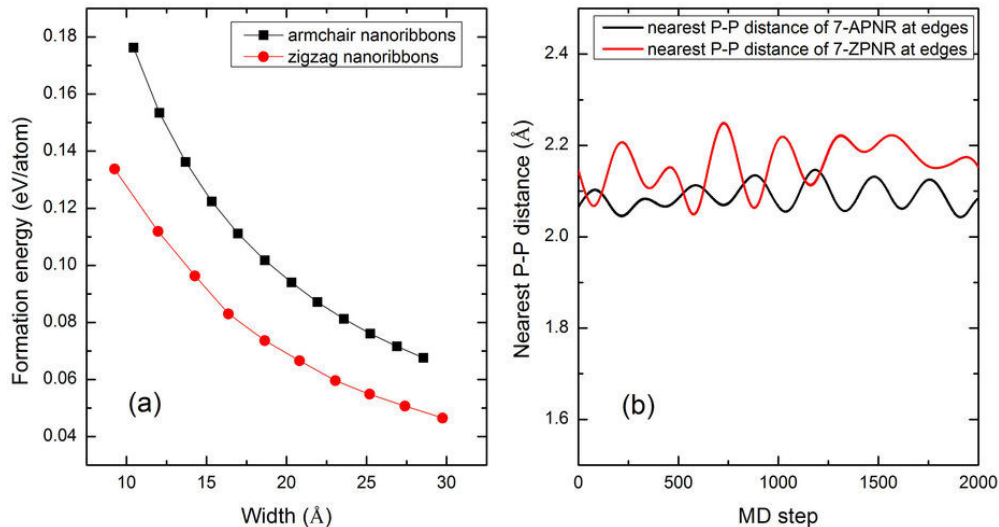


Figure 6.19: (a) The calculated formation energy of APNRs and ZPNRs as a function of the ribbon width, and (b) the ab-initio MD results of the nearest P-P distance at the edges for the 7-APNR and 7-ZPNR at room temperature. [107]

low frequency bands giving less edge phonon scattering, this lead to much smaller ZT values of 0.7 and 0.1 for p and n type respectively.

Note that ZT is dimensionless as this is a representative measurement of the heat engine efficiency of electricity conversion from heat, with infinity being the Carnot efficiency.

(REREAD THE EDGE DISPERSION FOR LOWER ZT BIT)

Bibliography

- [1] Yuichi Akahama, Shoichi Endo, and Shin-ichiro Narita. Electrical Properties of Black Phosphorus Single Crystals, 1983.
- [2] Andreas C. Albrecht. On the Theory of Raman Intensities. *The Journal of Chemical Physics*, 34(5):1476–1484, 1961.
- [3] Mamoru Baba, Fukunori Izumida, Akira Morita, Yoji Koike, and Tetsuro Fukase. Electrical properties of black phosphorus single crystals prepared by the bismuth-flux method. *Japanese Journal of Applied Physics*, 30(8):1753–1758, 1991.
- [4] Andres Castellanos-Gomez. Black Phosphorus: Narrow Gap, Wide Applications. *Journal of Physical Chemistry Letters*, 6(21):4280–4291, 2015.
- [5] Andres Castellanos-Gomez, Leonardo Vicarelli, Elsa Prada, Joshua O. Island, K. L. Narasimha-Acharya, Sofya I. Blanter, Dirk J. Groenendijk, Michele Buscema, Gary a. Steele, J. V. Alvarez, Henny W. Zandbergen, J. J. Palacios, and Herre S. J. van der Zant. Isolation and characterization of few-layer black phosphorus. *2D Materials*, 1(2):025001, 2014.
- [6] Andres Castellanos-gomez, Leonardo Vicarelli, Elsa Prada, Joshua O. Island, K. L. Narasimha-Acharya, Sofya I. Blanter, Dirk J. Groenendijk, Michele Buscema, Gary a. Steele, J. V. Alvarez, Henny W. Zandbergen, J. J. Palacios, Herre S. J. van der Zant, V Alvarez, Henny W. Zandbergen, J. J. Palacios, and Herre S J Van Der Zant. Isolation and characterization of few-layer black phosphorus [Supporting information]. *2D Materials*, 1(2):025001, 2014.
- [7] Andres Castellanos-Gomez, Leonardo Vicarelli, Elsa Prada, Joshua O. Island, K. L. Narasimha-Acharya, Sofya I. Blanter, Dirk J. Groenendijk, Michele Buscema, Gary a. Steele, J. V. Alvarez, Henny W. Zandbergen, J. J. Palacios, and Herre S. J. van der Zant. Isolation and characterization of few-layer black phosphorus. *2D Materials*, 1(2):025001, 2014.
- [8] Long Chen, Guangmin Zhou, Zhibo Liu, Xiaomeng Ma, Jing Chen, Zhiyong Zhang, Xiuliang Ma, Feng Li, Hui Ming Cheng, and Wencai Ren. Scalable Clean Exfoliation of High-Quality Few-Layer Black Phosphorus for a Flexible Lithium Ion Battery. *Advanced Materials*, 28(3):510–517, 2016.
- [9] Long Chen, Guangmin Zhou, Zhibo Liu, Xiaomeng Ma, Jing Chen, Zhiyong Zhang, Xiuliang Ma, Feng Li, Hui Ming Cheng, and Wencai Ren. Scalable Clean Exfoliation of High-Quality Few-Layer Black Phosphorus for a Flexible Lithium Ion Battery. *Advanced Materials*, 28(3):510–517, 2016.

- [10] Wilson A. Crichton, Mohamed Mezouar, Giulio Monaco, and Sara Falconi. Phosphorus: New in situ powder data from large-volume apparatus. *Powder Diffraction*, 18(02):155–158, 2003.
- [11] Mouad Dahbi, Naoaki Yabuuchi, Mika Fukunishi, Kei Kubota, Kuniko Chihara, Kazuyasu Tokiwa, Xue-fang Yu, Hiroshi Ushiyama, Koichi Yamashita, Jin-Young Son, Yi-Tao Cui, Hiroshi Oji, and Shinichi Komaba. Black Phosphorus as a High-Capacity, High-Capability Negative Electrode for Sodium-Ion Batteries: Investigation of the Electrode/Electrolyte Interface. *Chemistry of Materials*, page acs.chemmater.5b03524, 2016.
- [12] Saptarshi Das, Marcel Demarteau, Andreas Roelofs, Nanoscale Material, High Energy Physics, and United States. Ambipolar Phosphorene Field Effect Transistor. *ACS Nano*, (11):11730–11738, 2014.
- [13] Bangfu Ding, Wei Chen, Zilong Tang, and Junying Zhang. Tuning Phosphorene Nanoribbon Electronic Structure through Edge Oxidization. *Journal of Physical Chemistry C*, 120(4):2149–2158, 2016.
- [14] Rostislav a Doganov, Eoin C T O’Farrell, Steven P Koenig, Yuting Yeo, Angelo Ziletti, Alexandra Carvalho, David K Campbell, David F Coker, Kenji Watanabe, Takashi Taniguchi, Antonio H Castro Neto, and Barbaros Özyilmaz. Transport properties of pristine few-layer black phosphorus by van der Waals passivation in an inert atmosphere. *Nature communications*, 6:6647, 2015.
- [15] M. T. Edmonds, A. Tadich, A. Carvalho, A. Ziletti, K. M. O’Donnell, S. P. Koenig, D. F. Coker, B. ??zyilmaz, A. H Castro Neto, and M. S. Fuhrer. Creating a stable oxide at the surface of black phosphorus. *ACS Applied Materials and Interfaces*, 7(27):14557–14562, 2015.
- [16] Alexandre Favron, Etienne Gaufrès, Frédéric Fossard, Pierre L Lévesque, Phaneuf-l Heureux, Nathalie Y-w Tang, Annick Loiseau, and Richard Leonelli. Exfoliating black phosphorus down to the monolayer: photo-induced oxidation and electronic confinement effects. *arXiv preprint arXiv:1408.0345*, pages 1–33, 2014.
- [17] Alexandre Favron, Etienne Gaufrès, Frédéric Fossard, Anne-Laurence Phaneuf-L’Heureux, Nathalie Y-W Tang, Pierre L Lévesque, Annick Loiseau, Richard Leonelli, Sébastien Francoeur, and Richard Martel. Photooxidation and quantum confinement effects in exfoliated black phosphorus. *Nature materials*, 14(8):826–32, 2015.
- [18] Alexandre Favron, Etienne Gaufrès, Frédéric Fossard, Anne-Laurence Phaneuf-L’Heureux, Nathalie Y-W Tang, Pierre L Lévesque, Annick Loiseau, Richard Leonelli, Sébastien Francoeur, and Richard Martel. Photooxidation and quantum confinement effects in exfoliated black phosphorus. suppl. *Nature materials*, 14(8):826–832, 2015.
- [19] Ruixiang Fei, Alireza Faghaninia, Ryan Soklaski, Jia-an Yan, Cynthia Lo, and Li Yang. Enhanced Thermoelectric Efficiency via Orthogonal Electrical and Thermal Conductances in Phosphorene. 2014.

- [20] Fukuoka Shuhei, Taen Toshihiro, and Osada Toshihito. Electronic structure and the properties of phosphorene systems. *Journal of the Physical Society of Japan*, 84:121004–1 –121004–12, 2015.
- [21] Junfeng Gao, Gang Zhang, and Yong Wei Zhang. The Critical Role of Substrate in Stabilizing Phosphorene Nanoflake: A Theoretical Exploration. *Journal of the American Chemical Society*, 138(14):4763–4771, 2016.
- [22] Hongyan Guo, Ning Lu, Jun Dai, Xiaojun Wu, and Xiao Cheng Zeng. Phosphorene Nanoribbons, Phosphorus Nanotubes, and van der Waals Multilayers. *The Journal of Physical Chemistry C*, 118:14051–14059, 2014.
- [23] Zhinan Guo, Han Zhang, Shunbin Lu, Zhiteng Wang, Siying Tang, Jundong Shao, Zhengbo Sun, Hanhan Xie, Huaiyu Wang, Xue Feng Yu, and Paul K. Chu. From Black Phosphorus to Phosphorene: Basic Solvent Exfoliation, Evolution of Raman Scattering, and Applications to Ultrafast Photonics. *Advanced Functional Materials*, pages 6996–7002, 2015.
- [24] Damien Hanlon, Claudia Backes, Evie Doherty, Clotilde S. Cucinotta, Nina C. Berner, Conor Boland, Kangho Lee, Andrew Harvey, Peter Lynch, Zahra Gholamvand, Saifeng Zhang, Kangpeng Wang, Glenn Moynihan, Anuj Pokle, Quentin M. Ramasse, Niall McEvoy, Werner J. Blau, Jun Wang, Gonzalo Abellan, Frank Hauke, Andreas Hirsch, Stefano Sanvito, David D. O'Regan, Georg S. Duesberg, Valeria Nicolosi, and Jonathan N. Coleman. Liquid exfoliation of solvent-stabilized few-layer black phosphorus for applications beyond electronics. *Nature Communications*, 6:8563, 2015.
- [25] K. P S S Hembram, Hyun Jung, Byung Chul Yeo, Sung Jin Pai, Seungchul Kim, Kwang Ryeol Lee, and Sang Soo Han. Unraveling the Atomistic Sodiumation Mechanism of Black Phosphorus for Sodium Ion Batteries by First-Principles Calculations. *Journal of Physical Chemistry C*, 119(27):15041–15046, 2015.
- [26] Gui-qin Huang and Zhong-wen Xing. Superconductivity of bilayer phosphorene under interlayer compression . *Science*, 25(2):1–5, 2016.
- [27] Shouting Huang, Yufeng Liang, and Li Yang. Exciton spectra in two-dimensional graphene derivatives. *Physical Review B - Condensed Matter and Materials Physics*, 88(7):1–6, 2013.
- [28] Yuan Huang, Kai He, Stoyan Bliznakov, Eli Sutter, Fanke Meng, Dong Su, and Peter Sutter. Degradation of black phosphorus (BP): The role of oxygen and water. page arXiv 1511.09201, 2015.
- [29] Yuan Huang, Eli Sutter, Jerzy T. Sadowski, Mircea Cotlet, Oliver L A Monti, David A. Racke, Mahesh R. Neupane, Darshana Wickramaratne, Roger K. Lake, Bruce A. Parkinson, and Peter Sutter. Tin disulfide—an emerging layered metal dichalcogenide semiconductor: Materials properties and device characteristics. *ACS Nano*, 8(10):10743–10755, 2014.

- [30] Joshua O Island, Gary A Steele, Herre S J van der Zant, and Andres Castellanos-Gomez. Environmental instability of few-layer black phosphorus. *2D Materials*, 2(1):011002, 2015.
- [31] John C. Jamieson. Crystal Structures Adopted by. *Science*, 139(6):1291–1292, 1963.
- [32] Woosun Jang, Kisung Kang, and Aloysius Soon. Acute Mechano-Electronic Responses in Twisted Phosphorene Nanoribbons. *Nanoscale*, 2016.
- [33] Jin-Wu Jiang, Timon Rabczuk, and Harold S. Park. A Stillinger-Weber potential for single-layer black phosphorus, and the importance of cross-pucker interactions for negative Poisson’s ratio and edge stress-induced bending. *arXiv preprint*, 7:10, 2014.
- [34] Joon-Seok Kim, Yingnan Liu, Weinan Zhu, Seohee Kim, Di Wu, Li Tao, Ananth Dodabalapur, Keji Lai, and Deji Akinwande. Toward air-stable multilayer phosphorene thin-films and transistors. *Scientific reports*, 5:8989, 2015.
- [35] Jungcheol Kim, Jae-Ung Lee, Jinhwan Lee, Hyo Ju Park, Zonghoon Lee, Changgu Lee, and Hyeonsik Cheong. Anomalous polarization dependence of Raman scattering and crystallographic orientation of black phosphorus. *Nanoscale*, 7:18708–18715, 2015.
- [36] Steven P. Koenig, Rostislav A. Doganov, Henrik Schmidt, A. H. Castro Neto, and Barbaros Ozyilmaz. Electric field effect in ultrathin black phosphorus. *Applied Physics Letters*, 104(10):0–4, 2014.
- [37] Marianne Kopf, Nadine Eckstein, Daniela Pfister, Carolin Grotz, Ilona Kr??ger, Magnus Greiwe, Thomas Hansen, Holger Kohlmann, and Tom Nilges. Access and in situ growth of phosphorene-precursor black phosphorus. *Journal of Crystal Growth*, 405:6–10, 2014.
- [38] Liangzhi Kou, Thomas Frauenheim, and Changfeng Chen. Phosphorene as a superior gas sensor: Selective adsorption and distinct i - V response. *Journal of Physical Chemistry Letters*, 5(15):2675–2681, 2014.
- [39] Sangwook Lee, Fan Yang, Joonki Suh, Sijie Yang, Yeonbae Lee, Guo Li, Hwan Sung Choe, Aslihan Suslu, Yabin Chen, Changhyun Ko, Joonsuk Park, Kai Liu, Jingbo Li, Kedar Hippalgaonkar, Jeffrey J. Urban, Sefaattin Tongay, and Junqiao Wu. Anisotropic in-plane thermal conductivity of black phosphorus nanoribbons at temperatures higher than 100 K. *Nature Communications*, 6:8573, 2015.
- [40] Hai Li, Jumiati Wu, Xiao Huang, Gang Lu, Jian Yang, Xin Lu, Qihua Xiong, and Hua Zhang. Rapid and reliable thickness identification of two-dimensional nanosheets using optical microscopy. *ACS Nano*, 7(11):10344–10353, 2013.
- [41] Xuesong Li, Bingchen Deng, Xiaomu Wang, Sizhe Chen, Michelle Vaisman, Shun-ichiro Karato, Grace Pan, Minjoo Larry Lee, Judy Cha, Han Wang, and Fengnian Xia. Synthesis of thin-film black phosphorus on a flexible substrate. *2D Materials*, 2(3):031002, 2015.

- [42] L. Lindsay, Wu Li, Jes??s Carrete, Natalio Mingo, D. A. Broido, and T. L. Reinecke. Phonon thermal transport in strained and unstrained graphene from first principles. *Physical Review B - Condensed Matter and Materials Physics*, 89(15):1–8, 2014.
- [43] Xi Ling, Han Wang, Shengxi Huang, Fengnian Xia, and Mildred S. Dresselhaus. The renaissance of black phosphorus. *Proceedings of the National Academy of Sciences*, 112(15):201416581, 2015.
- [44] Zhi Peng Ling and Kah Wee Ang. Thermal effects on the Raman phonon of few-layer phosphorene. *APL Materials*, 3(12):0–6, 2015.
- [45] Han Liu, Yuchen Du, Yexin Deng, and Peide D Ye. Semiconducting black phosphorus: synthesis, transport properties and electronic applications. *Chemical Society Reviews*, 44:2732–2743, 2015.
- [46] Han Liu, Adam T. Neal, Zhen Zhu, David Tomanek, and Peide D. Ye. Phosphorene: A New 2D Material with High Carrier Mobility. *ACS nano*, 4133:4033–4041, 2014.
- [47] Jie Liu, Yaguang Guo, Shunhong Zhang, Qian Wang, Yoshiyuki Kawazoe, and Puru Jena. New Phosphorene Allotropes Containing Ridges with 2- and 4-Coordination. *Journal of Physical Chemistry C*, 119(43):24674–24680, 2015.
- [48] X Liu, Y W Wen, Z Z Chen, B Shan, and R Chen. A first-principles study of sodium adsorption and diffusion on phosphorene. *Physical Chemistry Chemical Physics*, 17(25):16398–16404, 2015.
- [49] Yuanyue Liu, Fangbo Xu, Ziang Zhang, Evgeni S. Penev, and Boris I. Yakobson. Two-dimensional mono-elemental semiconductor with electronically inactive defects: The case of phosphorus. *Nano Letters*, 14(12):6782–6786, 2014.
- [50] R. Loudon. Theory of the First-Order Raman Effect in Crystals. *Proceedings of the Royal Society A*, 275(1361), 1963.
- [51] R. Loudon. The Raman effect in crystals. *Advances in Physics*, 13(52):423–482, 1964.
- [52] Wanglin Lu, Xiaomeng Ma, Zhen Fei, Jianguang Zhou, Zhiyong Zhang, Chuanhong Jin, and Ze Zhang. Probing the anisotropic behaviors of black phosphorus by transmission electron microscopy, angular-dependent Raman spectra, and electronic transport measurements. *Applied Physics Letters*, 107(2), 2015.
- [53] H. Y. Lv, W. J. Lu, D. F. Shao, and Y. P. Sun. Large thermoelectric power factors in black phosphorus and phosphorene. *Cornell University Library*, page 2189, 2014.
- [54] M. Cardona and G. Gfintherodt. *Light scattering in solids II*, volume 50. Springer, Berlin, 2 edition, 1982.

- [55] R Ma, H Geng, W Y Deng, M N Chen, L Sheng, and D Y Xing. Effect of the edge states on the conductance and thermopower in Zigzag Phosphorene Nanoribbons. pages 1–6, 2016.
- [56] Nannan Mao, Juanxia Wu, Bowen Han, Jingjing Lin, Lianming Tong, and Jin Zhang. Birefringence-Directed Raman Selection Rules in 2D Black Phosphorus Crystals. *Small*, pages 2627–2633, 2016.
- [57] Paul Masih Das, Gopinath Danda, Andrew Cupo, William M. Parkin, Liangbo Liang, Neerav Kharche, Xi Ling, Shengxi Huang, Mildred S. Dresselhaus, Vincent Meunier, and Marija Drndic. Controlled Sculpture of Black Phosphorus Nanoribbons. *ACS Nano*, page acsnano.6b02435, 2016.
- [58] Matthew a. Meitl, Zheng-Tao Zhu, Vipan Kumar, Keon Jae Lee, Xue Feng, Yonggang Y. Huang, Ilesanmi Adesida, Ralph G. Nuzzo, and John a. Rogers. Transfer printing by kinetic control of adhesion to an elastomeric stamp. *Nature Materials*, 5(1):33–38, 2006.
- [59] Junhong Na, Young Tack Lee, Jung Ah Lim, Do Kyung Hwang, Gyu Tae Kim, Won Kook Choi, and Yong Won Song. Few-layer black phosphorus field-effect transistors with reduced current fluctuation. *ACS Nano*, 8(11):11753–11762, 2014.
- [60] Adam T Neal. Phosphorene : An Unexplored 2D Semiconductor with a High Hole Mobility. (4):4033–4041, 2014.
- [61] P. Nemes-Incze, Z. Osv??th, K. Kamar??s, and L. P. Bir?? Anomalies in thickness measurements of graphene and few layer graphite crystals by tapping mode atomic force microscopy. *Carbon*, 46(11):1435–1442, 2008.
- [62] Zahra Nourbakhsh and Reza Asgari. Excitons and optical spectra of phosphorene nanoribbons. pages 1–9, 2016.
- [63] Yasuharu Okamoto. Density Functional Theory Calculations of Alkali Metal (Li, Na, and K) Graphite Intercalation Compounds. *The Journal of Physical Chemistry C*, 118:131219114554000, 2013.
- [64] Maurizia Palummo, Federico Iori, Rodolfo Del Sole, and Stefano Ossicini. Giant excitonic exchange splitting in Si nanowires: First-principles calculations. *Physical Review B - Condensed Matter and Materials Physics*, 81(12):1–4, 2010.
- [65] Keith R. Paton, Eswaraiah Varrla, Claudia Backes, Ronan J. Smith, Umar Khan, Arlene O'Neill, Conor Boland, Mustafa Lotya, Oana M. Istrate, Paul King, Tom Higgins, Sebastian Barwich, Peter May, Pawel Puczkarski, Iftikhar Ahmed, Matthias Moebius, Henrik Pettersson, Edmund Long, João Coelho, Sean E. O'Brien, Eva K. McGuire, Beatriz Mendoza Sanchez, Georg S. Duesberg, Niall McEvoy, Timothy J. Pennycook, Clive Downing, Alison Crossley, Valeria Nicolosi, and Jonathan N. Coleman. Scalable production of large quantities of defect-free few-layer graphene by shear exfoliation in liquids. *Nature Materials*, 13(6):624–630, 2014.

- [66] Jiajie Pei, Xin Gai, Jiong Yang, Xibin Wang, Zongfu Yu, Duk-Yong Choi, Barry Luther-Davies, and Yuerui Lu. Producing air-stable monolayers of phosphorene and their defect engineering. *Nature communications*, 7:10450, 2016.
- [67] Vasili Perebeinos, J. Tersoff, and Phaedon Avouris. Radiative lifetime of excitons in carbon nanotubes. *Nano Letters*, 5(12):2495–2499, 2005.
- [68] Warner L. Peticolas, Laurence Nafie, Paul Stein, and Bruno Faconi. Quantum Theory of the Intensities of Molecular Vibrational Spectra. *The Journal of Chemical Physics*, 52(3):1576, 1970.
- [69] Mirko Poljak and Tomislav Suligoj. Immunity of electronic and transport properties of phosphorene nanoribbons to edge defects. *Nano Research*, 9(6):1723–1734, 2016.
- [70] Jingsi Qiao, Xianghua Kong, Zhi-Xin Hu, Feng Yang, and Wei Ji. High-mobility transport anisotropy and linear dichroism in few-layer black phosphorus. *Nature Communications*, 5:4475, 2014.
- [71] Jingsi Qiao, Xianghua Kong, Zhi-Xin Hu, Feng Yang, and Wei Ji. High-mobility transport anisotropy and linear dichroism in few-layer black phosphorus. *Nature Communications*, 5:4475, 2014.
- [72] Jingsi Qiao, Xianghua Kong, Zx Hu, Feng Yang, and Wei Ji. Few-layer black phosphorus: emerging direct band gap semiconductor with high carrier mobility. *arXiv preprint arXiv:1401.5045*, 2014.
- [73] Henrique B. Ribeiro, Marcos A. Pimenta, Christiano J S De Matos, Roberto Luiz Moreira, Aleksandr S. Rodin, Juan D. Zapata, Eunézio A T De Souza, and Antonio H. Castro Neto. Unusual angular dependence of the Raman response in black phosphorus suppl. *ACS Nano*, 9(4):4270–4276, 2015.
- [74] Henrique B. Ribeiro, Marcos A. Pimenta, Christiano J S De Matos, Roberto Luiz Moreira, Aleksandr S. Rodin, Juan D. Zapata, Eunézio A T De Souza, and Antonio H. Castro Neto. Unusual angular dependence of the Raman response in black phosphorus. *ACS Nano*, 9(4):4270–4276, 2015.
- [75] Christiaan Ridings, Gregory G. Warr, and Gunther G. Andersson. Composition of the outermost layer and concentration depth profiles of ammonium nitrate ionic liquid surfaces. *Physical Chemistry Chemical Physics*, pages 16088–16095, 2012.
- [76] Brow RK. ‘Review: the structure of simple phosphate glasses’. *J. Non-Cryst. Solids*, 263–264:1, 2000.
- [77] S. Roddaro, P. Pingue, V. Piazza, V. Pellegrini, and F. Beltram. The optical visibility of graphene: Interference colors of ultrathin graphite on SiO₂. *Nano Letters*, 7(9):2707–2710, 2007.
- [78] A Sanna, A V Fedorov, N I Verbitskiy, J Fink, C Krellner, L Petaccia, A Chikina, D Yu Usachov, A Grüneis, and G Profeta. First-principles and angle-resolved photoemission study of lithium doped metallic black phosphorous. *2D Materials*, 3(2):025031, 2016.

- [79] Manuel Serrano-Ruiz, Maria Caporali, Andrea Ienco, Vincenzo Piazza, Stefan Heun, and Maurizio Peruzzini. The Role of Water in the Preparation and Stabilization of High-Quality Phosphorene Flakes. *Advanced Materials Interfaces*, 3(3):2–9, 2016.
- [80] D. F. Shao, W. J. Lu, H. Y. Lv, and Y. P. Sun. Electron-doped phosphorene: A potential monolayer superconductor. *arXiv*, 108(6):1–5, 2014.
- [81] S Sugai. RAMAN AND INFRARED REFLECTION SPECTROSCOPY IN BLACK PHOSPHORUS. 53(9):753–755, 1984.
- [82] Jie Sun, Hyun-Wook Lee, Mauro Pasta, Hongtao Yuan, Guangyuan Zheng, Yongming Sun, Yuzhang Li, and Yi Cui. A phosphorene-graphene hybrid material as a high-capacity anode for sodium-ion batteries. *Nature nanotechnology*, 10(11):980–5, 2015.
- [83] Jie Sun, Hyun-Wook Lee, Mauro Pasta, Hongtao Yuan, Guangyuan Zheng, Yongming Sun, Yuzhang Li, and Yi Cui. A phosphorene-graphene hybrid material as a high-capacity anode for sodium-ion batteries. suppl. *Nature nanotechnology*, 10(11):980–5, 2015.
- [84] Jie Sun, Guangyuan Zheng, Hyun Wook Lee, Nian Liu, Haotian Wang, Hongbin Yao, Wensheng Yang, and Yi Cui. Formation of stable phosphorus-carbon bond for enhanced performance in black phosphorus nanoparticle-graphite composite battery anodes. *Nano Letters*, 14(8):4573–4580, 2014.
- [85] Zhipei Sun, Tawfique Hasan, Felice Torrisi, Daniel Popa, Giulia Privitera, Fengqiu Wang, Francesco Bonaccorso, Denis M Basko, and Andrea C Ferrari. Graphene Mode-Locked Ultrafast Laser. *ACS Nano*, 4(2):803–810, 2010.
- [86] David R. Tobergte and Shirley Curtis. Anisotropic in-plane thermal conductivity of black phosphorus nanoribbons at temperatures higher than 100 K. *Journal of Chemical Information and Modeling*, 53(9):1689–1699, 2013.
- [87] Vy Tran and Li Yang. Unusual Scaling Laws of the Band Gap and Optical Absorption of Phosphorene Nanoribbons. *arXiv preprint arXiv:1404.2247*, 2014.
- [88] Kainen L. Utt, Pablo Rivero, Mehrshad Mehboudi, Edmund O. Harriss, Mario F. Borunda, Alejandro A. Pacheco SanJuan, and Salvador Barraza-Lopez. Intrinsic Defects, Fluctuations of the Local Shape, and the Photo-Oxidation of Black Phosphorus. *ACS Central Science*, 1(6):320–327, 2015.
- [89] Deepti Verma. SIZESCALE EFFECTS IN BENDING FLEXIBILITY OF PHOSPHORENE AND ITS 2D ALLOTROPES. (August):1–2, 2016.
- [90] Gaoxue Wang, William J. Slough, Ravindra Pandey, and Shashi P. Karna. Degradation of Phosphorene in Air: Understanding at Atomic Level. *2D Materials*, 3(2):1–7, 2015.
- [91] V. Wang, Y. C. Liu, Y. Kawazoe, and W. T. Geng. Role of Interlayer Coupling on the Evolution of Band Edges in Few-Layer Phosphorene. *Journal of Physical Chemistry Letters*, 6(24):4876–4883, 2015.

- [92] Xiaomu Wang, Aaron M. Jones, Kyle L. Seyler, Vy Tran, Yichen Jia, Huan Zhao, Han Wang, Li Yang, Xiaodong Xu, and Fengnian Xia. Highly anisotropic and robust excitons in monolayer black phosphorus. *Nature Nanotechnology*, 10(6):517–521, 2015.
- [93] Qun Wei and Xihong Peng. Superior mechanical flexibility of phosphorene and few-layer black phosphorus. *Applied Physics Letters*, 104(25):251915, 2014.
- [94] Joshua D Wood, Spencer a Wells, Deep Jariwala, Kan-sheng Chen, Eunkyoung Cho, Vinod K Sangwan, Xiaolong Liu, Lincoln J Lauhon, Tobin J Marks, and Mark C Hersam. Effective Passivation of Exfoliated Black Phosphorus Transistors against Ambient Degradation. *Nano Letters*, 14:6964–6970, 2014.
- [95] Adam H. Woomer, Tyler W. Farnsworth, Jun Hu, Rebekah A. Wells, Carrie L. Donley, and Scott C. Warren. Phosphorene: Synthesis, Scale-Up, and Quantitative Optical Spectroscopy. *ACS Nano*, 9(9):8869–8884, 2015.
- [96] Qingyun Wu, Lei Shen, Ming Yang, Zhigao Huang, and Yuan Ping Feng. Band Gaps and Giant Stark Effect in Non-Chiral Phosphorene Nanoribbons. pages 1–19, 2014.
- [97] Qingyun Wu, Lei Shen, Ming Yang, Zhigao Huang, and Yuan Ping Feng. Electronic and Transport Property of Phosphorene Nanoribbon. pages 1–19, 2014.
- [98] Fengnian Xia, Han Wang, and Yichen Jia. Rediscovering black phosphorus as an anisotropic layered material for optoelectronics and electronics. *Nature communications*, 5:4458, 2014.
- [99] Fengnian Xia, Han Wang, and Yichen Jia. Rediscovering black phosphorus as an anisotropic layered material for optoelectronics and electronics. *Nature communications*, 5:4458, 2014.
- [100] Weiwei Xia, Qiubo Zhang, Feng Xu, Hongyu Ma, Jing Chen, Khan Qasim, Binghui Ge, Chongyang Zhu, and Litao Sun. Visualizing the Electrochemical Lithiation/Delithiation Behaviors of Black Phosphorus by in Situ Transmission Electron Microscopy. *Journal of Physical Chemistry C*, 120(11):5861–5868, 2016.
- [101] Gui-Liang Xu, Zonghai Chen, Gui-Ming Zhong, Yuzi Liu, Yong Yang, Tianyuan Ma, Yang Ren, Xiaobing Zuo, Xue-Hang Wu, Xiaoyi Zhang, and Khalil Amine. Nanostructured Black Phosphorus/Ketjenblack–Multiwalled Carbon Nanotubes Composite as High Performance Anode Material for Sodium-Ion Batteries. *Nano Letters*, page acs.nanolett.6b01777, 2016.
- [102] Jiong Yang, Renjing Xu, Jiajie Pei, Ye Win Myint, Fan Wang, Zhu Wang, Shuang Zhang, Zongfu Yu, and Yuerui Lu. Unambiguous identification of monolayer phosphorene by phase-shifting interferometry. *arXiv*, page 1412.6701, 2014.
- [103] Yu-Rong Yang, Zhao-Qian Zhang, Lei Gu, and Hua-Hua Fu. Spin-dependent Seebeck effect in zigzag black phosphorene nanoribbons. *RSC Adv.*, 6(50):44019–44023, 2016.

- [104] Xue Fang Yu, Giacomo Giorgi, Hiroshi Ushiyama, and Koichi Yamashita. First-principles study of fast Na diffusion in Na₃P. *Chemical Physics Letters*, 612:129–133, 2014.
- [105] Xue-fang Yu, Hiroshi Ushiyama, and Koichi Yamashita. Comparative Study of Sodium and Lithium Intercalation and Diffusion Mechanism in Black Phosphorus from First-principles Simulation. *Chemistry Letters*, 43(12):1940–1942, 2014.
- [106] Zhaoxin Yu, Jiangxuan Song, Mikhail L. Gordin, Ran Yi, Duihai Tang, and Donghai Wang. Phosphorus-Graphene Nanosheet Hybrids as Lithium-Ion Anode with Exceptional High-Temperature Cycling Stability. *Advanced Science*, 2(1-2):n/a–n/a, 2015.
- [107] J Zhang, H J Liu, L Cheng, J Wei, J H Liang, D D Fan, J Shi, X F Tang, and Q. J. Zhang. Phosphorene nanoribbon as a promising candidate for thermo-electric applications. *Scientific reports*, 4:4–10, 2014.
- [108] Shuang Zhang, Jiong Yang, Renjing Xu, Fan Wang, Weifeng Li, Muhammad Ghulran, Yong Wei Zhang, Zongfu Yu, Gang Zhang, Qinghua Qin, and Yuerui Lu. Extraordinary photoluminescence and strong temperature/angle-dependent raman responses in few-layer phosphorene. *ACS Nano*, 8(9):9590–9596, 2014.
- [109] Ming Zhao, Haolei Qian, Xinyue Niu, Wei Wang, Liao Guan, Jian Sha, and Yewu Wang. Growth Mechanism and Enhanced Yield of Black Phosphorus Microribbons. *Crystal Growth and Design*, 16(2):1096–1103, 2016.
- [110] Liyan Zhu, Gang Zhang, and Baowen Li. Coexistence of size-dependent and size-independent thermal conductivities in phosphorene. *Physical Review B - Condensed Matter and Materials Physics*, 90(21):2–7, 2014.
- [111] Weinan Zhu, Maruthi N. Yogeesh, Shixuan Yang, Sandra H. Aldave, Joon Seok Kim, Sushant Sonde, Li Tao, Nanshu Lu, and Deji Akinwande. Flexible black phosphorus ambipolar transistors, circuits and AM demodulator. *Nano Letters*, 15(3):1883–1890, 2015.
- [112] Zhen Zhu and David Tom??nek. Semiconducting layered blue phosphorus: A computational study. *Physical Review Letters*, 112(17):1–5, 2014.
- [113] A. Ziletti, A. Carvalho, D. K. Campbell, D. F. Coker, and A. H. Castro Neto. Oxygen defects in phosphorene. *Physical Review Letters*, 114(4):3–7, 2015.